

9529580129

EX

D/Blue

Design Analysis and Fabrication of a Lateral MEMS Microactuator

Chin Chi Choong



School of Mechanical and Aerospace Engineering

A thesis submitted to the Nanyang Technological University
in fulfilment of the requirement for the degree of
Master of Engineering

2007

Abstract

Radio-frequency microelectromechanical systems (RF MEMS) are highly miniaturized devices intended to switch, modulate, filter or tune electrical signals from DC to microwave frequencies. A novel lateral MEMS microactuator switch concept has been developed for RF switching purposes. The high-aspect ratio of the microactuator switch structure is designed and made possible through microfabrication via bulk micromachining; and is developed with thin-film deposition, silicon-glass wafer bonding and DRIE (deep reactive ion etching) technologies. The design has a 'push-pull' reciprocating actuation configuration with a lateral switch-contact structure, and is driven by electrostatic comb-drive actuators. The transmission section of the microactuator switch assembly is uniquely electrically insulated and physically connected to the microactuator structure by a dielectric slot, filled with silicon oxide and silicon nitride deposition. Finite element analysis has been employed to check on the structural integrity of the designed micromechanical flexures and justify the theoretical flexure stiffness. Using sputtered gold as the contact material, it has been demonstrated that a contact resistance below 1.64Ω is maintained for up to 3.2 million cycles of continuous switching operation. The microactuator switch can work well under an input square waveform at a frequency of 3.5kHz, corresponding to a switching time of 0.29ms under an actuation voltage of 60V. This would justify the good insulating capability of the dielectric slot for proper switching operations. Both the structural integrity and bonding capability of the dielectric slot are very good as it can structurally 'bond' two physically separate sections together even after reliability testing.

Acknowledgements

The author would like to express his deepest gratitude and sincere appreciation to both his supervisors, Associate Professor Xiao Zhongmin and Associate Professor Miao Jianmin. Both Assoc/Prof. Xiao's in-depth knowledge in the field of engineering mechanics and Assoc/Prof Miao's expertise in MEMS theory and microfabrication techniques, have made this research project possible. The author has received valuable advice and learned new skills, together with encouragement to work on MEMS engineering and learn the philosophy of research in fundamental issues. Both Assoc/Prof Xiao and Assoc/Prof Miao are so warmhearted and helpful, and the author has benefited much from their expertise during his research work. The author felt blessed to be given the opportunity to work under both their supervision.

The author would also like to express his appreciation to research fellow Dr Chen Longqing, who has taken time from his busy work schedule to give his unselfish guidance and assistance to the author's research project. Special thanks is extended to the staff in the Micromachines Centre (MMC), namely Mr Hoong Sin Poh, Mr Lau Joo Kiang, Mr Pek Soo Siong, Mr Wong Kim Chong, Mr Ho Kar Kiat and Mr Nordin Bin Abdul Kassim.

The author is also appreciative of the help rendered by fellow research students in the MMC: Ashraf Mohammed, Sun Jianbo, Wu Jie, Ke Fei Xiang and Wang Cheng. They have given much help and have been cooperative during daily work.

Acknowledgements

The author would also like to thank his company, Defence Science Organization (DSO) National Laboratories, for awarding him a postgraduate scholarship, hence giving him the opportunity to learn new engineering knowledge and technical skills.

Finally, the author would like to express his heartfelt thanks to his parents, lovely wife Joey, cute baby girls Jovie and Jolyn, his sister Fui Ling and all friends, for their love and support.

<u>Table of Contents</u>	
Abstract	i
Acknowledgements	ii
Table of Contents	iv
List of Abbreviations	viii
List of Figures	ix
List of Symbols	xv
List of Tables	xvi
	<u>Page</u>
Chapter 1: Introduction	1
1.1 Background	1
1.2 Objective	6
1.3 Scope of work	6
1.4 Report structure	7
Chapter 2: Literature Review	9
2.1 MEMS fabrication technology	9
2.1.1 Bulk micromachining	9
2.1.2 Surface micromachining	11
2.1.3 Micromoulding	13
2.1.4 Main microfabrication techniques for proposed microactuator design	15
2.1.4.1 Deep reactive ion etching (DRIE)	15
2.1.4.2 Wafer bonding	18
2.2 RF MEMS switches	21
2.2.1 Overview of RF MEMS	21
2.2.2 Miniaturization of mechanical switches	22
2.2.3 MEMS switch types	24

2.2.4	Electrostatic microactuator for RF MEMS switches	27
2.2.5	Application of MEMS switches	29
2.3	Design considerations of electrostatic metal-to-metal contact switches	31
2.3.1	Actuation voltage, displacement, contact and restoring forces	31
2.3.2	Contact distance versus isolation	36
2.3.3	Reliability of metal-to-metal contacts	38
2.3.4	Adhesion between actuation electrodes	42
2.4	Chapter summary	44
 Chapter 3: Design of the Lateral Microactuator Switch		46
3.1	Basic mechanism of electrostatic actuation	46
3.1.1	Parallel-plate capacitors	47
3.1.2	Types of electrostatic comb-drive	49
3.1.2.1	Lateral motion comb-drive	50
3.1.2.2	Vertical motion comb-drive	54
3.1.2.3	Transverse motion comb-drive	55
3.1.2.4	Rotary motion comb-drive	57
3.2	Design of the lateral MEMS microactuator switch	62
3.2.1	Specifications	62
3.2.2	Design features	62
3.2.2.1	Layout and mode of actuation	63
3.2.2.2	Structure of microactuator	65
3.2.2.3	Micromechanical flexure design	66
3.2.2.4	Resonant frequency of system	67
3.2.2.5	Actuation force, contact force and restoring force	67
3.2.2.6	Structural toughness and reliability	68
3.2.3	Micromechanical flexure designs	68
3.2.3.1	Straight-plate flexure	68
3.2.3.2	Fixed-fixed beam flexure	71
3.2.3.3	Crab-leg flexure	73
3.2.3.4	Folded flexure	74
3.2.4	Design calculations for the proposed design	75

3.3	Chapter summary	81
Chapter 4: Finite Element Analysis of the Microactuator		
	Structure	83
4.1	Introduction to the Finite Element Analysis (FEA)	83
	4.1.1 Validity and accuracy of finite element solutions	84
	4.1.2 Advantages and disadvantages of FEA	85
	4.1.3 General rules for finite element modeling	87
	4.1.4 Introduction to ANSYS	88
	4.1.5 General FEM procedures	90
4.2	Finite element analysis of micromechanical flexure designs	91
	4.2.1 Straight-plate flexure	92
	4.2.2 Fixed-fixed flexure	96
	4.2.3 Crab-leg flexure	99
	4.2.4 Folded flexure	103
4.3	Fatigue	107
	4.3.1 Introduction	107
	4.3.2 Fatigue loading	109
	4.3.3 S-N-P curves	112
	4.3.4 The influence of non-zero mean stress	113
4.4	Chapter summary	114
Chapter 5: Mask Design and Microfabrication Process		116
5.1	CAD modeling	116
5.2	Proposed fabrication process flow	119
5.3	Mask design	127
5.4	Fabrication process and results	132
5.5	Chapter summary	139

Table of Contents

Chapter 6: Results and Discussion	141
6.1 Test results	141
6.1.1 Actuation voltage	141
6.1.2 Contact resistance	142
6.1.3 Switching time	142
6.1.4 Switching lifetime	142
6.2 Discussion	144
Chapter 7: Conclusion and Recommendations	148
7.1 Conclusion	148
7.2 Recommendations	149

References

Appendix

List of Abbreviations

3-D	:	three-dimensional
CAD	:	computer aided design
CMOS	:	complementary metal-oxide semiconductor
CPU	:	central processing unit
DC	:	direct current
DNA	:	Deoxyribonucleic acid
DOF	:	degree of freedom
DRIE	:	deep reactive ion etching
FEA	:	finite element analysis
FEM	:	finite element method
FET	:	field effect transistor
IC	:	integrated circuit
KOH	:	Potassium Hydroxide
LIGA	:	lithographic, galvanofomung and Abformung
LPCVD	:	low pressure chemical vapour deposition
MEMS	:	microelectromechanical systems
PMMA	:	polymethylmethacrylate
PSG	:	phosphosilicate glass
Q	:	Quality factor
RF MEMS	:	radio-frequency microelectromechanical systems
RIE	:	reactive ion etching
SAM	:	self assembled layer
SEM	:	scanning electron microscope
SOI	:	silicon on insulator
SRF	:	self resonance frequency
VLSI	:	very large scale integration

List of Figures

Figure 1: Bulk micromachined structure

Figure 2: Generic surface micromachining process to fabricate a doubly-anchored poly-silicon bridge: (a) deposition and patterning of sacrificial PSG layer; (b) deposition and patterning of polysilicon structural layer; (c) release of structural layer by removal of sacrificial layer [30].

Figure 3: Setup for deep reactive ion etching (DRIE) process

Figure 4: Passivation step in DRIE process

Figure 5: Etch step in DRIE process

Figure 6: Overview of advanced silicon etch process: (a) simultaneous sidewall passivation; (b) deposition process; (c) etching process

Figure 7: Schematic of an anodic wafer bonding process [24]

Figure 8: Most common electrostatically actuated MEMS switch types [3]

Figure 9: Laterally driven electrostatic comb-drive resonant microactuator [41]

Figure 10: (a) Top and end view of a cantilever based switch; (b) simplified mechanical equivalent circuit model; (c) active forces and when opening the contact

Figure 11: Schematic of a parallel-plate capacitor

Figure 12: Schematic of an electrostatic comb-drive structure

Figure 13: Schematic of the cross-section of an electrostatic comb-drive

Figure 14: Force-displacement profile for lateral motion of an electrostatic comb-drive [63]

Figure 15: Cross section view of a levitated comb-drive [43]

Figure 16: Cross section view of a transverse motion comb-drive

Figure 17: Schematic of a quadrant of a rotary motion comb-drive [64]

Figure 18: Schematic of a rotary comb-drive (torsional comb)

Figure 19: Layout of electrodes of the proposed microactuator switch design

Figure 20: Microactuator switch at 'OPENED' state

Figure 21: Microactuator switch at 'CLOSED' state

Figure 22: Straight-plate flexure

Figure 23: Fixed-fixed beam flexure [46]

Figure 24: Crab-leg flexure [46]

Figure 25: Folded flexure [46]

Figure 26: Schematic of proposed comb-drive

Figure 27: Folded-flexure supports for microactuator system

Figure 28: FE model of straight-plate flexure

Figure 29: Loading scheme for straight-plate flexure

Figure 30: Nodal solution for Von Mises stresses (straight-plate flexure)

Figure 31: Nodal solution for displacements (straight-plate flexure)

Figure 32: Deformed and undeformed shape (straight-plate flexure)

Figure 33: Graph of applied load against displacement (straight-plate flexure)

Figure 34: FE model of fixed-fixed beam flexure

Figure 35: Loading scheme for fixed-fixed beam flexure

Figure 36: Nodal solution for Von Mises stresses (fixed-fixed beam flexure)

Figure 37: Nodal solution for displacements (fixed-fixed beam flexure)

Figure 38: Deformed and undeformed shape (fixed-fixed beam flexure)

Figure 39: Graph of applied load against displacement (fixed-fixed beam flexure)

Figure 40: FE model of crab-leg flexure

Figure 41: Loading scheme for crab-leg flexure

Figure 42: Nodal solution for Von Mises stresses (crab-leg flexure)

Figure 43: Nodal solution for displacements (crab-leg flexure)

Figure 44: Deformed and undeformed shape (crab-leg flexure)

Figure 45: Graph of applied load against displacement (crab-leg flexure)

Figure 46: FE model of folded flexure

Figure 47: Loading scheme for folded flexure

Figure 48: Nodal solution for Von Mises stresses (folded flexure)

Figure 49: Nodal solution for displacements (folded flexure)

Figure 50: Deformed and undeformed shape (folded flexure)

Figure 51: Graph of applied load against displacement (folded flexure)

Figure 52: Constant stress-time patterns (a) completely reversed, $R = -1$; (b) non-zero mean stress and (c) released tension, $R = 0$

Figure 53: Typical cyclic loading parameters

Figure 54: Three relations: Soderberg, Gerber and Goodman

Figure 55: Schematic of the microactuator switch assembly (plan view)

Figure 56: Schematic of the microactuator switch assembly (isometric view)

Figure 57: Overview of microactuator switch assembly (wafer level)

Figure 58: Isometric view of microactuator switch assembly (wafer level)

Figure 59: Mask 1 (electrical connection)

Figure 60: Mask 2 (electrical contact pads)

Figure 61: Mask 3 (backside etching)

Figure 62: Mask 4 (insulation slot)

Figure 63: Mask 5 (comb finger features)

Figure 64: Mask 6 (shadow mask opening)

Figure 65: Schematic of all masks superimposed

Figure 66: Overview of the layout of all masks

Figure 67: Sputtered alignment marks I (on glass substrate)

Figure 68: Sputtered alignment marks II (on glass substrate)

Figure 69: Sputtered alignment marks III (on glass substrate)

Figure 70: Sputtered Cr/Au electrode contacts I (on glass substrate)

Figure 71: Sputtered Cr/Au electrode contacts II (on glass substrate)

Figure 72: Sputtered Cr/Au electrode contacts III (on glass substrate)

Figure 73: Alignment mark after back etching (on silicon wafer)

Figure 74: Photo-resist patterning for back etching (on silicon wafer)

Figure 75: Structures formed after back etching (on silicon wafer)

Figure 76: SEM photo of structures formed after back etching (on silicon wafer)

List of Figures

Figure 77: Dielectric slot hole (view from top-side of silicon wafer)

Figure 78: Dielectric slot hole (view from backside of silicon wafer)

Figure 79: Dielectric slot hole after SiO₂ growth and Si₃N₄ deposition (top-side view)

Figure 80: Dielectric slot hole after SiO₂ growth and Si₃N₄ deposition (backside view)

Figure 81: Microactuator switch assembly (after final DRIE)

Figure 82: Dielectric slot at the switch contact region

Figure 83: Microactuator switch assembly

Figure 84: An opening of shadow mask wafer

Figure 85: Input sinusoidal waveform

Figure 86: Failure mode I (de-lamination at anchor point of front flexure support)

Figure 87: Failure mode II (de-lamination at anchor point of back flexure support)

Figure 88: Failure mode III (de-lamination at anchor point of back flexure support)

List of Symbols

<u>Symbol</u>	<u>Description</u>	<u>Unit</u>
R_a	surface roughness	m
F_C	contact force	N
F_S	spring force	N
F_{EL}	electrostatic force	N
F_{AD}	adhesion force	N
ϵ_0	permittivity of vacuum	F/m
K	stiffness	N/m
V	actuation voltage	V
C	capacitance	F
C_p	parasitic capacitance	F
A	surface area	m ²
θ	angle	rad
d	comb finger spacing	m
R_c	contact resistance	Ω
f_n	resonant frequency	Hz
P	applied load	N
E	Young's Modulus	N/m ²
I	bending moment of inertia	m ⁴
L	length	m
N	number of comb fingers	-
Δ	switch contact gap	M
ν	Poisson's ratio	-
ρ	density	Kg/m ³
σ_u	fracture stress	N/m ²
R	stress ratio	-
$\Delta\sigma$	stress range	N/m ²
σ_a	stress amplitude	N/m ²
σ_m	mean stress	N/m ²

List of Tables

Table 1: Advantages and disadvantages of MEMS switches [3]

Table 2: Overview of actuation mechanisms (in terms of actuation voltages, displacements and active forces) [3]

Table 3: General specifications of the lateral microactuator switch

Table 4: Summary of parameters for the lateral microactuator switch

Table 5: Loading against displacement values (straight-plate flexure)

Table 6: Loading against displacement values (fixed-fixed beam flexure)

Table 7: Loading against displacement values (crab-leg flexure)

Table 8: Loading against displacement values (folded flexure)

Table 9: Summary of microfabrication process flow for microactuator switch

Table 10: Comparison between specifications and actual values

Chapter 1: Introduction

1.1 Background

As information systems increasingly leave fixed locations and appear in our palms, they are getting closer to the physical world, creating new opportunities for perceiving and controlling our machines, structures and environments. To exploit these opportunities, information systems are required to sense and act as well to compute. Investing engineered system with superior capabilities to sense and act is the driving force for the development of microelectromechanical systems (MEMS) [1].

Microelectromechanical systems technology is a rapidly rising technology that is developed to fulfill the miniaturizing tendency. MEMS are integrated microdevices combining electrical components with active and passive interface functions to the physical surroundings, interacting with motion, sound, light, radio waves, gases, liquids, the chemical environment and thermic radiation etc. Thus, if the traditional microelectronic chip is the 'brain' or the information processing unit, the MEMS part adds the 'senses' to the microsystem.

The variety of new functionalities opens a new world for microdevices, whose impact on society is predicted to become similar to the impact of microelectronics up to today. MEMS promises to revolutionize nearly every product category by bringing together silicon-based microelectronics with micromachining technology, thereby making possible the realization of complete systems-on-a-chip. The high potential of the enabling technology MEMS lies similar to microelectronics, as MEMS fabrication is

based on traditional, highly developed and optimized semiconductor manufacturing processes, infrastructure and logistics. This lead to the possibility of miniaturization with advantageous scaling properties for improved device or system performance, a high level of circuit integration to improve performance or to reduce barriers for incorporation into larger systems, and batch fabrication for very large volume production. MEMS is truly an enabling technology which allows the development of smart products by augmenting the computational ability of microelectronics with the perception and control capabilities of microsensors and microactuators [2-4].

The complexity of the mechanical parts and interfaces of a MEMS device, the reliability issues and the non-standardized packaging procedures, as well as the fact that the production volume and the degree of miniaturization are all decisive for the price of the final device and hence its market potential, have so far led to only a few successful commercialized high volume MEMS products [3].

MEMS will create new capabilities, make high-end functionality affordable to low-end systems, and extend the operational performances and lifetimes of existing products and systems. There are many opportunities for MEMS insertion across a number of technologies and products that include [1,5]:

- Distributed unattended sensors – for asset tracking, border control, environmental monitoring, security surveillance and process control.
- Integrated fluidic systems – for miniature analytical instruments, chip-based DNA processing & sequencing, propellant & combustion control and chemical factories on chip.

- Low-power, high-resolution, small-area displays – for workstation and portable, personal information systems.
- Embedded sensors and actuators – for condition-based maintenance of machines & structures and on-demand amplified structural strength in low-weight systems and disaster-resistant building.
- Mass data storage devices – using magnetic and atomic scale patterning for storage densities of terabytes per square centimeter.
- Integrated microoptomechanical components – for low-power optical communication, displays and fiber-optic switches/modulators.
- Radio frequency (RF) and wireless – for relay and switching matrices, reconfigurable antennas, switched filter banks, electromechanical front-end RF filtering and demodulation.

MEMS, in general, is a miniature device or an array of devices combining electrical and mechanical components, and fabricated with IC (integrated circuit) batch processing techniques. MEMS devices may be fabricated in a number of ways using processes borrowed from classical integrated circuit technology. These processes have been extended to achieve 3-D structures by the techniques of bulk micromachining and surface micromachining. RF MEMS are small mechanical devices fabricated by photolithographic processes, which are specifically used for elemental signal processing functions in RF and microwave frequency circuits.

RF MEMS are micromachined devices interacting with electrical signals up to the radio frequency range. The components of main interest are micromachined switches, mechanically tunable capacitors and three-dimensional inductors, which offer

superior performance compared to their electronic counterparts. Of all the emerging subfields of MEMS with ongoing research and development activities, RF MEMS is believed to have the largest market potential since the high consumer market of personal communication devices already exists and literally cries out for new technologies expanding its possibilities.

Technology reliability, integrability, the demanded short development times and the risk of taking a completely new type of component into a high volume product on a very competitive market have so far inhibited the leap from research laboratories to commercial production lines. High-end applications such as automated measurement and test equipment, automotive safety and communication systems, military and space applications are believed to be the initial application fields of RF MEMS components [3].

RF MEMS switches operate on electrostatic force between two electrodes so they need a low bias current. The power consumption occurs from the dynamic current flow to MEMS bias circuits only when actuation occurs. A voltage excitation is needed to actuate the switch, but once actuated the switches hold their ON/OFF states with very little DC power. MEMS switches can be fabricated on almost any substrates. The MEMS technology leverages previous investments on VLSI processing facilities as they are being manufactured using silicon IC batch-processing techniques. They are easy to integrate in coplanar design.

RF MEMS switches are devices that use mechanical movement to achieve a short circuit or an open circuit in the RF transmission line. Switch contacts are either in

capacitive (metal-insulator-metal) or resistive (metal-to-metal) form. The two main techniques in which RF MEMS switches can be fabricated are [6-8]:

- Bulk micromachining – a process in which large amounts of the substrate are removed.
- Surface Micromachining – a process in which layers are deposited on the surface followed by the removal of a sacrificial layer to release a moving structure.

RF MEMS switches (lateral contact) fabricated via bulk micromachining are parallel-to-plane devices which are made up of cantilever structures; and some designs would require microactuators such as electrostatic comb-drives to provide the linear motion needed for actuation purpose. RF MEMS switches (vertical contact) fabricated via surface micromachining are perpendicular-to-plane devices which are made up of bridge, cantilever or membrane structures.

RF MEMS technology is a relatively new technology which is already finding niche applications. Its low power, high performance and tunability enables potential cost, size, and/or weight improvements in several systems. Currently efforts are underway to establish and improve the reliability of the devices. Comparing to those maturing technology, there is much room for improvement for RF MEMS technology [9].

Microactuators are the key parts of MEMS to perform physical functions. Many types of microactuators have been successfully devised and operated [5]. The microactuators are classified by their actuation mechanisms [10-11]. The actuating force can be generated following two main principles:

- The actuating forces are generated externally in the space between stationary and moving parts using electrostatic [12,13] or electromagnetic fields [14,15] and electrochemical [16] or thermopneumatic [17] effects.
- The actuating forces are generated internally using special materials (also called functional elements) which have intrinsic actuation capabilities including piezoelectric [18], thermomechanical [19], shape memory alloy [20], electrostrictive [21] and magnetostrictive effects [22].

Each actuation principle has its own advantages and disadvantages. The right choice and optimization of the actuation mechanism should be made according to the requirements of a particular application, such as the structural dimensions, technology, response time, force and torque as a function of displacement and the maximum power consumption as well [23].

1.2 Objective

The objective of this research project is to develop a lateral MEMS microactuator switch with a unique dielectric slot for RF switching applications; with low contact resistance, low switching time, moderate power consumption, good structural integrity and high reliability.

1.3 Scope of work

This research will investigate and compare the various designs of the existing lateral microactuator for RF MEMS switches, and propose a more feasible and robust design with features of ease of fabrication, high reliability and improved functionality. The

proposed lateral MEMS microactuator switch will be fabricated via bulk micromachining and silicon-glass wafer bonding technologies.

Various types of micromechanical spring flexure designs will be investigated. Both the structural integrity and stiffness values of the selected micromechanical spring flexure design will be analyzed and verified via the finite element software called ANSYS. A detailed process flow description for the fabrication of the proposed microactuator switch design will be presented. A total of six masks are to be designed and fabricated to cater for the overall fabrication process. The designed microactuator switch assembly will be fabricated solely based on MEMS fabrication techniques. The final microactuator switch design is to be fabricated, followed by mechanical characterization and testing for the various characteristics and specifications (e.g. actuation voltage, contact resistance, switching time and switching life).

1.4 Report structure

The report is structured as follows:

- Chapter 2 presents the fundamental MEMS fabrication technology. Literature reviews are done on the development of RF MEMS, various types of MEMS switches, microactuators for RF MEMS switches and their applications. The various types and applications of microactuator RF MEMS switches are investigated and discussed. The design considerations of electrostatic metal-to-metal contact switches are also discussed.
- Chapter 3 presents the theories of electrostatic actuation (comb-drives) and the stiffness simulation of micromechanical spring flexures. The detailed

calculations leading to the final proposed microactuator switch design are documented and presented.

- Chapter 4 provides a brief background and theory behind the finite element method (FEM). The FE analysis of a few micromechanical spring flexure designs is presented for the verification of their stiffness values against theoretical values. FE analysis is also used to analyze the selected spring flexure design structurally. The general theory of fatigue analysis is included in the chapter.
- Chapter 5 covers in detail the proposed process flow for the fabrication of the lateral microactuator switch assembly. The mask layout design includes a total of six layers. All the required mask designs generated using a software called ‘L-Edit’ are presented and discussed. In the entire fabrication process, thin film deposition, lift-off process, photolithography, deep reactive ion etch (DRIE) and wafer bonding technologies are used. The microactuator switch is fabricated on a silicon wafer, later to be bonded to a glass substrate. The complete fabrication progress and results are presented and discussed.
- Chapter 6 gives a summary on the various test results obtained, followed by a general discussion.
- Chapter 7 presents the conclusion to the research project. Some recommendations for future research work are proposed.

Chapter 2: Literature Review

2.1 MEMS fabrication technology

The initial development of MEMS technology was in the 1960's using fabrication facilities developed for VLSI technology. While the electronics were fabricated using integrated circuit (IC) process such as CMOS or BICMOS, the micromechanical components were fabricated using compatible micromachining processes that selectively “machine” or etch away parts of the silicon wafer, or add new structural layers to form the mechanical and electromechanical devices [24].

The fabrication process to realize MEMS is a combination of conventional IC processes and specialized technologies which are unique to silicon micromachining. Micromachining is the key to technology for the fabrication of solid-state MEMS devices such as microactuators and microsensors. The technologies concerned are bulk micromachining, surface micromachining and micromoulding technologies, including classical electroplating, the HexSil [25] and the LIGA [26] process.

2.1.1 Bulk micromachining

Bulk micromachining is a process whereby the silicon substrate is selectively removed to shape and form the desired micromechanical elements. It is in fact a subtractive process. Figure 1 shows a typical bulk micromachined structure.

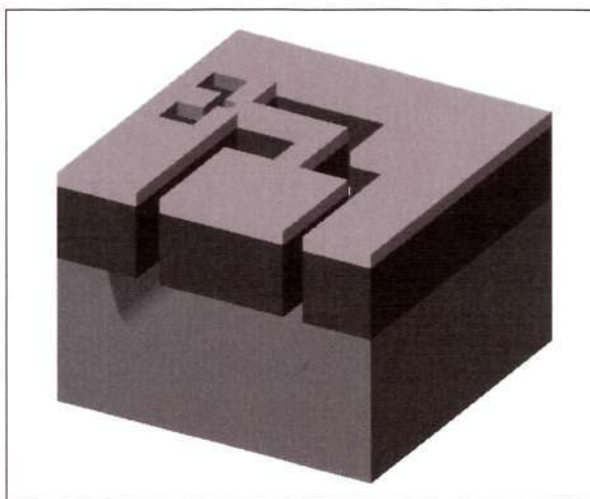


Figure 1: Bulk micromachined structure

There are many fabrication methods of machining the silicon substrate. The typical methods include isotropic etching, anisotropic etching, electromechanical etching, spark milling, mechanical milling, ultrasonic milling, laser etching, plasma-phase or dry etching etc [27].

Bulk micromachining is essentially the formation of a desired microstructure via utilization of the bulk of the structure. This extension of definition includes the widespread use of wafer bonding technology.

Currently, the introduction of deep reactive ion etching (DRIE) process provides a powerful tool for bulk micromachining to etch very deep trenches (up to a depth of 500 μm) with nearly vertical sidewalls [28,29]. DRIE is evolved from the need of anisotropically etching trenches with high aspect ratios at a high etch rate. The high selectivity to silicon dioxide for the DRIE process makes it possible to etch deep trenches and stop on a buried layer of silicon dioxide e.g. silicon-on-insulator (SOI) wafers.

For wet bulk micromachining, the features are sculpted from the bulk material such as silicon, SiC, quartz and glass; by orientation-dependent (anisotropic) or orientation-independent (isotropic) wet etchants. Isotropic etchants will etch in all crystallographic directions at the same rate, and are usually acidic in nature e.g. HNA (HF/HNO₃/ CH₃COOH). Isotropic etching will produce rounded isotropic features in single-crystal silicon. The simple KOH water system is the most popular etchant used for the case of anisotropic etching of single-crystal silicon. In near saturated solutions (1:1 in water by weight) at a temperature of 80°C, this etching method produces a uniform and bright surface. The solution attracts {1,1,1} plane types, which have a high bond density, in a much slower rate than other plane types (the side wall of {1,1,1} is at an angle of 54.74° to the surface) [24].

Bulk micromachining is a relatively straightforward process that does not require elaborate equipment. Nevertheless, this method has its disadvantages. The etchant chemical commonly used in bulk micromachining are often incompatible with IC or IC fabrication equipment. In addition, bulk micromachining inherently consumes an inordinate amount of wafer surface area as compared to other technologies, and is usually more costly. However, despite these limitations, silicon bulk micromachining is still the most widely used micromachining technology, and this trend will probably continue to be so for the immediate future.

2.1.2 Surface micromachining

Surface micromachining is a microfabrication process whereby the micromechanical structures or devices are made or built entirely on the surface of the wafer without penetrating the wafer surface. Surface micromachining is an additive process.

Typically, the desired micromechanical structure is built up by depositing and patterning thin-films of both structural and sacrificial material on the substrate surface. The most commonly used structural layer is polysilicon (Poly-Si) or silicon nitride (Si_3N_4) [24].

Figure 2 illustrates a generic surface micromachining process flow of a doubly-anchored polysilicon bridge. First a sacrificial material such as silicon dioxide (SiO_2) or PSG (Phosphosilicate glass) is deposited onto the substrate. The purpose of this sacrificial material layer is to provide a temporary stand-off from the substrate during the subsequent processing to form the structural layer. After deposition, the sacrificial layer is etched into the desired pattern. Openings are etched entirely through the sacrificial layer so as to provide anchoring points for the structural layer. This prevents the structural layers from ‘floating’ away during the release step at the end of the process. Next, a thin-film layer of the structural material is deposited and etched. After etching, the sacrificial layer is removed by immersion into a wet etchant, thereby leaving behind the released structural layer [30].

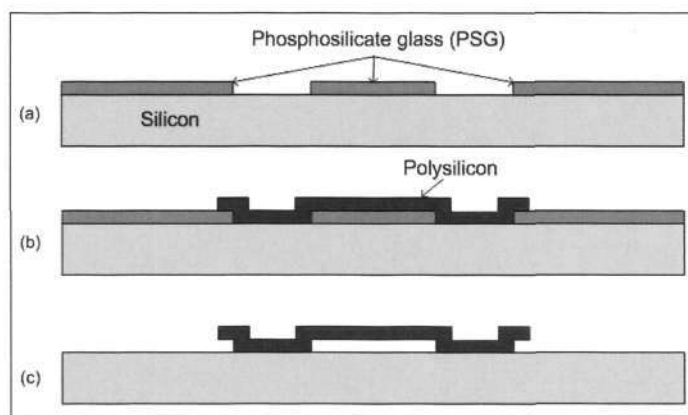


Figure 2: Generic surface micromachining process to fabricate a doubly-anchored poly-silicon bridge: (a) deposition and patterning of sacrificial PSG layer; (b) deposition and patterning of polysilicon structural layer; (c) release of structural layer by removal of sacrificial layer [30].

The key advantage of surface micromachining is its compatibility with conventional IC processing. Surface-micromachined micromechanical devices are fabricated using standard IC thin-film deposition and patterning technologies without resorting to potentially contaminating chemicals or non-standard processes. Another advantage of surface micromachining is that the size of the devices is not constrained to the minimum device dimensions. Instead, surface micromachined devices can be reduced to a much smaller size than that made with bulk micromachined components.

The major disadvantage of surface micromachining is that the technology is inherently a two-dimensional planar process that can possibly limit the flexibility of the design. Surface micromachining is a relatively new technology compared to bulk micromachining, and has not been widely employed in commercial production. However, it is expected to become a preferred method of fabrication in the future due to cost savings and compatibility with integrated circuit processing.

2.1.3 Micromoulding

Micromoulding is a micromachining process whereby high-aspect-ratio (depth to width) devices are created on the surface of silicon wafers. Micromoulding is capable of fabricating components having small lateral dimensions (as small as 1 or 2 μm) and comparatively large vertical dimensions (10 to over 500 μm). Micromoulding processes can be divided into three main groups: classical electroplating, LIGA and HexSil processes. All moulding technologies allow high aspect ratios, but the mechanical structures are simpler and less diverse as compared to structures fabricated via surface micromachining.

The classical electroplating technology uses photo-resist or other photo-structural, organic materials for the female form of the structures. They are deposited on various substrates with low resistivity or metal coating (starting layer) [31]. After the moulds have been patterned, metals like Ni, Cu or alloys are grown into the moulds by the electrodeposition process starting from the metal layer. Similar to surface micromachining technology, sacrificial layers can be used to realize bridges, suspending beams or sliding anchors. The structures are freed by stripping the photo-resist. Each mould can only be used once.

The LIGA process (lithographic, galvanofornung and Abformung) was developed at Forschungszentrum Karlsruhe, Germany. This process starts with a thick layer (up to 500 μm) of PMMA (polymethylmethacrylate) that is deposited onto a metal substrate. The structures are patterned by parallel and high-energy X-ray lithography. The gaps are filled up with metal (Au, Cu etc.) by the electrodeposition process. The electroforming process starts on the metal substrate. The high fidelity of the LIGA photoengraving process allows very dense patterns with very small dimensions to be faithfully reproduced in the PMMA material. Mass production of polymers, metals and even ceramic microcomponents makes use of hot embossing and injection moulding. Cantilever LIGA-structures can be realized by sacrificial layer etching (e.g. titanium). However, LIGA processing requires a synchrotron radiation source and therefore has limited accessibility [32].

The HexSil process was developed at U.C. Berkeley [33]. The process uses a low-pressure chemical vapor deposition (LPCVD) process and silicon moulds fabricated by DRIE of silicon wafers. The HexSil process allows the fabrication of high-aspect-

ratio molded CVD polysilicon structures. The key feature of this process is that it relies on a reusable silicon mold, significantly lowering the final unit cost of finished parts. After fabrication, the finished structure is solder-bonded to a target substrate, and the mold wafer is then ready for the next fabrication cycle.

2.1.4 Main microfabrication techniques for proposed microactuator design

The proposed microactuator RF MEMS switch design is a parallel-to-plane device that actuates switching motion parallel to the wafer plane (lateral contact). The two main microfabrication techniques used in this proposed design are the deep reactive ion etching (DRIE) process and the silicon-glass wafer bonding process. The DRIE process is essential to achieve comb-drive structures of a high aspect ratio while the wafer bonding process is required to bond the silicon wafer to a glass substrate electrostatically.

2.1.4.1 Deep reactive ion etching (DRIE)

The etching process in microfabrication can be classified into two main categories: wet etching and dry etching; each with further subdivisions of isotropic (orientation independent) and anisotropic (orientation dependent) etching. Deep reactive ion etching (DRIE) is a highly anisotropic etching process developed in the semiconductor industry and used to create deep and high aspect ratio channels in materials such as silicon. DRIE is a dry anisotropic etching technique that has been widely used for MEMS and high value integrated capacitors; channels with vertical sides and having aspect ratios greater than 20:1 can be produced. This process is also known as advanced silicon etching. The etch mask to be used in the DRIE process is the simple photo-resist mask.

Figure 3 shows the setup for a DRIE process. There are three primary processes which are brought together to achieve the results in DRIE. First a highly reactive gas is used to perform an isotropic etch of the substrate. After a brief period the etching is stopped and the process switches over to deposition of a layer of passivation over the whole surface. This protects the substrate from further chemical attack and prevents further etching. The process now returns to etching, which is where the third process comes into play. Within the chamber there is an energetic plasma which produces a collimated stream of ions that bombard the substrate. By a process of sputtering these ions remove the passivation from the bottom of the previous etch step, but not from the sides. The etchant chemicals can then erode only the bottom of the channels [24].

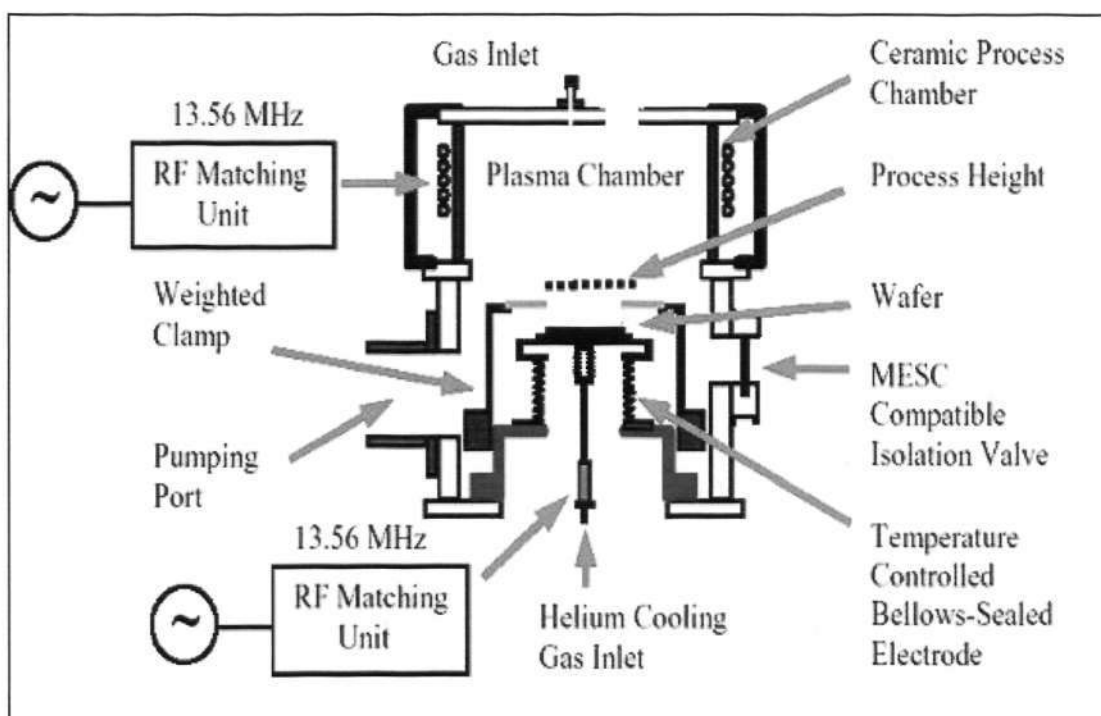


Figure 3: Setup for deep reactive ion etching (DRIE) process

The process is repeated many times resulting in a large number of very small isotropic etch steps taking place only at the bottom of the etched pits. It is this selectivity that

leads to the overall anisotropy of the process and the creation of high aspect ratio channels with vertical sidewalls.

Figures 4 and 5 show the sequence of steps in a typical DRIE process.

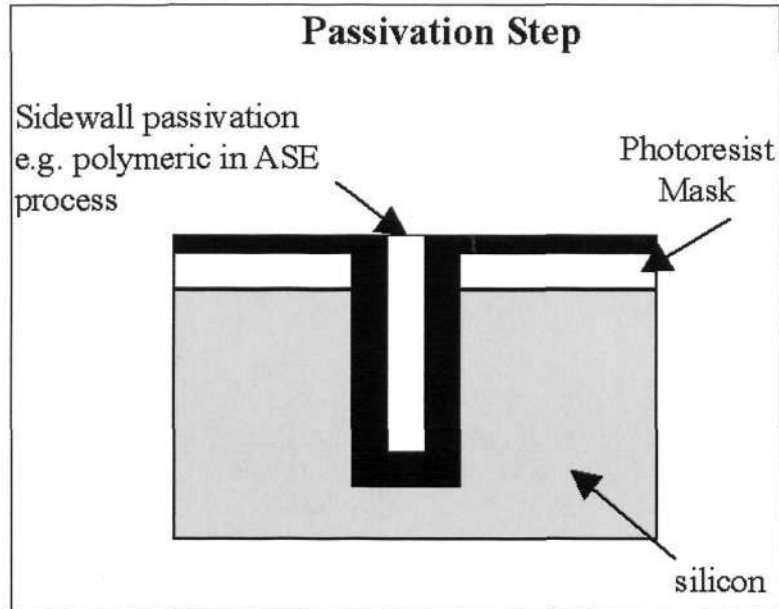


Figure 4: Passivation step in DRIE process

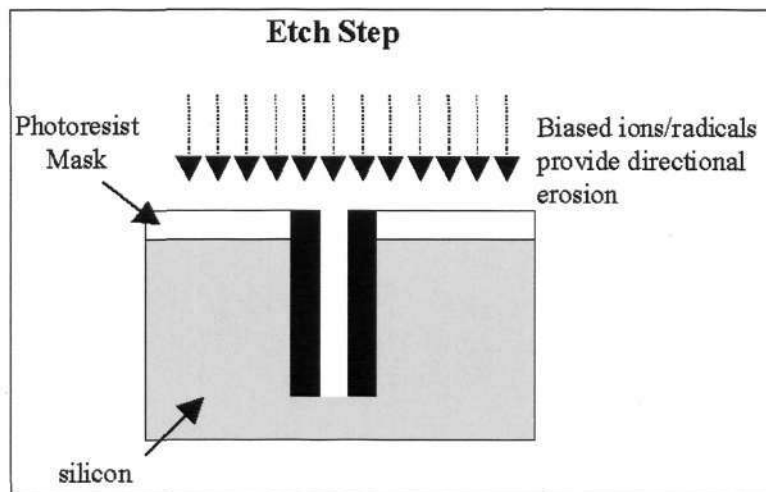


Figure 5: Etch step in DRIE process

Consider a simplified advanced silicon dry etch process based on $\text{SF}_6/\text{C}_4\text{F}_8$. Note that the gas C_4F_8 is for passivation purpose while SF_6 is for etching purpose. The steps in the process are listed in sequence as follows:

- Dissociation of precursor gas (C_4F_8) by plasma to form ions/radicals that form the passivating polymeric layer.
- Gases are switched from C_4F_8 to SF_6 .
- Dissociation of SF_6 by plasma to form ions/radicals.
- Removal of passivation layer.
- Etching of silicon.

Figure 6 shows an overview of the advanced silicon etch process.

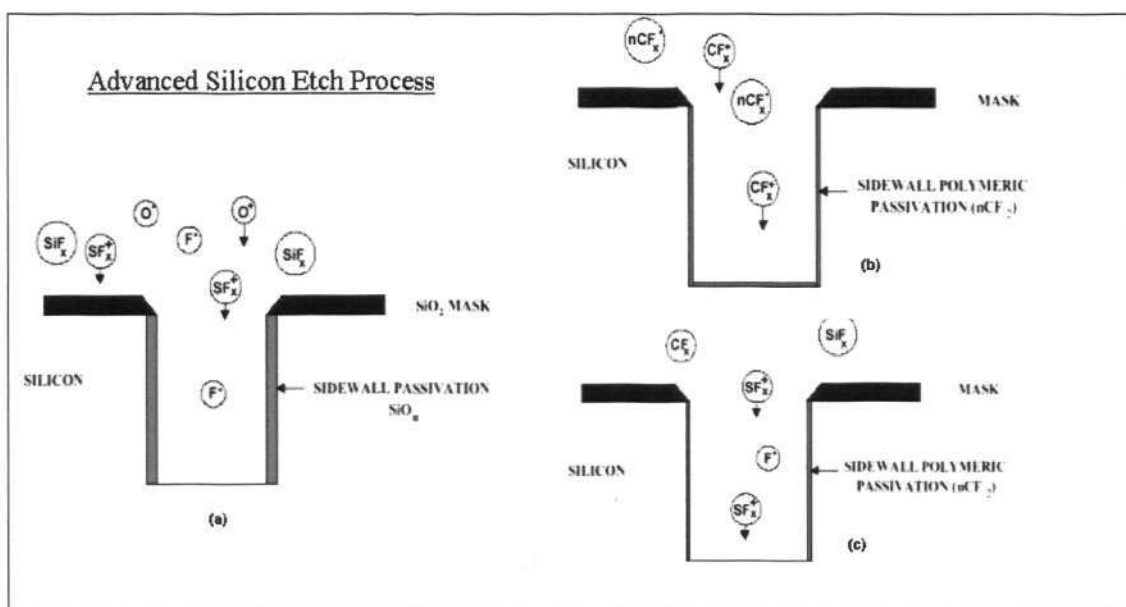


Figure 6: Overview of advanced silicon etch process: (a) simultaneous sidewall passivation; (b) deposition process; (c) etching process

2.1.4.2 Wafer bonding

There are a few types of wafer bonding processes, mainly anodic bonding, thermal silicon fusion bonding, thermal bonding and eutectic bonding. The anodic wafer bonding process will be discussed in detail in this section since it is the wafer bonding process to be adopted and is most suited and commonly used for bonding silicon to glass.

The anodic wafer bonding process is a field-assisted thermal bonding process that is used to join silicon to glass. The process is a relatively low-temperature process in which both silicon and glass remain rigid throughout the process. Bonding process can take place in either atmosphere or vacuum at temperatures ranging from 180°C to 500°C, with typical voltages of 200V to 1000V; all depending on the thickness of glass and temperature. The operating temperature is chosen to be near to the glass-softening point and well below its melting point. The bonding process can be achieved in very short time under the most suitable conditions [24].

Figure 7 shows a schematic of an anodic wafer bonding process.

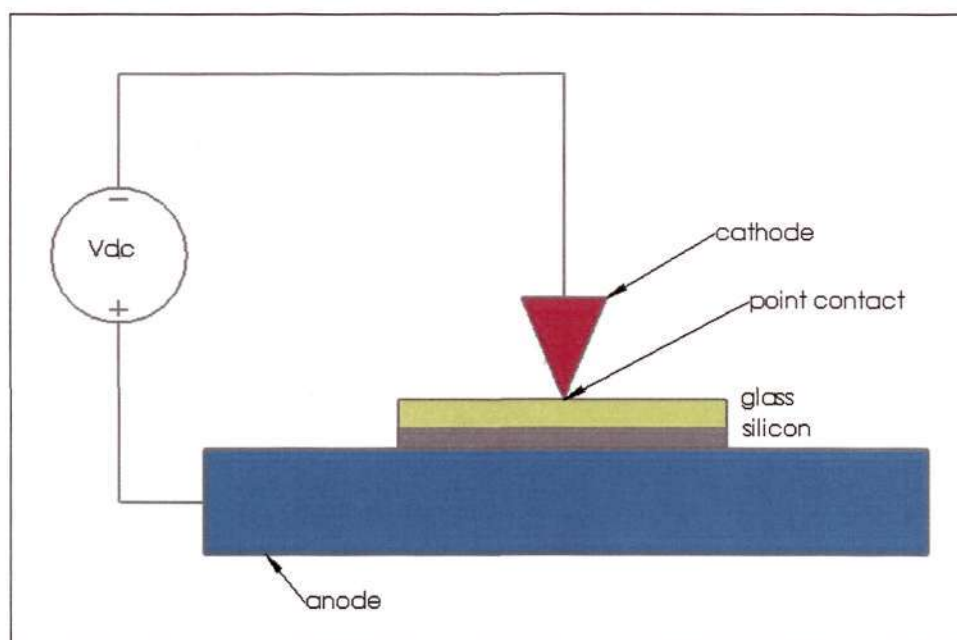


Figure 7: Schematic of an anodic wafer bonding process [24]

With reference to Figure 7, the glass wafer is placed on top of the silicon wafer and makes a point contact to the uppermost surface of the glass wafer, which is held at a constant negative bias with respect to the grounded silicon wafer. Looking through glass, the bonded region can be seen to move outwards from the cathode pin-point by

the disappearance of interference fringes. A constant voltage supply is preferred since this prevents dielectric breakdown after the bonding process is completed and the interface becomes an insulator.

Some main precautions to be taken for the anodic bonding process are:

- Contact surfaces must be flat ($R_a < 1\mu\text{m}$)
- Dust-free
- Thickness of native (or thermal) oxide coating on silicon wafer surface must be less than $0.2\mu\text{m}$.
- Thermal expansion coefficients must match.

The actual bonding mechanism is not well understood. However, it is thought that at elevated temperatures, the glass becomes a conductive solid electrolyte and bonding results through the migration of Na ions (pyrex glass contains ~ 3%-5% Na) towards the cathode. As it moves, a space charge (bound negative charge) is left behind in the region at the glass-silicon interface. Most of the applied voltage drop occurs across this space charge and the high electromagnetic field results in an electrostatic force that pulls both the glass and silicon wafers into intimate contact.

The main problems encountered in the anodic bonding process are a need for high voltages, thermal/mechanical stresses arising due to a mismatch in thermal expansion coefficients and the viscous behavior of glass (degraded long-term stability of components).

2.2 RF MEMS switches

2.2.1 Overview of RF MEMS

The first MEMS switch was fabricated back in 1979 by K. E. Petersen [34], showing the possibilities of the emerging micromachining technology. In 1991, L. E. Larson presented a MEMS switch dedicated to switching RF signals up to a few tens of GHz [35]. Despite the immaturity of the device, its electrical signal characteristics were so remarkable that it brought many research institutes and universities on the track of RF MEMS. In the middle of the nineties of the last century, one publication followed another on new RF MEMS device concepts, and by the end of the nineties the research included more and more device reliability issues, indicating the increasing matureness of the technology. The device of main interest, due to its excellent performance, was and still is the micromachined switch [3].

Other RF MEMS components are mechanical, dielectric and cavity resonators for frequency-selecting applications, tunable capacitors, three-dimensional inductors, as well as micromachined antennas and transmission lines. RF circuits based on MEMS components are wide-band phase-shifters realized with MEMS switches or micromachined tunable capacitors, reconfigurable antennas, voltage controlled oscillators and impedance tuning circuits, just to give a few examples [3].

On the whole, all these devices are characterized by their outstanding performance: low insertion loss and high signal linearity for the switches; high frequency selectivity and very small chip size of filters based on mechanical

resonators; high quality factor (Q) value and high self resonance frequency (SRF) of micromachined inductors; high tuning range, low series resistance and high linearity of mechanically tunable capacitors. On the other hand, due to high complexity in fabrication, many issues have surfaced. The main common issues encountered are reliability issues and the difficulty of integration with traditional electronic circuits due to their special packaging requirements and device specific problems (e.g. high impedance of micromechanical resonators and the relatively low power handling ability of MEMS switches) [3].

Wireless MEMS is a term often used synonymously with RF MEMS and indicates the market potential of MEMS components in consumer products with telecommunication functionality, demanding low size, low weight, low power consumption, reconfigurability and good signal properties to fulfill new telecommunication standards. These requirements make RF MEMS devices very suitable for replacing bulky passive off-chip components, which currently inhibit further miniaturization of wireless equipment since they consume most of the circuit board size and, in contrast to RF MEMS devices, cannot be integrated on-chip without sacrificing performance [36].

2.2.2 Miniaturization of mechanical switches

The development of digital switches (transistors) in logic devices has proceeded at an incredible speed over the last decades in terms of components per chip, cost per function, clock rates, power consumption, compactness and functionality [37]. However, the limits of digitally controllable analog signal switches have not been advancing and matching that fast pace, and electronic

switches based on PIN diodes and field effect transistors (FET) can hardly meet the performance requirements of today's communication systems, especially concerning the isolation, the insertion loss (on resistance) and the signal linearity. Even though semiconductor-based switches have been improving over the last decade, their RF signal performance still decreases drastically with frequency above 1 GHz where they are limited either in power handling or they show a very large insertion loss, poor isolation and high signal distortion [38].

However, MEMS switches perform very well over an extremely large bandwidth with very uniform characteristics, even above 100 GHz [39]. That is the advantage of having a purely mechanical element opening and closing (short-circuiting) an almost unimpaired transmission line.

Unfortunately, MEMS switches also have some obvious disadvantages, which are tabulated and compared to their advantages in Table 1. This problem (listed under disadvantages in Table 1) has inhibited the leap from the “lab to the fab”, since so far no system and component manufacturer has dared to take the risk of embedding a device uncertain in its reliability and lifetime into a volume product [3].

Table 1: Advantages and disadvantages of MEMS switches [3]

Advantages	Disadvantages
very high DC and RF isolation	high actuation voltages (for electrostatically actuated switches)
very low insertion loss	low switching speeds
high signal linearity	limited power handling

almost zero power consumption (for electrostatically actuated switches)	uncertain lifetime
very large bandwidth (no compromise on performance)	problematic integration with RF circuits
miniaturization	special packaging necessary
simple control circuits	uncertain reliability
possible high volume production	uncertain price
Highly resistant to external influences (temperature, radiation, mechanical shock etc.)	

Even from a MEMS perspective, a micromachined switch, especially a DC metal contact switch, is a mechanically rather problematic and complicated device as compared to other typical MEMS devices. However, because of their market potential, MEMS switches are attracting a lot of attention from universities, research institutes and industries. The need of better signal switching properties in more sophisticated telecommunication standards and in high-end applications might compensate for the technological skepticism.

2.2.3 MEMS switch types

A MEMS switch is a bistable mechanical device fabricated by micromachining techniques, allowing the free propagation of an electrical signal from an input to an output in one state and blocking the signal in the other state. Stability in one or both of the states is achieved with or without applying an external energy source, and the transition between the two states is controlled by imposing or releasing the external effort [3].

RF MEMS switches can be classified by their actuation principle, by the circuit configuration, the fabrication technology or by the intended application. About 80% of the switches presented so far belong to the two most common switch types, schematically illustrated in Figure 8:

- Electrostatically actuated series switches with metal contacts: A cantilever or membrane with a switching metal contact bar vertically opens or closes the signal line. Switches of this category are normally OFF, and the incoming RF wave is reflected by the interrupted signal line in the OFF state. In the ON-state, the signal can propagate over the metal contact bar short-circuiting the gap between the input and the output line. This switch type is capable of switching DC to RF signals and is both in its fabrication and in its reliability more complicated than the next type, mainly because of its metal contacts.
- Electrostatically actuated capacitive shunt switches: Consist of a metal bridge or membrane connected to RF ground and moving vertically above the isolated signal line. The switch is normally ON, and in the down position, the bridge capacitively short-circuits the signal line to the RF ground. Thus, in the down-state (OFF-state), the signal propagates via the bridge to the ground and the isolation mainly depends on the parasitic inductance of the whole ground path. This switch type is basically not suitable for low frequency signals. It is relatively simple in its fabrication, very fast with a switching time of only a few microseconds, and very small compared to the metal contact switches which need a stronger actuator to obtain the necessary contact and opening forces.

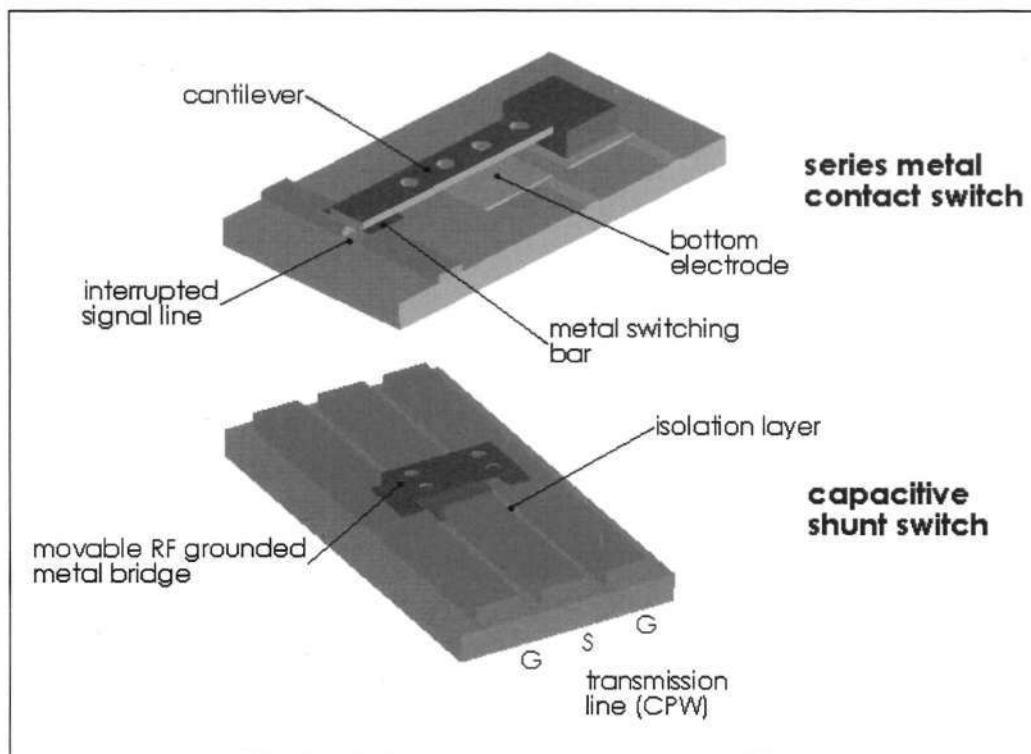


Figure 8: Most common electrostatically actuated MEMS switch types [3]

It should be noted that another type of MEMS switch, which are similar in concept but a variation to the first switch type as discussed, is known as the microrelay. Microrelays are highly miniaturized metal-contact relays fabricated by micromachining techniques. The most common actuation mechanisms are electrostatic, magnetostatic or electrothermal. The relays are designed with larger contact and restoring forces from a few to a few tens of milli-Newtons to be able to handle currents over 10mA. The contact resistance is rather small in the range of a few hundred milli-Ohms or lower. The contact distance in the OFF-state should be at least 10-20 μm to provide sufficient DC isolation in air. Reliability is a big issue for this type of switch, since the relatively weak MEMS microactuator has to open contacts carrying larger currents. A longer switching time in the millisecond region is tolerated by most of the target applications.

2.2.4 Electrostatic microactuator for RF MEMS switches

Electrostatic microactuators which are driven by electrostatic forces have been widely studied and investigated. The one remarkable advantage is their suitability for miniaturization, easy integration on a chip, easily controllable and low power consumption. They require only thin plane electrodes to produce electric field and do not require large and heavy three-dimensional structures such as iron cores and coils found in traditional electromagnetic motors. The electrostatic microactuator is driven essentially by voltage. It is easy to control with high switching speeds and has low power consumption and high efficiency.

An electrostatic microactuator design is chosen for this research project for the ease of fabrication. The structural material of the device needs only to be conductive, rather than ferromagnetic or piezoelectric. Furthermore, electrostatic microactuators allow high accuracy, capacitive measurement of displacement, and are capable of high bandwidth operations.

Many types of electrostatic microactuators for RF switching applications have been proposed. The actuation mode of the microactuators can be classified into two main categories [3]:

- Parallel-to-plane devices: These devices are made up of cantilever structures; and some designs would require microactuators such as electrostatic comb-drives to provide the linear motion needed for actuation purpose. Most of the parallel-to-plane devices are fabricated via bulk micromachining and actuation motion is in a direction parallel to the wafer plane (lateral contact).

- Perpendicular-to-plane actuation: RF MEMS switches fabricated via surface micromachining are perpendicular-to-plane devices which are made up of bridge, cantilever or membrane structures. The actuation motion is in a plane perpendicular to the wafer plane (vertical contact).

Among the linear microactuators, the interdigitated finger (also known as the comb-drive) structures are well researched and commonly used, which was first demonstrated by William chi-keung, Tang [40-42]. The actuator is a laterally-driven polysilicon microstructure parallel to the plane of the substrate.

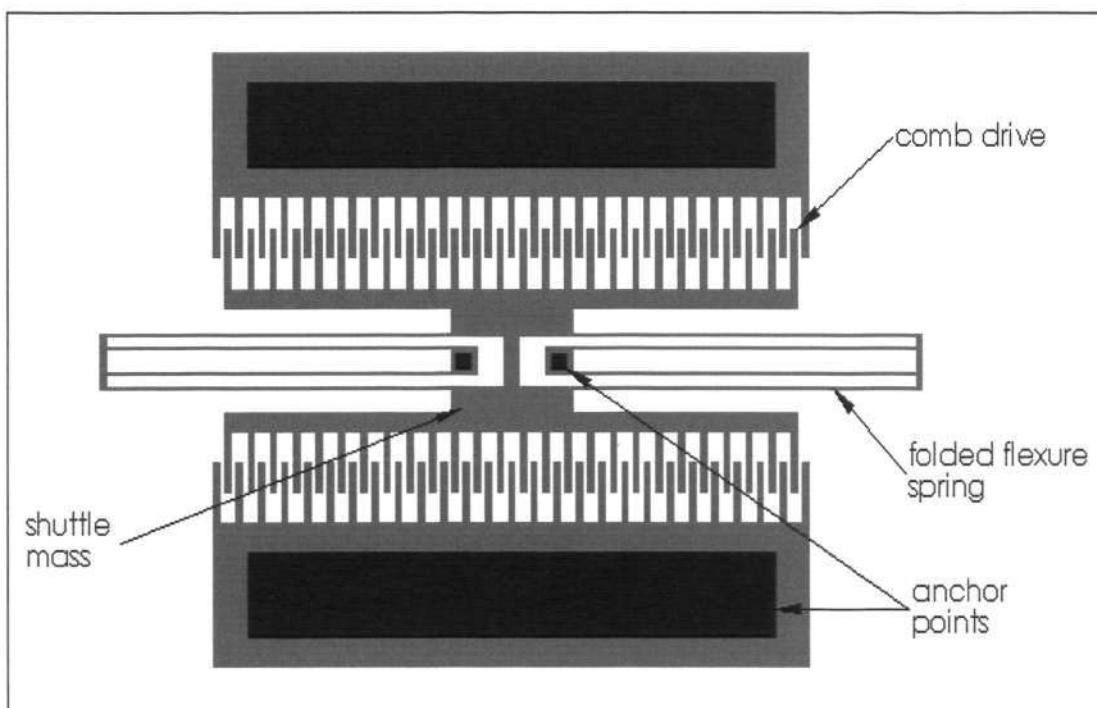


Figure 9: Laterally driven electrostatic comb-drive resonant microactuator [41]

Figure 9 shows the layout of a linear electrostatic comb-drive resonant structure that can be electrostatically driven from one side and sensed capacitance at the other side with interdigitated finger (comb) structures. Note that the regions in black color are the locations where the polysilicon structures are anchored or fixed to the

bottom layer. The rest of the entire structure is suspended above the bottom layer. The resonant microactuator consists of a movable central shuttle mass that is suspended by folded-flexure springs on either side. The other ends of the folded-flexure springs are fixed to the bottom layer. The microactuator can be thought of, as a spring-mass-damper system, the damping being provided by the air below and above the movable part. By applying a voltage across the fixed and movable comb fingers, an electrostatic force is produced which sets the mass into motion in the lateral direction (operational direction) [43].

Electrostatic comb-drive microactuators are widely used because their output force can be easily controlled by the applied voltage and have high efficiency i.e. a high proportion of the output force needed to drive passive structures is extracted more than in rotational actuators. Many researchers have since engaged in the shape design, fabrication and operation of comb-drive microactuators [42-49].

2.2.5 Application of MEMS switches

MEMS switches are intended to switch the propagation path of an analog signal with very high signal purity. This function might be used to connect/disconnect an electrical potential, or to select signals (e.g. incoming and the outgoing signal of an antenna) or to reconfigure a sub-system. Typical applications of the latter type are switching of filter banks, tuning of filters by switching capacitors or inductors, switching of delay lines in phase-shifters, impedance matching by switching stub-lines or capacitors, and configuration of antenna patterns or frequencies by switching antennas or parts of an antenna.

Depending on the frequency specifications, either capacitive or metal contact switches are preferred for certain applications.

To switch DC to RF signals, typically required in high-quality test and measurement equipment, the most demanded properties are an extremely large bandwidth from DC to a few tens of GHz with very good signal properties over the whole bandwidth. The switching speed and the power consumption are less important. Metal contact switches are good candidates for these applications.

Microrelays are intended for applications in which DC to low frequency currents have to be switched. Here it is important to galvanically decouple the input from the output in the OFF-state, and to have a small series resistance for a low voltage drop and low power dissipation in the ON-state.

Military and space applications also favour MEMS components because of their robustness against external influences such as radiation, temperatures and strong electromagnetic fields, and because of their high shock resistance. Switch reliability and a large number of switching cycles of the order of tens of billions are equally important for most applications. It can be expected that MEMS switches are first going to be introduced in less cost critical areas before they might be considered for low-cost, high volume markets.

2.3 Design considerations of electrostatic metal-to-metal contact switches

This section addresses some selected important design problems of electrostatically actuated metal-to-metal contact switches. The various design parameters and their influence on each other for the MEMS switch design are reported and discussed. The dominant reliability problems of contact switches are also included.

2.3.1 Actuation voltage, displacement, contact and restoring forces

These four switch parameters are tightly coupled to each other, which makes good switch design very difficult. Figure 10(a) is a schematic drawing of a simple electrostatically actuated cantilever switch, and Figure 10(b) shows a simplified quasi-static electromechanical equivalent circuit model of such a cantilever-spring or membrane spring based switch. These are the most common MEMS series switch types and are discussed in this section. The active forces, when establishing the contact and when opening it, are illustrated in Figure 10(c). The overall goal of any switch design is to balance these forces to achieve the desired contact performance, expressed in the contact resistance and in the contact reliability [3].

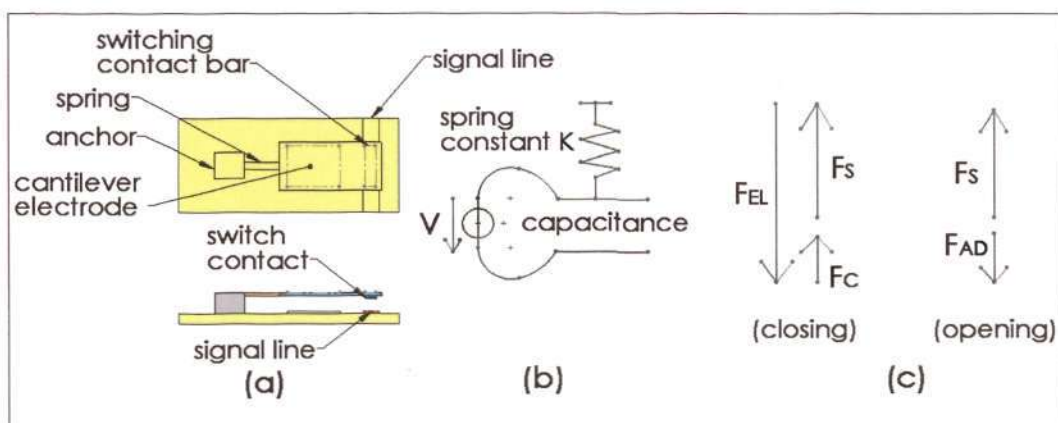


Figure 10: (a) Top and end view of a cantilever based switch; (b) simplified mechanical equivalent circuit model; (c) active forces and when opening the contact

Basically, a high contact force F_C results in low contact resistance, and a high restoring force is desired to prevent contact stiction caused by microwelding. A high restoring spring force F_S can be achieved by a relatively stiff structure and a large displacement, both requiring an increased electrostatic force F_{EL} to pull down the structure. Also, increasing the restoring force demands an even stronger electrostatic actuator to maintain the desired contact force (see Figure 10c). The electrostatic force can only be increased by the actuation voltage or by a larger actuation electrode area, resulting in a larger switch size. To complicate it even more, the effective restoring force is the spring force minus the adhesion force F_{AD} . The adhesion force generated upon contact between the two bodies is very difficult to predict or to control, since the contact physics in microswitches is still not very well understood [50-51].

The actuation voltages of current electrostatic switch designs are between 15V and 80V to achieve sufficient switching performance [52-53]. These voltages are by far not compatible with the voltage levels used in electronic products. Thermal and magnetostatic actuators can be designed in a way resulting in actuation voltages below 5V, but their high power consumption, unless using a bistable latching mechanism, is even less acceptable especially when targeting wireless applications. Also, switches based on electrostatic actuation are the most promising designs in terms of reliability and wafer-scale manufacturing possibilities [52]. Another strong advantage of electrostatic actuation mechanisms is the fact that the maximum force is created in the end position with touching contacts.

The pull-down voltage is the voltage in which the cantilever beam will snap on and make physical contact when the actuation voltage attains this value. The pull-down voltage required by a switch as illustrated in Figure 10(a) can be calculated approximately with the simplified mechanical model shown in Figure 10(b).

The electrostatic force and the restoring spring force are given by [38]:

$$F_{EL} = \frac{1}{2} \varepsilon_0 \varepsilon_r \frac{A}{(d-y)^2} V^2 \quad [1]$$

$$F_S = -ky \quad [2]$$

where ε_0 = permittivity of vacuum

ε_r = effective relative permeability

A = electrode area

d = initial distance between electrodes

V = actuation voltage

k = spring constant (reflecting mechanical stiffness)

y = deflection of cantilever beam

The upper electrode snaps against the lower one if the electrostatic force is larger than the spring force. That is the case when the distance between the electrodes falls below a critical distance, and can be explained by the positive feedback mechanism in the electrostatic actuation. The attracting electrostatic force grows with the square of $\frac{1}{d}$, whereas the restoring spring force only grows linearly with the distance. The critical distance is $y = \frac{1}{3}d$ and is independent of the design geometry [53].

Thus the pull-down voltage of the cantilever switch can be estimated by:

$$V_{\min} \geq \sqrt{\left(\frac{2}{3}\right)^3 \frac{kd^3}{\epsilon_0 \epsilon_r A}} \quad [3]$$

From Equation [3] it can be seen that the minimum required actuation voltage is proportional to $d^{\frac{3}{2}}$ and inversely proportional to \sqrt{A} . A stiff structure results in a larger restoring force, but requires either larger electrode areas or a higher actuation voltage unless the electrode distance is very small, which basically decreases the signal isolation because the contact distance is then also smaller for the discussed model. It is not easy to create an effective switch design with low actuation voltages (for electronic compatibility), small electrode areas (for small chip size and low cost per switch) and large contact distance (for high isolation), by maintaining a reasonable restoring force (for contact reliability) and contact force (for low resistance) [3].

The following table provides an overview of the actuation voltages, displacements and active forces in electrostatically actuated switches as compared to a few alternative actuation mechanisms with zero power consumption in both the ON and OFF states.

Table 2: Overview of actuation mechanisms (in terms of actuation voltages, displacements and active forces) [3]

Actuation mechanism	Advantages	Disadvantages
Electrostatic actuators	<ul style="list-style-type: none"> • simple in fabrication and operation • maximum force in 	<ul style="list-style-type: none"> • requires relatively high actuation voltages

	<ul style="list-style-type: none"> • contact position • strong contact force • pull-in hysteresis 	<ul style="list-style-type: none"> • displacement limited to a few μm
Electrothermal lateral actuators (with mechanical latching mechanisms)	<ul style="list-style-type: none"> • large displacement • low actuation voltage • simple fabrication 	<ul style="list-style-type: none"> • very large size • maximum force during transition and not at end positions • small contact forces
Electrothermal actuators (with electrostatic clamping)	<ul style="list-style-type: none"> • low voltage • large displacement • maximum force in contact position • large contact force • small size 	<ul style="list-style-type: none"> • complex fabrication
Magnetostatic actuators (latching by switching magnetic polarization)	<ul style="list-style-type: none"> • low actuation voltage • restoring force controllable by actuation current to a certain extent 	<ul style="list-style-type: none"> • low displacement • low contact force • low restoring force • complex fabrication
Piezoelectric actuators	<ul style="list-style-type: none"> • acceptable contact force 	<ul style="list-style-type: none"> • low displacement • complex fabrication
Electrothermal actuators (vertically moving with mechanical latching mechanisms)	<ul style="list-style-type: none"> • low actuation voltage • low restoring force 	<ul style="list-style-type: none"> • large vertical and lateral but uncontrollable displacement • low contact force

2.3.2 Contact distance versus isolation

- DC isolation

The DC voltage isolation of a switch is given by the maximum voltage which can be applied in the OFF-state between the input and the output end without having a breakdown between the separated contacts. By experience, such a breakdown occurs when a field strength is reached in the isolation gas (for dry air, atmospheric pressure, room-temperature, about $30\text{V}\cdot\mu\text{m}^{-1}$). Therefore, the isolation or so-called stand-off voltage basically depends on the atmosphere inside the switch package and on the contact distance.

For dimensions of the order of a few tens of micrometer the breakdown mechanisms are different. In large scale systems, electrical breakdown arises due to electrons accelerated in the electric field colliding successively with molecules which are ionized and thus result in more electrons which are subsequently accelerated by the field and cause further collisions. For dimensions of the same order as the mean free electron path to collision or for very low pressures with decreased probability of collision, ionizing breakdown cannot occur. For very small pressure-distance products, the breakdown voltage theoretically even increases after having passed a theoretical minimum. In dry air, the minimum voltage at which a breakdown is possible is 327V, corresponding to a field strength of $66\text{V}\cdot\mu\text{m}^{-1}$ at atmospheric pressure [54].

This minimum was confirmed by measurements reporting on a breakdown voltage of $64\text{V}\cdot\mu\text{m}^{-1}$. This can be explained by extremely high local field

strengths due to surface roughness which plays an increasing role for very low gap distances [55]. Thus, the breakdown occurs by field emission depending on the surface properties. Irregular and unstable discharging phenomena can also occur at larger distances if the field strength exceeds $28\text{V}\cdot\mu\text{m}^{-1}$, without leading to a breakdown [54]. Discharging does not destroy the electrodes but, in the long term, a stable glow discharge degrades the electrodes and should be avoided in normal operation modes.

From a practical point of view, a MEMS in-line switch with deposited metal contacts provides reliable isolation for 300V at gap distances of 10-20 μm and about 150V for contact distances of 2-4 μm .

- RF isolation

RF isolation of an electrical switch is defined by the ratio of the output voltage to the input voltage in the OFF-state. Since this ratio can vary over many orders of magnitude, a logarithmic scale is commonly used.

One might assume that the isolation in the microwave band is mainly determined by the coupling capacitance between the overlapping switching contact areas. When comparing the measured isolation with the calculated value from the capacitance between the contacts, it can be seen that the effective coupling capacitance must be much larger. For 'standard' membrane and cantilever switch designs, the measured coupling capacitance by far even exceeds the single contact capacitance. The reason for this discrepancy is that the total coupling capacitance is composed of:

$$C_{off} = \frac{1}{2}(C_A + C_f) + C_p \quad [4]$$

where C_A = parallel-plate capacitance of open contacts

C_f = fringing field capacitance

C_p = parasitic capacitance between the open ends of the transmission line

The fringe capacitance is proportional to the ratio of the contact distance to the overlapping contact length, and can even exceed the parallel-plate capacitance itself. The coupling capacitance between the open ends of the transmission line mainly depends on the gap between the two signal lines and on the signal line width. For a typical switch design on silicon, this coupling capacitance is 2-4fF, and it is about 50% lower for GaAs-substrate based switches [53].

2.3.3 Reliability of metal-to-metal contacts

The metal contacts are the most crucial part of a MEMS switch since they determine the ON-state resistance and the current handling capability, and are the source of the most dominant failure mechanisms in the type of switches under discussion. Besides literature addressing metal contact issues in conventional relays, a variety of publications [51,54,56] reported on the contact physics, contact forces and contact reliability in MEMS switches and relays. The main issues determining contact performance in microswitches are discussed in the following paragraphs.

Contact force, resistance, materials and effective contact area

The contact force of typical MEMS switches is between $10\mu\text{N}$ and 10mN , compared to conventional relays with forces from 100mN upward [56]. The dependence of the contact resistance on the contact pressure has been thoroughly investigated for different contact materials [51,54,56]. According to the literature, a stable contact resistance of $80\text{-}200\text{m}\Omega$ can be achieved at about $100\mu\text{N}$ for gold, which is the most common contact material, dropping to $10\text{-}20\text{m}\Omega$ at 1mN [57]. For AuNi5, a force of at least $300\mu\text{N}$ is necessary for a stable contact resistance below $100\text{m}\Omega$ [51]. Rhodium, another less common choice, gives a stable contact resistance of about 1Ω at a minimum force of $600\mu\text{N}$ [58]. Other well-suited materials are sputtered or plated rhenium and gold-palladium alloys with a contact resistance of $0.5\text{-}3\Omega$ for $0.2\text{-}2\text{mN}$ contact force [53], or hard-gold AuCuCd with a stable contact resistance of $50\text{-}80\text{m}\Omega$ at a contact force of $200\mu\text{N}$. Platinum was also used for contact material alloys in a MEMS switch design, but it was not commented on the composition and performance. The contact resistance of gold is about ten times lower than that of AuNi alloys, which again is lower than that of rhodium by a factor of ten. Besides the different resistivities, this can be explained by the hardness of the materials, resulting in a larger effective contact area for a low hardness at a given contact force, due to elastic deformation of the metal.

The effective contact area is then one of the main factors influencing the contact resistance. A larger contact area results in a smaller resistance, as expected. Smaller areas are also characterized by non-linear behavior i.e. the resistance increases with increasing current, which can be explained by local annealing effects caused by increased localized heating due to the smaller thermal conductivity of smaller

contact areas. In general, the better heat dissipation of larger effective contact areas is the critical design criterion to maintain low contact resistance, high power handling capability, and a minimum of surface adhesion wear [57].

Materials with a native oxide such as aluminum, copper, nickel or silicon, are not the first choice since they require a substantial contact force for an acceptable contact resistance. Due to its hardness, silicon, even though very suitable since it is already often used as the structural material of the device, results in very high contact resistances of the order of 20k Ω .

In all, gold and gold alloys in hermetic atmosphere (nitride or air at atmospheric pressure) are still the first choice contact materials for microrelays because of their low hardness and low resistivity, both resulting in a low contact resistance; their relatively high melting temperature for a soft material and their resistance to absorption of surface contaminants. However, the final choice of the contact material will still depend on the specific application.

Metal deposition process

The deposition processes of the contact material affects its contact performance. Sputtered gold is much harder than electroplated gold and therefore less susceptible to surface damage. Also, higher gold deposition temperatures (e.g. hot sputtering at 200 $^{\circ}$ C) result in a dense and compact grain size and show less surface change due to material transfer and annealing at higher currents than gold deposited at lower temperatures [57].

Contact contamination

Clean contacts are extremely important for microrelays compared to conventional relays since the very low contact forces are not able to break absorbed contaminant films. Sample preparation with tetrachloroethylene followed by alcohol and de-ionized water was found to be a sufficient cleaning method [57]. Another successful tested procedure is cleaning in isopropanol with 40 subsequent switching cycles at 40mA. In both cases, the samples were afterward kept and tested in a nitrogen atmosphere. Besides residues left over from fabrication steps with organic materials, if the device is not sealed hermetically, surface contamination can also occur by absorption or condensation of gases, either during packaging procedure or during operation. From a material point of view, gold is very suitable since it strongly resists surface layer formation [53].

Adhesion force and microwelding

The estimation of the adhesion force is very important to design the necessary restoring force of the switch actuator. The adhesion force is the least understood parameter of metal contacts in microrelays, and strongly deviating values were reported for different switch designs. Besides the contact material, the switching history influences the remaining adhesion force after releasing the actuation mechanism. The adhesion force depends on the hardness of the contact material.

Heat dissipation in the contacts is a very important parameter since increased contact temperature softens the material, resulting in a larger effective

contact area with larger adhesion. At even higher temperatures caused by local current densities, a soft material with low melting point deforms plastically under the contact pressure, and static microwelding might occur, which can be assumed to be the major failure mechanism at larger switching currents [59].

The probability of failure due to contact adhesion also depends on the switching history, which is not only characterized by the switching conditions and the number of cycles, but also by the dwell time of the closed contacts. It is well known for relays in the macro-world that contacts have an increasing tendency to stick to each other if the closed contact is maintained for a very long time, especially when applying an electrical load. Unfortunately, no reliability data has been published for MEMS switches about this type of aging with closed contacts.

2.3.4 Adhesion between actuation electrodes

Besides contact stiction as the main failure mechanism of metal-to-metal contact switches as discussed in the previous section, unwanted adhesion can also occur between touching electrodes during operation, which is also a very important failure mechanism of MEMS switches. This type of failure might have different causes in electrostatic actuators, listed in the order of their importance for MEMS switches:

- Electrostatic stiction: Caused by charge injection and charge trapping in dielectric layers, mainly dependent on the field strength, if above $2 \text{ MV}\cdot\text{cm}^{-1}$, and on the dwelling time in the active state [60].

- Hydrogen bridging: Hydrophilic surfaces such as the native oxides of all silicon based dielectrics (nitrides and oxides) are highly hydrophilic and contain absorbed water layers. When two of these surfaces are brought into close contact, hydrogen bonds may form and result in quite high adhesion energy [61].
- Capillary condensation between contacting surfaces: Liquid condensate can drastically increase the effective contact area of otherwise rough surfaces and can cause stiction [62].
- Van der Waals forces between solid bodies: Caused by mutual electric interaction of the induced dipoles in two touching bodies, strongly dependent on surface roughness [62].

Possible means of preventing the mentioned effects are listed as follows:

- Hermetic packaging: Will reduce effects of electrostatic stiction and hydrogen bridging drastically, since they depend on the relative humidity of the working environment.
 - Increased surface roughness: Reduces the effect of Van der Waals forces between solid bodies, which is the main concern only for surface roughness below a few nm typical of traditional LPCVD based surface micromachining [62].
 - Anti-stiction coating: Hydrophobic self assembled monolayer (SAM) coatings prevent the formation of hydrated layers and thus reduce the effects of hydrogen bridging and capillary condensation between contacting surfaces. Anti-stiction coating of the total structure is not possible for metal-to-metal contact switches.
-

- Choice of materials: Silicon dioxide has a much lower trap density than silicon nitride and is therefore less susceptible to electrostatic stiction. However, it should be noted that dioxide takes up more moisture than nitride and might be worse overall if the effects of hydrogen bridging and capillary condensation between contacting surfaces are not taken care of by other methods.
- Low electrostatic actuation voltage design: Charge injection is exponential with voltage and a reduction in the actuation voltage will have a large influence in the lifetime of a capacitive MEMS switch, thus reducing the effect of electrostatic stiction.
- Bipolar actuation voltage: The polarity of the voltage does not affect the electrostatic force. Negative voltage pulses, when releasing the actuation voltage, reduced trapped charges and result in a vast improvement in the switch reliability [53]. Charge trapping is avoided by using AC actuation voltage. This reduces the effect of electrostatic stiction, at the cost of increased complexity of the electronic drive circuitry.

2.4 Chapter summary

This chapter presents literature reviews on MEMS technology and its current notion. Firstly, the 3 methods of the MEMS fabrication technology, namely bulk micromachining, surface micromachining and micromoulding, are discussed. The following section gives an overview of RF MEMS followed by the design and development of RF MEMS switches. The typical electrostatic microactuator design for MEMS switches is also presented, followed by the possible applications of MEMS switches. Finally, the various design

considerations for the design of electrostatic metal-to-metal contact MEMS switches are listed and discussed in details.

The motivation of this research project is to design and develop a lateral MEMS microactuator switch for RF switching purpose. The design has a reciprocating actuation mode, and incorporates a unique feature consisting of a dielectric insulation slot that separates the switch contact section and the microactuator structure. The microactuator switch design is developed with the aim of having low switch contact resistance, high switching speed, good reliability and moderate power consumption. This research project will also investigate the structural integrity and insulation capability of the dielectric slot hole which is to be filled with both silicon oxide and silicon nitride.

Chapter 3: Design of the Lateral Microactuator Switch

In this chapter, the actuation mechanism and structural design of the microactuator switch will be documented and presented. Basically, a resonant microstructure depends on the actuating component and a well-tuned stiffness that is controlled by a flexure mechanism, in order to reach a pre-defined resonant frequency. The current research project will focus on the electrostatic actuation mechanism and look into its most widely used device, the electrostatic comb-drive. The electrostatic comb-drive was first developed by W. C Wang [40]. Comb-drives are widely used mainly because their output force is easily controlled by the applied voltage, and the output force needed to drive passive structures is extracted more easily than in rotational actuators [48].

3.1 Basic mechanism of electrostatic actuation

The many advantages of electrostatic actuation includes the suitability for miniaturization, ease of integration on a chip, easily controlled high switching speeds, relatively low power consumption and high efficiency. Electrostatic actuators allow high accuracy, capacitive measurement of displacement, and are capable of high bandwidth operations. Many MEMS devices use electrostatic forces as their main actuation scheme. Silicon microstructures can be actuated and sensed electrostatically by means of fixed electrodes forming parallel-plate capacitors with the structure. The two types of electrostatic actuation mechanism and their development with various comb-drive structures will be discussed as follows.

3.1.1 Parallel-plate capacitors

The theory behind a parallel-plate capacitor will be presented in this section. The same theory is then extended to the working mechanism of an electrostatic comb-drive and other related applications. Figure 11 shows a simple schematic of a parallel-plate capacitor. An electrode is used to actuate a moving structure. In most applications two electrodes will be separated by an air gap, with one electrode fixed and the other being free-moving [44].

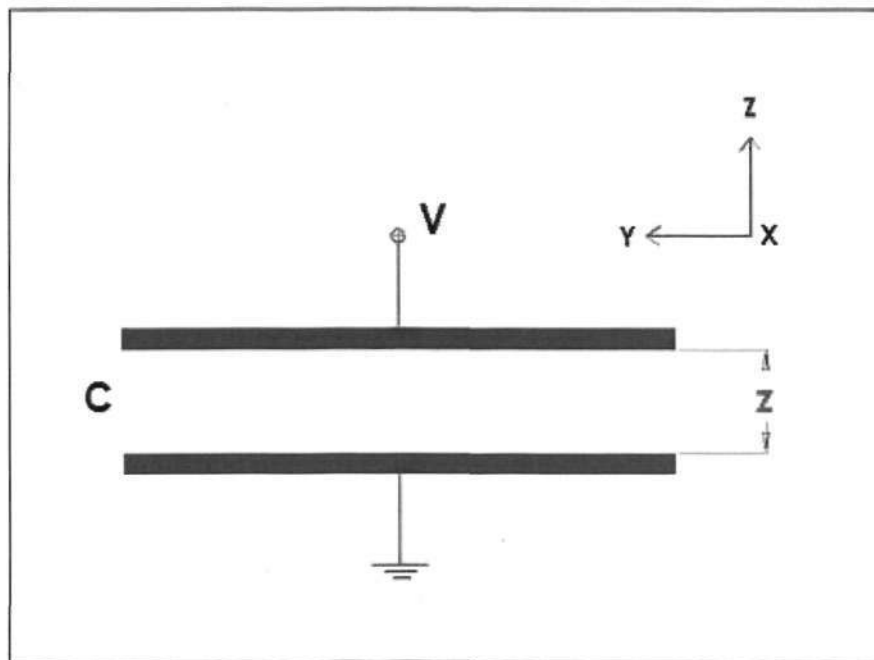


Figure 11: Schematic of a parallel-plate capacitor

The capacitance (C) is given by:

$$C = \frac{\epsilon_0 A_0}{z} \quad [5]$$

where ϵ_0 = vacuum permittivity ($\epsilon_0 = 8.854 \times 10^{-12}$ F/m)

A_0 = plate area

z = electrode separation distance

Chapter 3: Design of the Lateral Microactuator Switch

When a constant voltage V is applied across the electrodes, the movable structure is pulled towards the fixed structure, thus increasing the capacitance between the electrodes and also the stored energy W . The work done (dW) in moving the structure by an incremental distance (dZ) is:

$$dW = \frac{1}{2} dCV^2 \quad [6]$$

where dC = change in capacitance

Since $dW = Fdz$, the force (F) attracting the free electrode to the fixed electrode is given as follows:

$$F = \frac{dW}{dz}$$

$$\Rightarrow F = \frac{1}{2} \frac{dC}{dz} V^2 \quad [7]$$

From equation [5], we obtain the following:

$$\frac{dC}{dz} = -\frac{\epsilon A}{z^2} \quad [8]$$

Substitute [8] into [7] gives:

$$F = \frac{1}{2} \left(-\frac{\epsilon_o A_o}{z^2}\right) V^2$$

$$\Rightarrow F = -\frac{1}{2} \frac{\epsilon_o A_o V^2}{z^2} \quad [9]$$

From equation [9], it can be seen that the force (F) is directly proportional to the square of the excitation voltage (V) and inversely proportional to the square of the separation distance (z). Due to the square factor dependence, reducing the air gap is very advantageous. Typical values for the air gap are in the region of 2-5 μ m. Also, it

Chapter 3: Design of the Lateral Microactuator Switch

is observed that the relationship between the electrostatic force and the displacement is non-linear. This implies that the parallel-plate capacitor with displacement in the normal direction (with respect to the plate surface) may not be an ideal choice for actuation applications. This is the main drawback of such structures unless the movement concerned is small as compared to the electrostatic gap. The negative sign obtained in equation [9] implies that the force between the electrodes is attractive in nature.

The need for a linear actuating/sensing device has led to the design and development of the electrostatic comb-drive, which consists of interdigitated cantilever beams called comb fingers. Electrostatic comb-drives will be discussed in the following section.

3.1.2 Types of electrostatic comb-drive

Interdigitated comb-drives have been widely employed in various microactuator designs, providing a lateral electrostatic force that is independent of lateral position. Figure 12 shows a schematic of an electrostatic comb-drive structure. The comb-drive structure consists of comb-like structures with fingers overlapping each other. One comb is free-moving while the other comb is in a fixed position. The movable and fixed comb fingers are also known as the rotor and stator respectively.

The working concept of a comb-drive is similar to that of the parallel-plate capacitor. The concept as discussed for the parallel-plate capacitor in the earlier section can be applied to the lateral, transverse, vertical and rotary types of comb-drive.

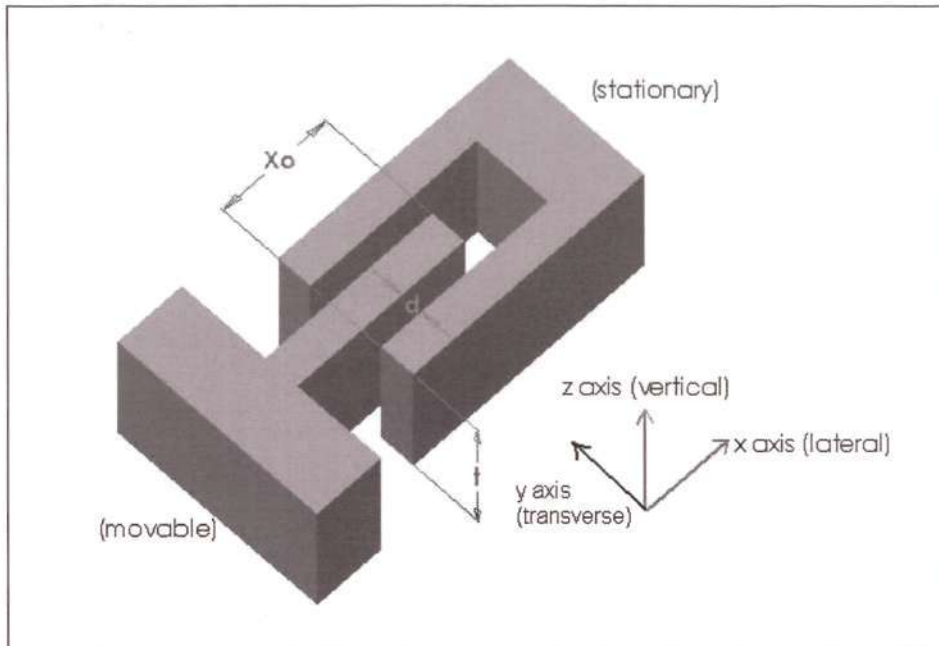


Figure 12: Schematic of an electrostatic comb-drive structure

3.1.2.1 Lateral motion comb-drive

Figure 13 shows a schematic of the cross-section of an electrostatic comb-drive [44].

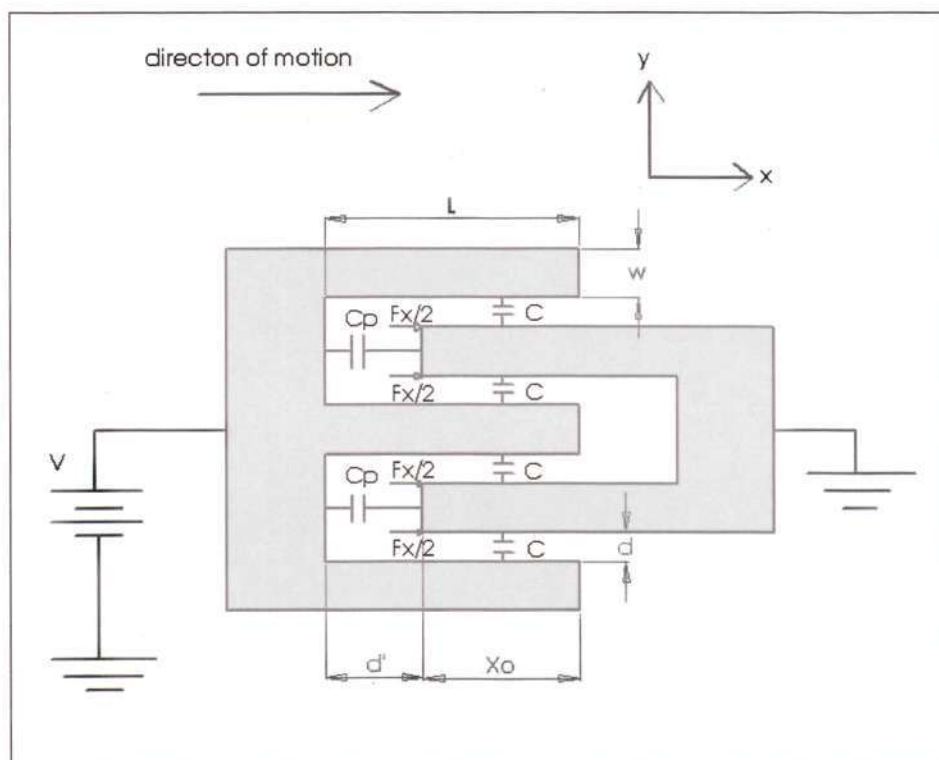


Figure 13: Schematic of the cross-section of an electrostatic comb-drive

Chapter 3: Design of the Lateral Microactuator Switch

With reference to Figure 13, the initial overlapped finger length is x_0 , the air gap between fingers is d , the finger width is w and the depth (or thickness in the z direction) of the comb finger is t . Two types of capacitance will arise when a potential difference (V) is applied between the movable and fixed comb fingers, namely capacitance C and parasitic capacitance C_p . The parasitic capacitance C_p arises due to the undesirable fringing electrostatic fields.

Capacitance can be expressed as:

$$C = \frac{Q}{V}$$

$$\Rightarrow C = \frac{\epsilon_0 A}{d}$$

where Q = stored charge

V = electrostatic potential between electrodes

d = gap between electrodes

The comb-drive moving fingers translate along the longitudinal x -axis of the fingers. Consider an incremental movement (x) in the x -direction for an individual set of movable comb tooth.

Capacitance (C) is given as:

$$C = 2 \left[\frac{\epsilon t (x_0 + x)}{d} \right] \quad [10]$$

where $A = t(x_0 + x)$ {Note: a change in area}

d = transverse gap between fingers

Chapter 3: Design of the Lateral Microactuator Switch

Parasitic capacitance (C_p) is given as:

$$C_p = 2 \left[\frac{\epsilon t w}{(d' - x)} \right] \quad [11]$$

where $A = tw$ {Note: a change in gap distance}

d' = lateral gap between fingers' tip and base

For 1 set of comb fingers, total capacitance is expressed as:

$$\begin{aligned} C_{\text{total}} &= C + C_p \\ &= 2 \left[\frac{\epsilon t (x_o + x)}{d} + \frac{\epsilon t w}{(d' - x)} \right] \end{aligned}$$

For N set of comb fingers, total capacitance is:

$$C_{\text{total}} = 2N \left[\frac{\epsilon t (x_o + x)}{d} + \frac{\epsilon t w}{(d' - x)} \right] \quad [12]$$

The parasitic capacitance (C_p) can be avoided when the tip of the overlapping finger is kept at a distance of $(x_o + x)$ away such that C_p is not dominant. Neglecting fringing electrostatic field effects (i.e. $C_p = 0$), we have:

$$C_{\text{total}} = 2N \left[\frac{\epsilon t (x_o + x)}{d} \right] \quad [13]$$

From equation [13], $\frac{\partial C_{\text{total}}}{\partial x_o} = 2N \frac{\epsilon t}{d}$. Since $F = \frac{1}{2} V^2 \frac{\partial C_{\text{total}}}{\partial x_o}$, therefore the resultant

lateral electrostatic force (F_x) acting on each individual movable comb tooth for a total of N sets of comb fingers is expressed as:

$$F_x = \frac{1}{2} V^2 \frac{\partial C_{\text{total}}}{\partial x_o}$$

$$\begin{aligned}
 &= \frac{1}{2} V^2 \left(2N \frac{\epsilon t}{d} \right) \\
 \Rightarrow F_x &= \frac{N \epsilon t}{d} V^2 \quad [14]
 \end{aligned}$$

Equation [14] can be used to calculate the total actuation force of lateral driven comb-drives. However, the interdigitated field force generated by comb-drives is generally smaller than the direct force across parallel-plate capacitors, but it exhibits a better controllable range of motion. As long as the movable fingers are precisely centered in their corresponding air gaps, the lateral force components that act on each finger (in the y direction) will exactly cancel each other out. To increase the force and obtain the maximum displacement with this comb-drive mechanism, a cantilever with a large number of comb teeth should be designed.

The relationship between the force and displacement shows that the applied force is independent of the displacement. This would imply that this actuation mode has a linearity to be a good actuator. According to literature research [63], the force displacement profile for lateral motion of the comb-drive is as shown in Figure 14.

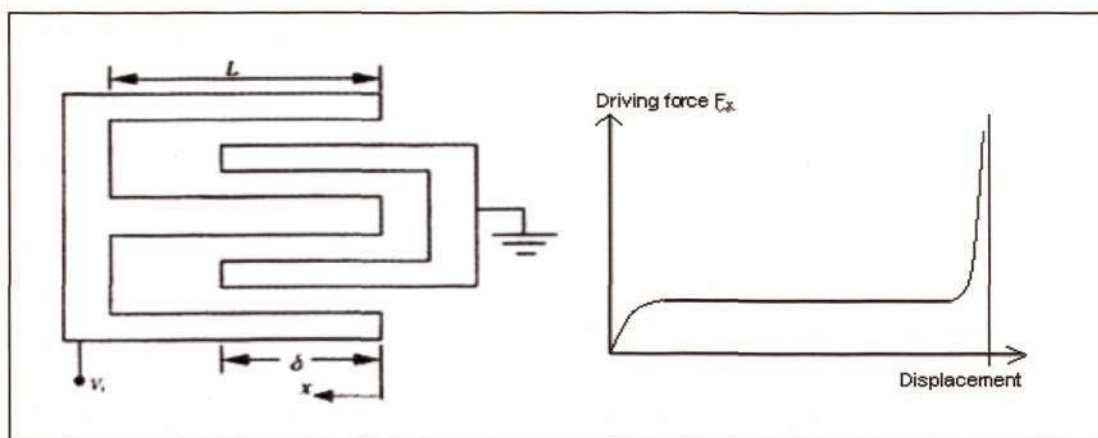


Figure 14: Force-displacement profile for lateral motion
of an electrostatic comb-drive [63]

Chapter 3: Design of the Lateral Microactuator Switch

With reference to the force-displacement profile as shown in Figure 14, there is non-linearity occurring at regions where displacement is near zero and near maximum. The non-linearity observed at the near-zero displacement region is generally caused by fringing electrostatic field effects, whereas the non-linearity at the near-maximum displacement region is caused by the dominant parasitic capacitance (C_p). In general, the driving force will be approximately constant in the range of $0.2L < (x + \Delta x) < 0.7L$. Within this region, the driving force will be constant and is independent of the lateral displacement [63].

The lateral electrostatic force is independent of the position of the moving comb fingers, and the force increases with decreasing gap spacing (d) and additional number of comb fingers (N). On the whole, the linearity of capacitance, sensitivity and force make lateral actuation motion a good choice for both sensing and actuation purposes.

3.1.2.2 Vertical motion comb-drive

The vertical motion comb-drive has a phenomenon known as comb finger levitation. The effect of comb finger levitation is mainly caused by the electrostatic repulsion effects due to the image charges mirrored in the ground plane. Figure 15 shows the cross section view of a levitated comb-drive [43]. With reference to Figure 15, positively-biased comb-drive fingers will induce negative charges both on the ground plane and on the movable comb finger. However, this ground plane contributes to an unbalanced electrostatic field distribution. The imbalance in the field distribution results in a net vertical force induced on the movable comb fingers, which levitates the movable structure away from the substrate. The compliance of the suspension and the

Chapter 3: Design of the Lateral Microactuator Switch

quality factor for vertical displacements will determine if the levitation force will cause significant static displacement or excites a vibration mode of the structure.

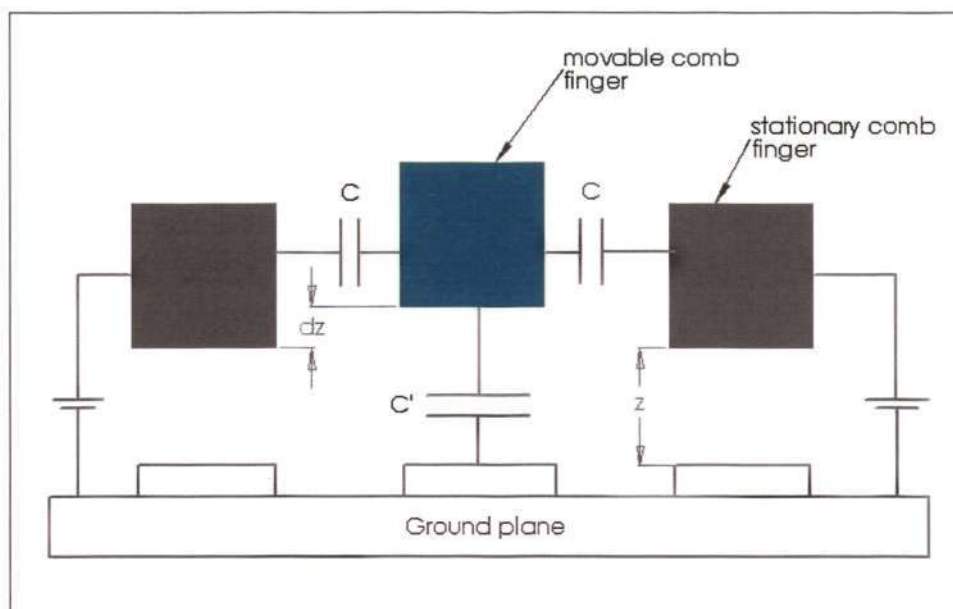


Figure 15: Cross section view of a levitated comb-drive [43]

There are typically two methods to reduce the effect of levitation. One method is to reverse the polarity of the stator parts of the comb fingers thus resulting in an altered field distribution. The other method is to modify the ground plane so that there is a strip of conductor biased at the same potential underneath each comb finger.

3.1.2.3 Transverse motion comb-drive

As opposed to lateral motion, the comb finger may move in the transverse (orthogonal to lateral motion) direction. Figure 16 shows the cross section view of a transverse motion comb-drive. The transverse motion of the comb fingers can be considered as one of the undesired motion for a linear comb-drive, due to the fact that there is a tendency for the opposite finger to 'stick' together. The working principle of transverse comb is similar to that of the parallel-plate capacitor.

Chapter 3: Design of the Lateral Microactuator Switch

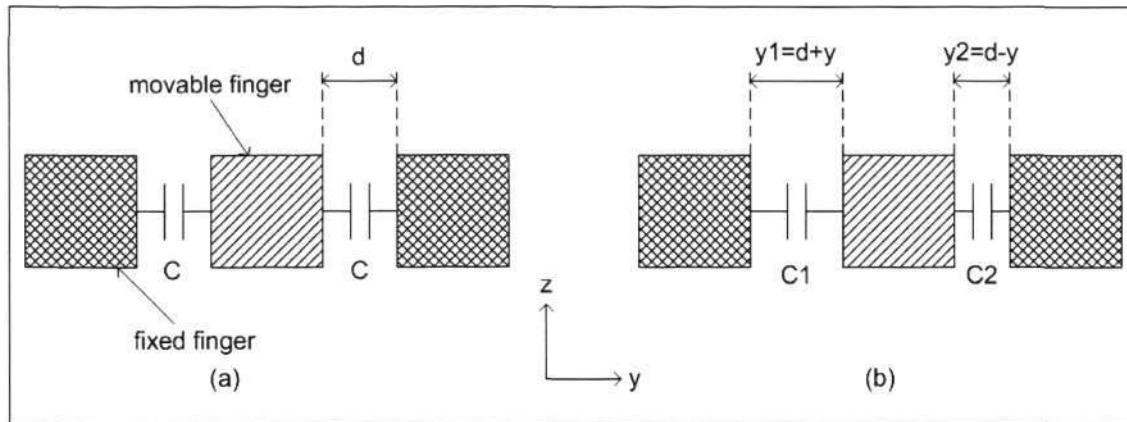


Figure 16: Cross section view of a transverse motion comb-drive

In Figure 16(a) above, the movable comb finger at the center is positioned at the exact center between both fixed comb fingers. In this manner, the capacitances at both sides are equal and are expressed as $C = \frac{\epsilon x t}{d}$. In Figure 16(b), under the influence of a weak flexure with low stiffness ratio, a shift in position of the movable finger will take place as a result. This may lead to a variation in the capacitances between both sides of the movable finger.

The resultant capacitance variations are given as:

$$C_1 = \frac{\epsilon x t}{d + y} \quad [15]$$

$$C_2 = \frac{\epsilon x t}{d - y} \quad [16]$$

The differential electrostatic force induced by the fingers in the transverse direction is expressed as:

$$F_y = F_{y2} - F_{y1}$$

$$\Rightarrow F_y = \frac{1}{2} \frac{\partial C_2}{\partial y} V^2 - \frac{1}{2} \frac{\partial C_1}{\partial y} V^2 \quad [17]$$

From equation [17], the transverse electrostatic force can then be obtained and simplified as:

$$F_y = \frac{1}{2} \epsilon_0 t \left[\frac{1}{(d-y)^2} - \frac{1}{(d+y)^2} \right] V^2 \quad [18]$$

From equation [18], it can be seen that the relationship between the transverse force and displacement is a non-linear one. This non-linear relationship between the transverse force and displacement causes side-instability of the comb-drive. It is obvious that the non-linearity between the force and displacement is undesirable for actuation, and should be avoided by controlling or limiting the driving voltage and maximum lateral deflection to certain values.

3.1.2.4 Rotary motion comb-drive

The rotary comb-drive has been developed as an extension from the linear comb-drive. Two types of rotary comb-drives are investigated here. The first type of rotary comb-drive to be discussed is known as the angular comb-drive [64]. Figure 17 shows a schematic of a quadrant of a rotary motion comb-drive. The rotary comb-drive microactuator consists of N pairs of capacitive plates. One-half of the total number of plates is used for clockwise rotation, while the other half is being used for counter-clockwise rotation purpose.

Chapter 3: Design of the Lateral Microactuator Switch

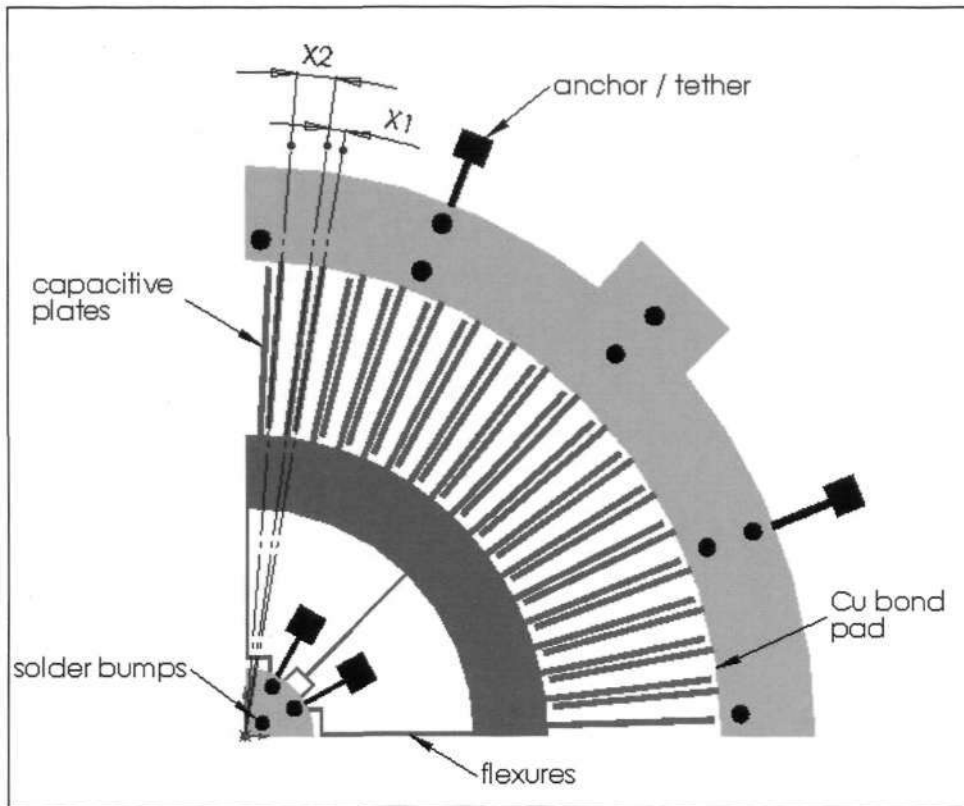


Figure 17: Schematic of a quadrant of a rotary motion comb-drive [64]

For a small rotation angle (θ), the plates can be assumed as parallel-plate capacitors with decreasing gap x_1 and increasing gap x_2 where:

$$x_1 = x_n - r\theta \quad [19]$$

$$x_2 = x_n + r\theta \quad [20]$$

where r = distance between rotor center and plate center

x_n = nominal plate gap

θ = small rotation angle subtended

By applying a voltage V_1 to one-half of the rotary comb-drive structure, the resultant electrostatic torque is:

$$T(V_1, \theta) = \frac{N}{4} r \epsilon_0 A \left(\frac{V_1}{x_1} \right)^2$$

Chapter 3: Design of the Lateral Microactuator Switch

$$\Rightarrow T(V_1, \theta) = \frac{N}{4} r \epsilon_0 A \left(\frac{V_1}{x_n - r\theta} \right)^2 \quad [21]$$

where A = plate area

ϵ_0 = permittivity of air

From equation [21], the output torque (T) is a non-linear function of both the applied voltage (V_1) and the rotation angle (θ). The non-linearity with regard to the applied voltage may be reduced by applying differential voltages V_1 and V_2 to the two halves of the structure on each side of the moveable comb finger where:

$$V_1 = V_b + V_c \quad [22]$$

$$V_2 = V_b - V_c \quad [23]$$

where V_b = fixed bias voltage

V_c = control voltage

For a constant control voltage (V_c), the rotation of the rotary comb-drive microactuator is given as:

$$\theta(V_c) = \frac{T(V_1, \theta) - T(V_2, \theta)}{K_\theta} \quad [24]$$

where K_θ = mechanical spring stiffness of the flexure coupling the rotor to the fixed anchor.

Another type of rotary comb-drive to be discussed here is known as the torsional comb-drive. The rotary comb-drive (torsional comb) is designed for torsional resonant plates in which the comb fingers lie on arcs of concentric circles, and can both actuate and sense torsional motion about the center of these circles [64]. Figure 18 shows a schematic of a rotary comb-drive (torsional comb).

Chapter 3: Design of the Lateral Microactuator Switch

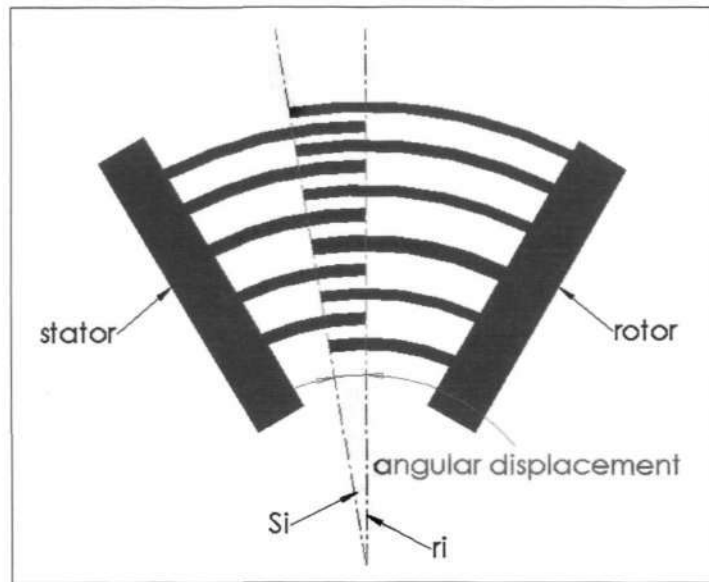


Figure 18: Schematic of a rotary comb-drive (torsional comb)

The capacitance between the two fingers can be expressed as:

$$\begin{aligned}
 C &= \frac{Q}{V} \\
 &= \frac{\epsilon t \theta}{\ln\left(\frac{S_i}{r_i}\right)} \\
 \Rightarrow C &= \frac{\epsilon t \theta}{\ln\left(1 + \frac{d}{r_i}\right)} \quad [25]
 \end{aligned}$$

where Q = charge between two comb fingers

ϵ = dielectric constant

θ = static/initial finger overlap angle

t = thickness of comb finger

S_i = inner radius of stator comb finger

r_i = outer radius of rotor comb finger

d = gap between the stator and rotor comb finger ($d = S_i - r_i$)

Chapter 3: Design of the Lateral Microactuator Switch

The circumferential electrostatic force is:

$$F_x = \frac{1}{2} \frac{\partial C}{\partial x} V^2$$

$$\Rightarrow F_x = - \frac{\epsilon V^2}{2r \ln(1 + \frac{d}{r_i})} \quad [26]$$

where x = circumferential displacement of the rotor comb finger ($x = r\theta$)

V = applied voltage

Assuming that the value of $\frac{d}{r}$ is small, the following equation holds:

$$\ln(1 + \frac{d}{r}) \approx \frac{d}{r} \quad [27]$$

Substitute equation [27] into [26], the simplified equation for the circumferential electrostatic force is:

$$F_x = - \frac{\epsilon V^2}{2d} \quad [28]$$

It can be seen that equation [28] is equivalent to that of the driving force of a linear comb-drive. However, due to some errors involved in the assumption used to obtain the simplified equation [28] for the rotary comb-drive (torsional comb), equation [28] can only be used for rough design calculations. The percentage error difference of the force values obtained between equations [26] and [28] is approximately 2%. This estimated error is dependent on the total number of comb fingers, and will become increasingly significant as the number of comb fingers increases.

3.2 Design of the lateral MEMS microactuator switch

There are many design issues that need to be taken into account for the design of the lateral microactuator switch. For example, the issue on the type of micromechanical flexure design to support and suspend the entire microactuator structure is important as it will determine the resultant resonant frequency of the entire microactuator switch assembly. This will involve optimization of the total stiffness of the flexure supporting the structure and the overall translating structure mass. Other factors include the sizing of comb-drive fingers, determination of the total number of comb fingers, switch contact force and actuation voltage etc.

3.2.1 Specifications

The main design specifications for the lateral MEMS microactuator switch are listed in Table 3 as shown:

Table 3: General specifications of the lateral microactuator switch

Parameter	Specification
Actuation voltage (V)	< 80
Contact resistance (Ω)	< 2
Switching time (μ s)	< 500
Switching lifetime (continuous number of switching cycles)	> 2×10^6

3.2.2 Design features

The main design features for the proposed lateral MEMS microactuator switch are listed and discussed in this section:

3.2.2.1 Layout and mode of actuation

The mode of actuation chosen for the proposed microactuator design is electrostatic actuation using the linear electrostatic comb-drive. The electrostatic comb-drive will act as the driving component providing linear translation motion necessary for the functioning of the microactuator switch. Figure 19 shows a portion of the proposed lateral microactuator switch design with the layout of both the movable and fixed electrodes.

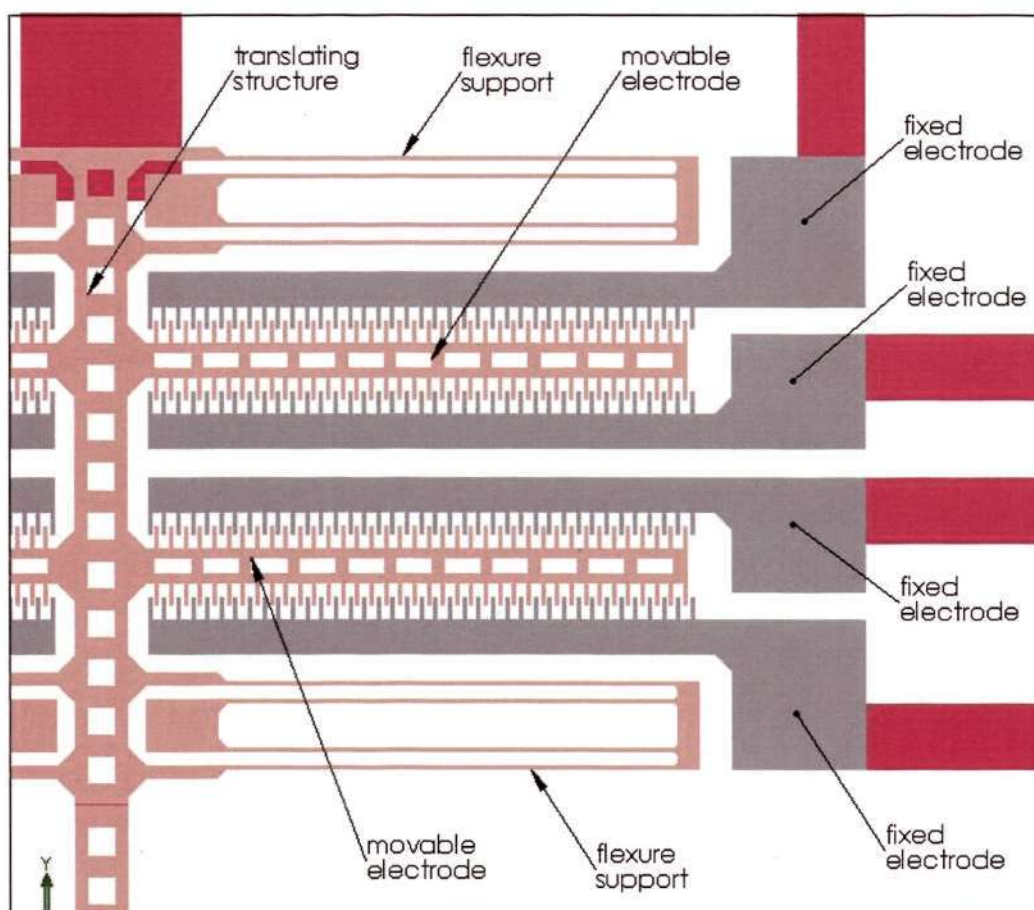


Figure 19: Layout of electrodes of the proposed microactuator switch design

The microactuator employs a 'push-pull' configuration, with an array of comb-drive fingers (one set fixed and the other movable) symmetrically positioned along the center line of the system. The comb teeth of the movable electrodes are shaped in a

Chapter 3: Design of the Lateral Microactuator Switch

double-sided manner and are symmetrically designed for each pair of comb-drives. Thus, many parallel-plate capacitors are formed in the interdigitated field of the two parts of the electrodes. Figures 20 and 21 show the microactuator switch at the 'OPENED' and 'CLOSED' states respectively.

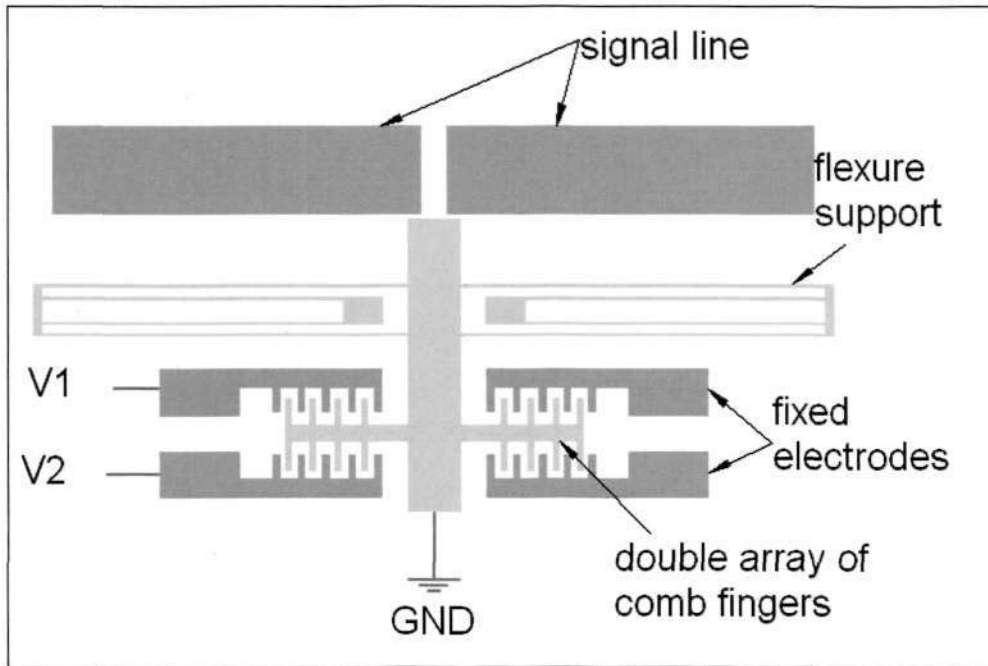


Figure 20: Microactuator switch at 'OPENED' state

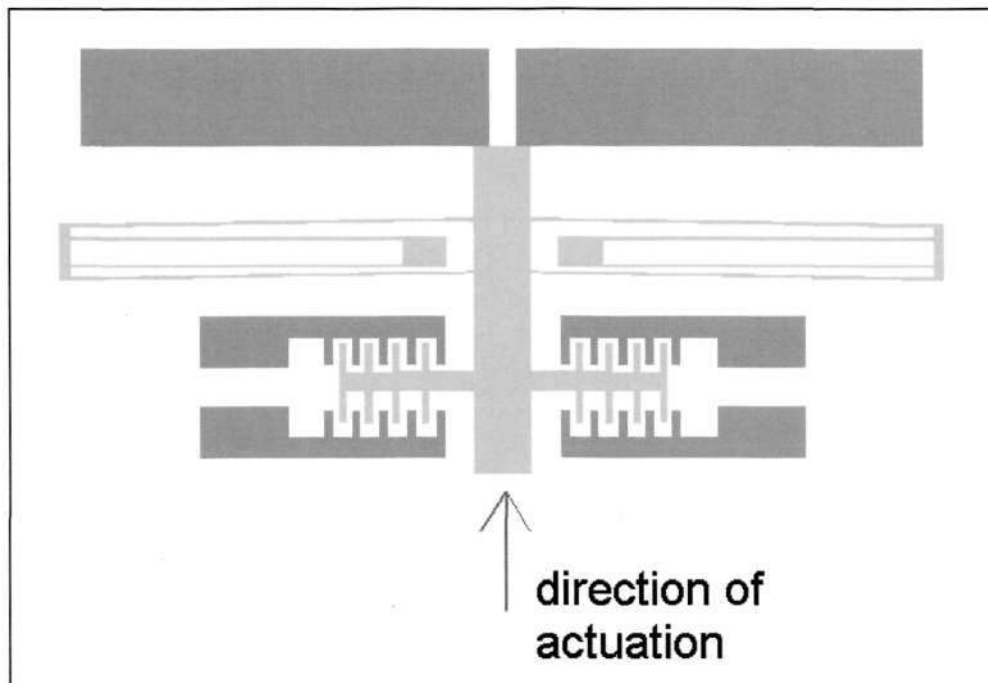


Figure 21: Microactuator switch at 'CLOSED' state

Chapter 3: Design of the Lateral Microactuator Switch

V_1 is the actuation voltage to close the switch and V_2 is the actuation voltage to assist in the return stroke (i.e. opening the switch) in addition to the restoring force of the loaded flexure supports. The center translating beam structure is always grounded. When voltage V_1 is applied only, electrostatic attractive force will be generated between the comb fingers and this will cause a linear motion of the translating structure in the operating direction, causing the folded flexure supports to flex and be loaded. This linear motion physically closes the switch. To open the switch, V_1 is removed and V_2 is applied only. The electrostatic attractive force between the opposite array of comb fingers will assist the physical opening of the switch by ‘pulling’ the translating structure back to its original position, in addition to the restoring force by the flexure supports. The switch-closing voltage V_1 and switch-opening voltage V_2 must have different polarity. Note that V_2 is not necessarily equal to V_1 in magnitude. The value of V_2 is optimized in consideration of the restoring force from the loaded spring flexure supports to sufficiently aid in the return stroke.

The proposed design incorporating a ‘push-pull’ concept caters for an extra force for the return stroke. This helps to optimize the support flexure design since a stiffer flexure design is not required in this case, hence effectively reducing the required actuation voltage, and minimizing the ‘sticking’ tendency at the switch contact region.

3.2.2.2 Structure of microactuator

The microactuator is a three-dimensional (3-D) structure, with the designed linear comb-drives moving in a plane parallel to the mounting plane or substrate. The 3-D structure provides a broad space to maximize the thickness of the structure, a factor

Chapter 3: Design of the Lateral Microactuator Switch

which makes the microactuator being able to generate a higher electrostatic force between the drives when applying a relatively low voltage.

The thickness of the microactuator is designed to be approximately $200\mu\text{m}$. Thus it cannot be fabricated using surface micromachining technology. The use of SOI (silicon-on-insulator) wafers is also not possible since SOI wafers are usually only about $10\text{-}40\mu\text{m}$ in thickness. For the designed width of the comb tooth ($5\mu\text{m}$) and the finger gap ($3\mu\text{m}$), the structure has a high aspect ratio (depth-to-width ratio) which can reach more than 20:1.

The 3-D structural configuration of the proposed microactuator makes it feasible to be fabricated via bulk micromachining technology with DRIE of bulk silicon; and silicon-glass wafer bonding technology is adopted to combine the microactuator with a glass substrate that provides the electrical interface and routing of electrical leads.

3.2.2.3 Micromechanical flexure design

A few types of micromechanical flexure designs will be evaluated and one design will be chosen to support and suspend the entire translating structure mass. The stiffness of the micromechanical flexure should be carefully designed and optimized since there is always a compromise between the flexure stiffness and actuation voltage. Some types of micromechanical flexure designs to be considered are straight-plate flexure, fixed-fixed beam [46], crab-leg flexure [27, 46, 65] and folded flexure [46, 66]. The main function of the micromechanical flexure is to support/suspend the translating structure, and provide proper guidance for the actuation motion.

3.2.2.4 Resonant frequency of system

The resonant frequency of the system is dependent on the stiffness of the micromechanical flexure supports. The appropriate flexure type and design should be carefully chosen and done to cater for high frequency requirements. In most cases it is desirable to have a structure which is very compliant in one direction while being very stiff in orthogonal directions. This can be expressed in the form of a stiffness ratio.

The resonant frequency (f_n) can be obtained by [48]:

$$f_n = \frac{1}{2\pi} \sqrt{\frac{k_x}{m}} \quad [29]$$

where k_x = stiffness value of flexure in the x-direction

m = mass of the translating/moving structure

3.2.2.5 Actuation force, contact force and restoring force

The output actuation force via the electrostatic linear comb-drives must be sufficient to overcome the flexure stiffness in the operation direction, drive the entire translating mass and induce sufficient contact force when switch contact has been made. The stiffness of the flexure design is crucial in determining the required output actuation force. A sufficient contact force is needed for most metal-to-metal contact switches in order to result in low contact resistance.

The restoring force, in this case, is provided by both the micromechanical spring flexure and the opposing electrostatic force generated via the comb-drives when the driving voltage is alternated to the other set of fixed electrodes (the movable electrodes are grounded).

3.2.2.6 Structural toughness and reliability

Due to the 3-D structural design characteristics, the microactuator will have good toughness to support its movement. A sufficient mounting area catered for the suspended movable structure and a thick comb structural design will both result in good reliability for the movement of the electrostatic microactuator.

3.2.3 Micromechanical flexure designs

The micromechanical flexure is one of the most important component of the entire microactuator system, as well as the driving component. The main function of the micromechanical flexure is to provide support and proper guidance for the actuation motion. A flexure that is compliant in the desired direction of displacement and stiff in other orthogonal directions is desired and required (i.e. a large stiffness ratio). The flexure design will determine the stiffness and natural frequency of the system. It is desirable to have a large operating frequency in the operating direction. A few types of micromechanical flexure designs will be discussed. It should be noted that all the analysis to be presented for the types of flexure assumes that there is no residual stress present in the spring structure.

3.2.3.1 Straight-plate flexure

The straight-plate flexure is the simplest flexure that is used in micromechanical structures. They are linear, small-displacement flexures and will constrain motion to a linear direction. Figure 22 shows a straight-plate flexure with one end clamped or fixed.

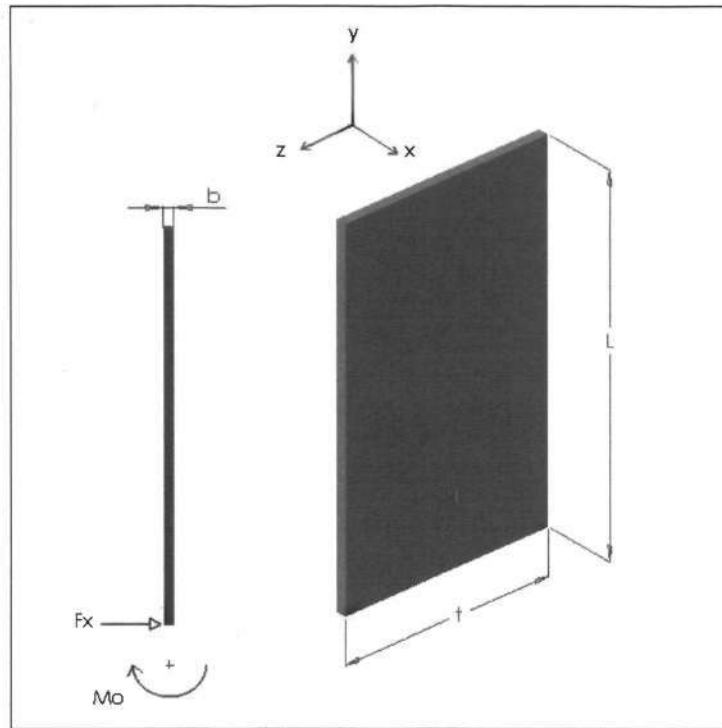


Figure 22: Straight-plate flexure

As in 3-D microactuators, the flexures are actually thin plates because of the large width (t) and small thickness (b). The plates are fixed at one end and subjected to an orthogonal electrostatic force (F_x) and a bending moment (M_o) at the other end. The electrostatic force and bending moment are uniformly distributed on the end plate. With no other loads, the setup can be simplified and assumed to be straight beams. Since such plates have similar deflection state and stiffness ratio as that of general straight beams, the study of the straight plates, in this case, can be obtained via the theory of straight beams.

A concentrated electrostatic force with a bending moment from the movable electrode is applied to one free end of the beam, with the other end fixed. Axial displacement (y direction) can be obtained directly from Hooke's law, while the lateral displacement (x direction) is obtained from small deflection theory [67].

Chapter 3: Design of the Lateral Microactuator Switch

In the x-axis direction, the deflection (Δ) at the end of the loaded straight beam is given by:

$$\Delta = \frac{PL^3}{3EI} \quad [30]$$

where P = applied load

L = length of beam

E = Young's modulus of beam material

I = bending moment of inertia (I_{ZZ})

Now, rearranging equation [30] gives:

$$P = \left(\frac{3EI}{L^3}\right)\Delta$$

By comparing with $P = K\Delta$, the following is obtained:

$$\begin{aligned} K_x &= \frac{3EI}{L^3} \\ &= \frac{3E\left(\frac{tb^3}{12}\right)}{L^3} \\ \Rightarrow K_x &= \frac{Etb^3}{4L^3} \end{aligned} \quad [31]$$

In the axial direction (y-axis), by Hooke's law, axial displacement is given by:

$$\begin{aligned} K_y &= \frac{EA}{L} \\ &\text{where } A = \text{area of the cross section of beam} \\ \Rightarrow K_y &= \frac{Etb}{L} \end{aligned} \quad [32]$$

The stiffness ratio is expressed as:

$$\frac{K_y}{K_x} = \frac{4L^2}{b^2} \quad [33]$$

In general, the stiffness ratio of the straight beam can be very high. Due to the high stiffness, the straight beam/plate generates relatively small displacements under the limited electrostatic forces. The deflections obtained from the equations for the beam flexure will be slightly larger than that obtained for the plate flexure.

For cantilever beams, extensional axial forces develop in the straight beam/plate will result in a non-linear force-displacement relationship. In this case, since the displacement of the straight flexure is very small, thus the non-linear effects that strongly increase the beam stiffness with increasing deflection may be negligible and acceptable.

3.2.3.2 Fixed-fixed beam flexure

A fixed-fixed beam with a rectangular cross section is shown in Figure 23 [46].

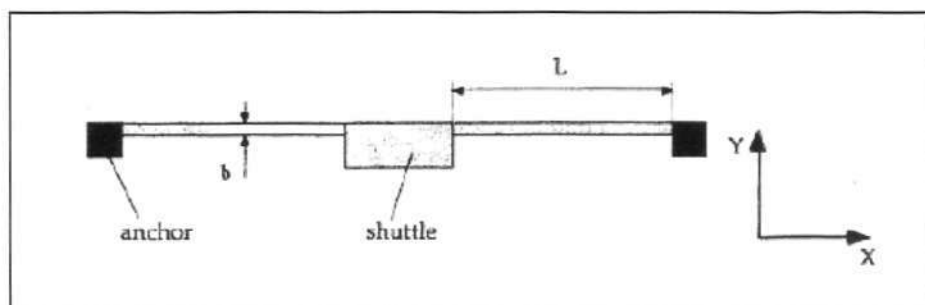


Figure 23: Fixed-fixed beam flexure [46]

Chapter 3: Design of the Lateral Microactuator Switch

A concentrated force is applied (in the y direction) to the center of the shuttle. The axial displacement along the x axis can be found directly from Hooke's law and the lateral deflection along the y axis can be obtained via small deflection theory.

The spring constants for a concentrated force in the x and y directions are expressed as:

$$K_x = \frac{2Ebh}{L} \quad [34]$$

$$K_y = \frac{2Eb^3h}{L^3} \quad [35]$$

where h = thickness (depth) of beam

The stiffness ratio is given by:

$$\frac{K_x}{K_y} = \left(\frac{L}{b}\right)^2 \quad [36]$$

The stiffness ratio for the fixed-fixed beam flexure can be very high. For large displacements, however, extensional forces will develop in the beam and this result in a non-linear force-displacement relation. In this case non-linear effects have to be included which strongly increase the stiffness of the beam with increasing deflection. This spring flexure design is therefore not suitable for large deflections. However, it is useful in applications that require the measurement of axial forces, for instance, to determine residual stresses or externally measure applied axial stresses as in sensing applications.

3.2.3.3 Crab-leg flexure

A crab-leg flexure can be employed to reduce the extensional axial forces. Figure 24 shows a crab-leg flexure [46].

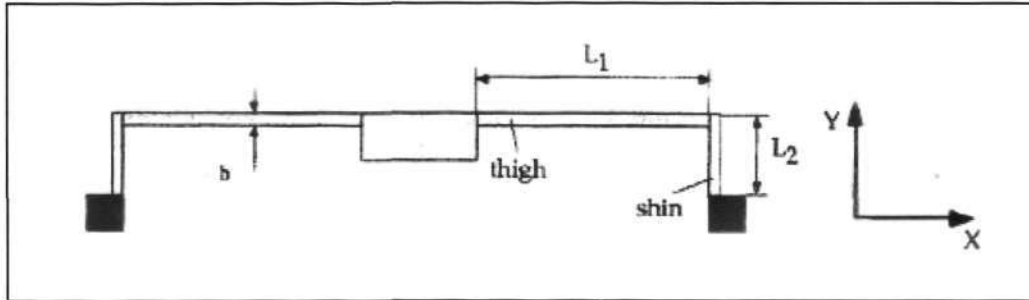


Figure 24: Crab-leg flexure [46]

With reference to Figure 24, the thigh segment has a second moment of inertia I_1 and is of length L_1 ; while the shin segment has a second moment of inertia I_2 and is of length L_2 . The spring constants, as a result of a concentrated force on the shuttle, in the x and y direction, are given by:

$$K_x = \frac{12EI_2}{L_2^3} \left(\frac{L_1I_2 + 2L_2I_1}{2L_1I_2 + L_2I_1} \right) \quad [37]$$

$$K_y = \frac{24EI_1}{L_1^3} \left(\frac{L_1I_2 + L_2I_1}{L_1I_2 + 4L_2I_1} \right) \quad [38]$$

With the thigh and the shin segment having the same width and thickness, the stiffness ratio can be obtained as:

$$\frac{K_x}{K_y} = \frac{1}{2} \frac{L_1^3}{L_2^3} \left(\frac{L_1^2 + 6L_1L_2 + 8L_2^2}{2L_1^2 + 3L_1L_2 + L_2^2} \right) \quad [39]$$

Chapter 3: Design of the Lateral Microactuator Switch

Although this design increases the linear deflection region to a certain extent, a large reduction of the stiffness ratio is introduced. A flexure design that is less susceptible to a decrease in the stiffness ratio is the folded flexure design.

3.2.3.4 Folded flexure

Figure 25 shows a schematic of a folded flexure design [46].

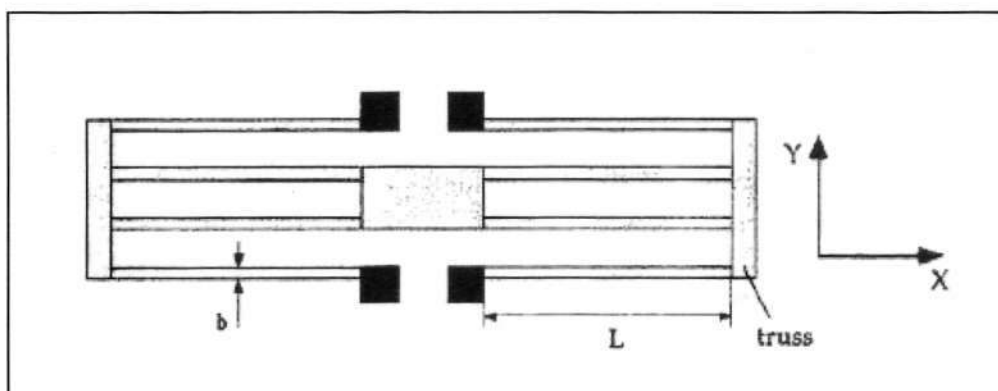


Figure 25: Folded flexure [46]

In the folded flexure design, the beams are anchored near the centre and the trusses allow expansion or contraction of the beams along the x axis. Assuming rigid trusses, the spring constants for the folded flexure design in the axial (x) and lateral (y) directions can be found as:

$$K_x = \frac{2Ebh}{L} \tag{40}$$

$$K_y = \frac{2Eb^3h}{L^3} \tag{41}$$

where h = thickness (depth) of beam

The stiffness ratio is given as:

$$\frac{K_x}{K_y} = \left(\frac{L}{b}\right)^2 \tag{42}$$

Chapter 3: Design of the Lateral Microactuator Switch

The folded flexure design strongly reduces the development of axial forces and exhibits a much larger linear deflection range. The stiffness ratio for small deflections is equal to the stiffness ratio of a fixed-fixed beam. Therefore this flexure design is very suitable for large deflection actuators. The large deflection behaviour of a folded flexure design can be obtained by considering the folded flexure as four folded beams in parallel. Each folded beam is a combination of two clamped-guided beams connected in series. It should be noted that the stiffness of the folded beam flexure in the x axis decreases with increasing displacement in the y axis.

3.2.4 Design calculations for the proposed design

The first step is to size up the comb-drive fingers and determine the total number of comb finger pairs. Precautions must be taken in the design due to a limitation in the aspect ratio for the DRIE etching technique. This will affect the sizing of the comb finger width, the air gap between the comb fingers and the comb-drive thickness. Another issue is to determine the total stiffness of the microactuator system, based on a predefined driving voltage value.

Figure 26 shows a schematic of the proposed comb-drive. With reference to the schematic diagram, at the initial unexcited state, the following parameters are designed and sized as follows:

- Comb finger width : $b = 5\mu\text{m}$
 - Finger gap spacing : $d = 3\mu\text{m}$
 - Initial finger overlap length : $L' = 10\mu\text{m}$
 - Total length of comb finger : $L = 25\mu\text{m}$
 - Gap between finger tip and base : $d' = 15\mu\text{m}$
-

Chapter 3: Design of the Lateral Microactuator Switch

- Comb finger thickness : $t = 60\mu\text{m}$ (assume an aspect ratio of 20:1)

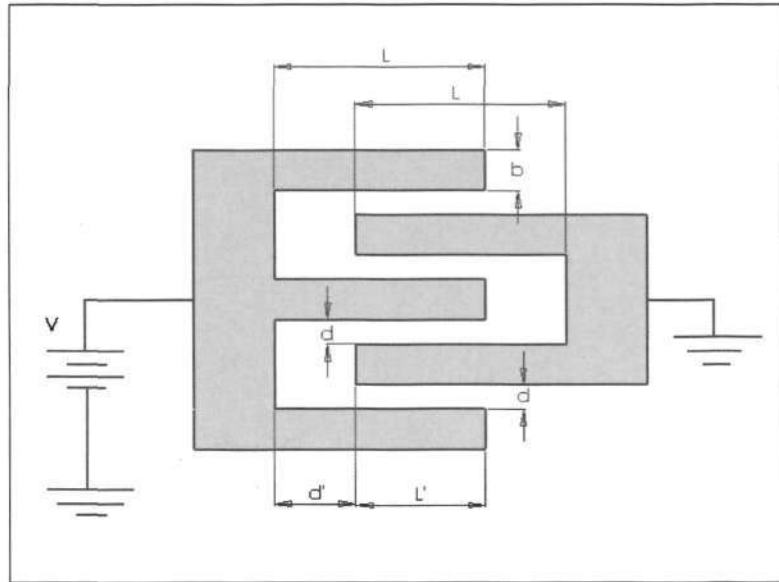


Figure 26: Schematic of proposed comb-drive

The electrostatic actuation force (F_x) in the operating x axis for N pairs of comb-drive fingers is given in equation [14] as:

$$F_x = \frac{N\epsilon t}{d} V^2$$

Now, with reference to Figure 25, the operating direction is along y-axis. Rearranging the equation gives:

$$V^2 = \frac{F_y d}{N\epsilon t}$$

Since $F_y = K_t \Delta$, the driving voltage (V) can be expressed as:

$$V^2 = \frac{K_t \Delta d}{N\epsilon t} \tag{43}$$

where K_t = total stiffness in the operating direction (y axis)

Δ = displacement in the operating direction (y axis)

N = total number of comb-drive fingers

Chapter 3: Design of the Lateral Microactuator Switch

For the micromechanical flexure, the folded flexure design is chosen due to the fact that this type of flexure will strongly reduce the development of axial forces and exhibits a much larger linear deflection range.

With reference to Figure 25 and equations [40] and [41], the stiffness values of the folded flexure are as shown:

$$K_x = \frac{2Eb^3h}{L}$$

$$K_y = \frac{2Eb^3h}{L^3} \quad (\text{y axis is the operating direction})$$

where h = thickness (depth) of beam

The following assumptions have been iterated and finally presented as shown:

- Driving voltage: $V = 56\text{V}$
- Switch closing gap: $\Delta = 3\mu\text{m}$
- Total number of comb-drive fingers: $N = 38 \times 4 = 152$

Using equation [43], we have:

$$V^2 = \frac{K_t \Delta d}{N \epsilon t}$$

$$56^2 = \frac{K_t (3e-06)}{(38 \times 4)(8.854e-12)} \left(\frac{3}{60}\right)$$

$$\Rightarrow K_t = 28.1\text{N/m}$$

This is the total stiffness value (K_t) in the y direction (see Figure 25) required for the entire lateral microactuator system to cater for the assumed parameters listed above.

Chapter 3: Design of the Lateral Microactuator Switch

Using equation [14], the total actuation force of the microactuator is obtained as:

$$F_t = \frac{N\epsilon t}{d} V^2$$

$$\Rightarrow F_t = \frac{(38 \times 4)(8.854 \times 10^{-12})}{1} \left(\frac{60}{3}\right) (56^2)$$

$$= 84.4 \mu\text{N}$$

To cater for a contact force of $15 \mu\text{N}$, the required total actuation force needed is:

$$F_t' = F_t + 15 \mu\text{N}$$

$$= 99.4 \mu\text{N}$$

Assuming that the total stiffness of the system remains constant at 28.1N/m , using equation [14], we obtain the new driving voltage (V') as:

$$F_t' = \frac{N\epsilon t}{d} V'^2$$

$$99.4 \times 10^{-6} = \frac{(38 \times 4)(8.854 \times 10^{-12})}{1} \left(\frac{60}{3}\right) V'^2$$

$$\Rightarrow V' = 60.8 \text{V}$$

Therefore, a final driving voltage of 60.8V is required to produce an electrostatic actuation force of $99.4 \mu\text{N}$ to drive a lateral microactuator switch system with a total system stiffness of 28.1N/m ; with a switch-closing gap of $3 \mu\text{m}$ and to cater for a contact force of $15 \mu\text{N}$. The next step is to size up the folded flexure based on the requirement that the total stiffness value for the entire microactuator system is 28.1N/m . From equation [41], the stiffness of the folded flexure in the operating lateral direction is given as:

$$K = \frac{2Eb^3h}{L^3} \quad (\text{h is thickness of beam})$$

There must be a total of two flexure supports for the entire microactuator system. Figure 27 shows the entire microactuator system supported by two folded flexure supports. Note that the thickness (depth) of the folded flexure support is defined to be $60\mu\text{m}$ (i.e. $h = 60\mu\text{m}$). This is to make the beam thickness to be the same as the comb finger thickness in order to facilitate the microfabrication process.

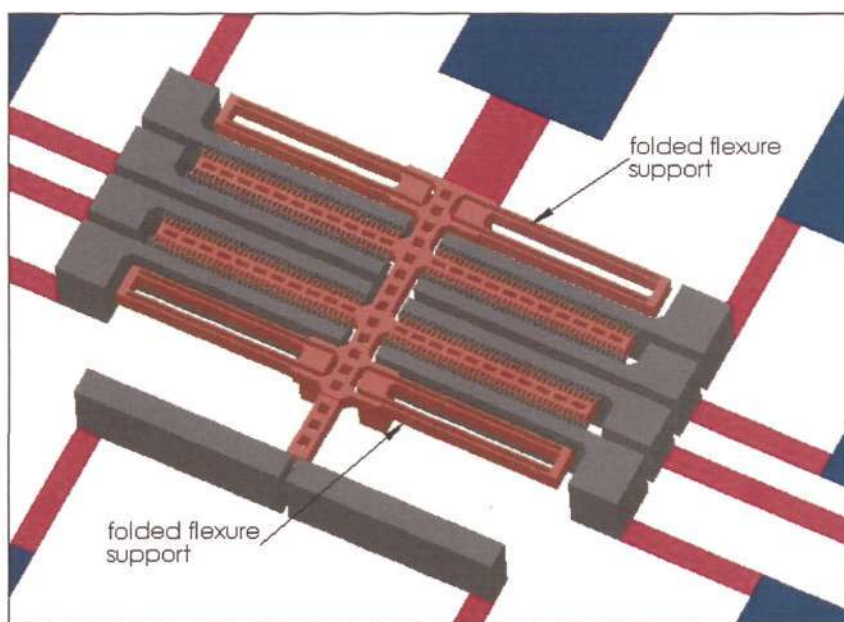


Figure 27: Folded-flexure supports for microactuator system

Consider one folded flexure support. From equation [41],

$$K = \frac{2Eb^3h}{L^3} \quad (\text{where } E = \text{Young's modulus of silicon})$$

$$\Rightarrow \frac{K_t}{2} = \frac{2Eh}{1} \left(\frac{b}{L}\right)^3$$

$$\frac{28.1}{2} = \frac{2(130e09)(60e-06)}{1} \left(\frac{b}{L}\right)^3$$

Chapter 3: Design of the Lateral Microactuator Switch

$$\left(\frac{b}{L}\right)^3 = 9.01e-07$$

$$\left(\frac{b}{L}\right) = 9.66e-03$$

Let the width (b) of the flexure beam be 5 μ m. Therefore,

$$\left(\frac{5e-06}{L}\right) = 9.66e-03$$

$$L = 518\mu\text{m}$$

The stiffness ratio as given in equation [42] is:

$$\begin{aligned} \frac{K_x}{K_y} &= \left(\frac{L}{b}\right)^2 \\ &= \left(\frac{518e-06}{5e-06}\right)^2 \\ &= 10733 \quad (\text{a desirable large value}) \end{aligned}$$

Therefore, each of the two folded flexure supports will have a beam width of 5 μ m, a total length of approximately 1.036mm (i.e. $\sim 2L$) and a beam thickness of 60 μ m.

The final step is to determine the resonant frequency of the translating structure. With reference to Figure 27, the translating structure is shaded in orange color. With the aid of a CAD software called 'SolidWorks', assuming the density of silicon to be 2330kg/m³, the mass of the translating structure is estimated to be 3.985e-08kg.

From equation [29], the resonant frequency of the system can be obtained as:

$$f_n = \frac{1}{2\pi} \sqrt{\frac{k_x}{m}}$$

Chapter 3: Design of the Lateral Microactuator Switch

$$\begin{aligned}
&= \frac{1}{2\pi} \sqrt{\frac{28.1}{3.985e-08}} \\
&= 4226\text{Hz} \\
&= 4.23\text{kHz} \quad (\text{a desirable large value})
\end{aligned}$$

Table 4 provides a summary of the various parameters defined and designed for the lateral MEMS microactuator switch:

Table 4: Summary of parameters for the lateral microactuator switch

Parameter	Specification
Total number of comb-drive fingers	152
Width of comb drive tooth (μm)	5
Air gap spacing between comb teeth (μm)	3
Thickness of comb-drive (μm)	60
Number of flexure supports per microactuator assembly	2
Total folded flexure length (μm)	1036
Flexure beam width (μm)	5
Flexure beam thickness (μm)	60
Switch contact gap (μm)	3
Total driving voltage (V)	60.8
Total stiffness of the microactuator assembly (N/m)	28.1
Total actuation force (μN)	99.4
Contact force (μN)	15
Mass of translating structure (kg)	3.985×10^{-8}
Resonant frequency of microactuator assembly (kHz)	4.23

3.3 Chapter summary

The chapter started off by explaining the basic operating principle of the mechanism involving electrostatic actuation. The various types of comb-drives are then listed and discussed. The advantages and disadvantages of the lateral motion comb-drive are

Chapter 3: Design of the Lateral Microactuator Switch

compared against the other types of comb-drives like vertical motion comb drive, transverse motion comb-drive and rotary motion comb-drive.

The general design specifications for the microactuator switch have been listed, and the various design features discussed in detail. A critical aspect of the microactuator design, the micromechanical flexure support, has been evaluated and discussed for the final selection of the type of flexure support to be employed in the proposed design.

Finally, all detailed calculations and sizing of the various parameters leading to the final proposed lateral microactuator switch design are presented.

Chapter 4: Finite Element Analysis of the Microactuator Structure

4.1 Introduction to the Finite Element Analysis (FEA)

The finite element method (FEM) is a general numerical analysis technique for obtaining approximate solutions to a wide variety of engineering problems. Finite element analysis techniques are increasingly being employed in engineering design and analysis to give accurate assessment of the behavior of a structure or a product. FEM has been used to replace, complete or partially, the testing of new and modified designs. Some of the more popular finite element codes available in the market include ANSYS, Nastran, Marc, Abaqus etc.

The FEM is both a powerful and popular analysis tool. It is applied to different types of problems of continua, but is most widely and extensively used for structural mechanics. The purpose of a structural analysis is to predict the response (which includes the stress, load, displacement, strain and temperature) of a structure subjected to external actions such as load, displacement or temperature. FEM provides engineers the necessary “quantitative yard-stick” as to the efficiency of a load-carrying component and possibility of its failure in service. Finite element analysis has become both an essential and necessary stage in the rational design of most engineering components.

In FEM, the continuum is divided into a series of elements which are connected at a finite number of points known as nodes. Irregular geometry, complex loading and boundary conditions can be handled by the FEM with ease. In a FEM model, the real

Chapter 4: Finite Element Analysis of the Microactuator Structure

structure is represented by an assemblage of numerous sub-divisions called finite elements. These finite elements can be arranged in virtually any manner. Each element is defined by its boundary geometry, material properties and other characteristic parameters such as its thickness and cross-sectional area.

The behavior of the element in relation to adjoining elements is assumed to be fully described by its boundary loads and displacements, which in turn are assumed to be a function consisting fully of a finite number of discrete variables nominally defined at the nodes. The geometrical mesh or convenient points on the boundaries' behavior of the complete idealized structure is determined as the aggregate behavior of its elements.

In FEM, the results obtained are only just as good as the finite element model itself, and the way in which the results are being interpreted. A prototype must always be constructed and tested at the early stages of any finite element analysis, in order to ensure high accuracy and reliability of the finite element model.

4.1.1 Validity and accuracy of finite element solutions

In general, the three pillars of mechanics, namely the constitutive law, compatibility and equilibrium conditions, have been well satisfied by finite element solutions. Since complete satisfaction cannot be achieved, the finite element results are not absolutely accurate. However, the stresses will tend to converge to the correct solutions with an increasing number of elements used.

Any finite element modeling must have sufficient degree of freedoms (DOF) in order to satisfy the convergence requirement so that more accurate results can be obtained

Chapter 4: Finite Element Analysis of the Microactuator Structure

with an increasing number of elements employed. A higher order element, having a greater number of DOF than the minimum required by a particular element shape, tends to be more flexible and is likely to give more accurate results. This is due to a better conformance to the actual deformation pattern.

Any element types used in the finite element model must first be tested to ensure convergence. The patch test is a critical test of element validity. It is a numerical test which determines whether an element (conforming or non-conforming) will produce convergent results. An element will converge to the continuum solution as long as the patch test is passed. Arrangement of the elements for the test is arbitrary since the patch must pass for any selected arrangements. All elements that satisfy the convergence criteria will pass the patch test, although the reverse is not true. It should be noted that an element that fails the patch test may provide convergence, but may converge to incorrect results.

4.1.2 Advantages and disadvantages of FEA

The various advantages and disadvantages of the FEM are listed and discussed as follows:

Advantages

- Diversity and flexibility

The FEM can be applied to a wide range of engineering problems. The region under analysis can have arbitrary shapes, loads and boundary conditions. The mesh can be generated with elements of different types, shapes and physical properties. This great versatility is contained within a single computer program, with the user-prepared

Chapter 4: Finite Element Analysis of the Microactuator Structure

input data controlling the selection of the problem type, geometry, element and boundary condition.

- High accuracy

A FEM is primarily a numerical analysis method. The finite element model gives a piece-wise approximation to the governing equations for all complicated shapes with high accuracy.

- Close resemblance between model and actual structure

One of the features of FEM is the close resemblance between the meshed and actual structure. The mesh is unlike a mathematical abstraction that is hard for one to visualize.

- Design optimization and cost minimization

The initial computation cost is high, but a design optimization can be obtained via the finite element simulation without having to build the actual model. On a long term basis, material cost and “trial-and-error” costs can both be minimized.

Disadvantages

- High cost incurred due to bad meshing

Bad meshing causes errors in finite element analyses, which will in turn lead to higher processing costs. A good engineering sense and experience is essential for the construction of a good mesh.

- Reliability of finite element results based on assumptions

The correct set of assumptions must be realized and made before any FEA in order to justify the validity of the finite element solutions.

- Specific finite element solutions

Chapter 4: Finite Element Analysis of the Microactuator Structure

A specific numerical result will be obtained for a specific problem. No closed-form expressions are available that permits analytical study of the effect of changes in the various parameters.

- Voluminous input and output data

Many input data are required, and the sorting and understanding of voluminous output data are unavoidable.

- Poor modeling

Poor modeling could result because of insufficient information on the boundary conditions, lack of understanding for the physical problem and the presence of certain unknown flexibility and constraints in some parts of the system.

4.1.3 General rules for finite element modeling

The general rules for finite element modeling are presented as shown:

- A more refined mesh is needed for a stress analysis as compared to a displacement analysis.
- Nodes are placed at supports, load points and other locations where information is required.
- A uniform mesh pattern with equal nodal spacing should be used when applicable for practical reasons. Dimensions of adjacent elements should not be changed by more than a factor of two when making transitions from a coarse-to-fine region. Transition could be made over a series of elements in order to maintain this factor.
- Aspect ratios should be kept as close to unity as possible for triangular and quadrilateral elements.

Chapter 4: Finite Element Analysis of the Microactuator Structure

- Extreme acute and obtuse angles should be avoided for triangular and quadrilateral elements respectively. This will avoid over-distortion of the elements.
- Poisson's ratio should be lower than 0.5. Special elements are required for materials having a Poisson's ratio approaching the value of 0.5.
- Lines defining areas and areas defining volumes must attain non-zero values.
- Elements should not extend across discontinuities and changes in thickness. Additional nodes must be added and smaller elements must be used in these areas.

4.1.4 Introduction to ANSYS

The finite element software program employed for this project is ANSYS version 8.1. The ANSYS program is a large-scale, general purpose computer program that is used to obtain the solution of various types of engineering analyses. The program is highly versatile in the sense that it is able to perform a wide variety of analyses, ranging from structural, non-structural to bio-chemical aspects.

The wide variety of finite elements that are available in the library enhances the versatility aspect of the program in analyzing 2-D and 3-D problems under varying scenarios (where certain elements are preferred and recommended). Loading on the structure may take the form of forces, displacements, pressures, temperatures or response spectra. Loading may be arbitrary functions of time for linear and non-linear dynamic analyses. Loading for heat transfer analyses include internal heat generation, convection and radiation boundaries, and specified temperatures or heat flows.

Chapter 4: Finite Element Analysis of the Microactuator Structure

The ANSYS program consists of three phases, namely pre-processing, solution and post-processing:

- Pre-processing >> This is the phase for which the specification of the data needed to perform a solution is carried out. Solid models are created and meshed with the selected elements. Definition of the material properties, boundary conditions and types of loading are done during this phase.
- Solution >> This is the phase where the solution to the FEA of the finite element is obtained. Specifications are made on the analysis type, analysis options, load data and analysis load-step options. This is followed by the initiation for the finite element solution. The specified analysis type will indicate the set of governing equations used in the solution process.
- Post-processing >> This is the phase where the results calculated in the solution phase are operated and obtained. The results may include displacements, temperatures, stresses, strains, velocities and heat flow. The output from this phase is in graphic display mode and/or tabular report form. Display may be made on-line during an interactive post-processing session at a graphic display device, or may be diverted for off-line plotting where data can be examined immediately.

The ANSYS program is designed to operate fully interactive, fully batch or a combination of both modes. Interactive runs are self-teaching and lead to lesser dependence on user manuals. Plots and outputs are instantly produced, and enable immediate editing and corrections to be made where necessary. The drawback for interactive runs is that CPU time may be charged at a premium rate when connected to the host machine. It is of common practice these days that the pre-processing phase

Chapter 4: Finite Element Analysis of the Microactuator Structure

to be done interactively, the solution phase be submitted as a batch job and the post-processing phase be carried out either interactively or batch. Data input is essentially the same for both modes.

4.1.5 General FEM procedures

The FEM procedures are listed and described as follows:

1. The boundary and interior of the solution domain are subdivided by points, lines or surfaces into a finite number of discrete finite elements.
2. A discrete number of nodal points are established within the mesh. The mesh divides the entire region into a finite number of elements.
3. Integer numberings are assigned to both the nodes and elements.
4. The DOF of the system is determined, which is the product of the number of nodes and the number of parameters defining per node.
5. The topology of the mesh assigned for the system is defined.
6. Material properties or coefficients for nodal points of elements under consideration are defined.
7. The necessary element equations are established.
8. The system equation is formed by the addition of contribution from each individual element.
9. The appropriate boundary conditions or constraints are applied before the solution process for the unknown nodal parameters.
10. Solution of the system equation is carried out.
11. The entire procedure is repeated if necessary, by generating a finer mesh incorporating a greater number of nodal points and elements.

-
12. The analysis results are compared with the theoretical results, in order to ensure reliability and validity of the finite element model.

4.2 Finite element analysis of micromechanical flexure designs

Finite element analysis is performed on various micromechanical flexure types, namely the straight-plate flexure, fixed-fixed beam flexure, crab-leg flexure and folded flexure. As micromechanical flexures are designed to generate small deflections, a static linear analysis mode is employed. A three-dimensional 10-noded tetrahedral structural solid element (SOLID92) is chosen as the element type used for the analysis for its ease of meshing. Translations in the x, y and z axes are obtained at each of the 10 nodes. The analysis is performed for the various types of flexures to verify the theoretical stiffness values against the values obtained via FEM. This would justify the use of theoretical equations representing the flexure stiffness in the design of the microactuator switch. Structural analysis is performed to check on the structural integrity of the designed flexure under the stipulated loading conditions.

According to MEMS material database [68], each material property of bulk silicon varies due to process variability as every laboratory doing the fabrication will have its own process control regime. The parameters used for the finite element analysis of the flexures are listed as follows:

- Material : Bulk silicon
 - Young's Modulus : 130GPa
 - Fracture stress : 7GPa
 - Density : 2330kg/m³
 - Poisson's ratio : 0.2
-

- Element type : SOLID92

4.2.1 Straight-plate flexure

The required total stiffness for the system in the operating direction is 28.1N/m. There will be four identical straight-plate flexures supporting the system. In this case, only one flexure will be modeled and analyzed. Hence the stiffness (in the operating direction) per straight-plate flexure is 7.025N/m.

From equation [31], the dimensions of the straight-plate flexure to cater for a stiffness of 7.025N/m are as follows:

- Length (L) = 518 μ m
- Width (t) = 60 μ m
- Thickness (b) = 7.94 μ m

Figure 28 shows the CAD model of a straight-plate flexure generated for FEA:

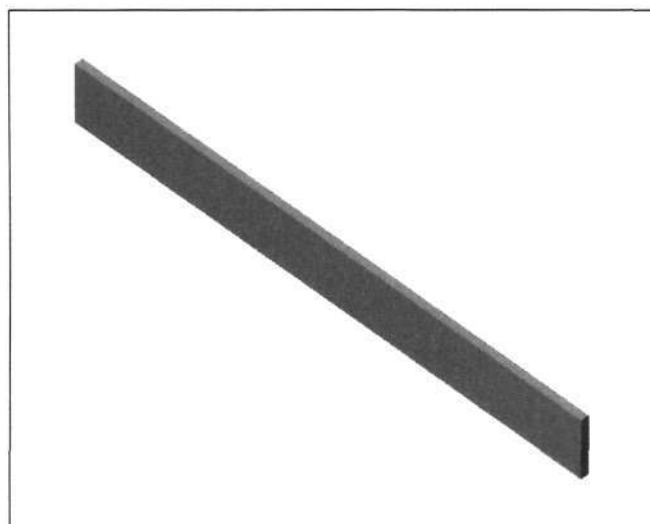


Figure 28: FE model of straight-plate flexure

Chapter 4: Finite Element Analysis of the Microactuator Structure

The following figure shows the loading scheme for the straight-plate flexure:

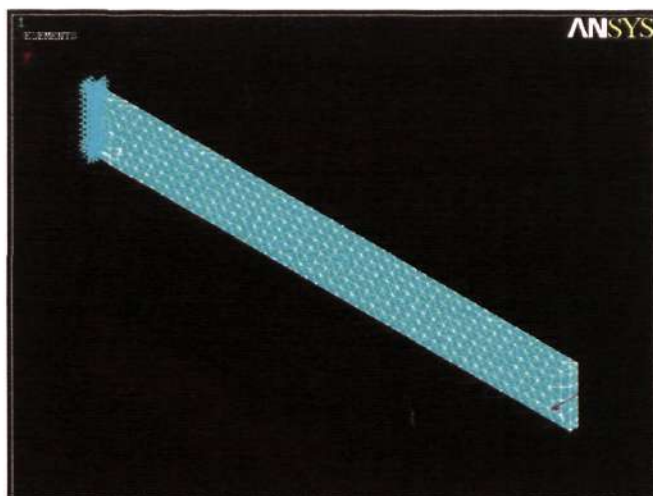


Figure 29: Loading scheme for straight-plate flexure

The analysis is carried out for various loading levels. The simulated displacement values are compared against theoretical values obtained from Equation [31]. The corresponding displacement values obtained for each loading level are shown in Table 5:

Table 5: Loading against displacement values (straight-plate flexure)

Applied load / F (μN)	Simulated displacement / Δ (μm)	Theoretical displacement / Δ (μm)	Percentage deviation / (%)
0	0.000	0.000	0.000
5	0.708	0.712	0.526
10	1.420	1.423	0.245
15	2.120	2.135	0.713
20	2.840	2.847	0.245
25	3.540	3.559	0.526
30	4.250	4.270	0.479
35	4.960	4.982	0.446

Chapter 4: Finite Element Analysis of the Microactuator Structure

Figures 30 to 32 show the FEA results obtained:

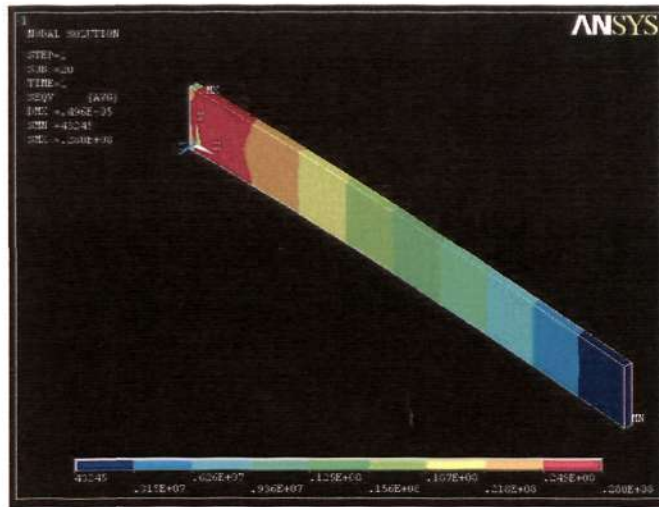


Figure 30: Nodal solution for Von Mises stresses (straight-plate flexure)

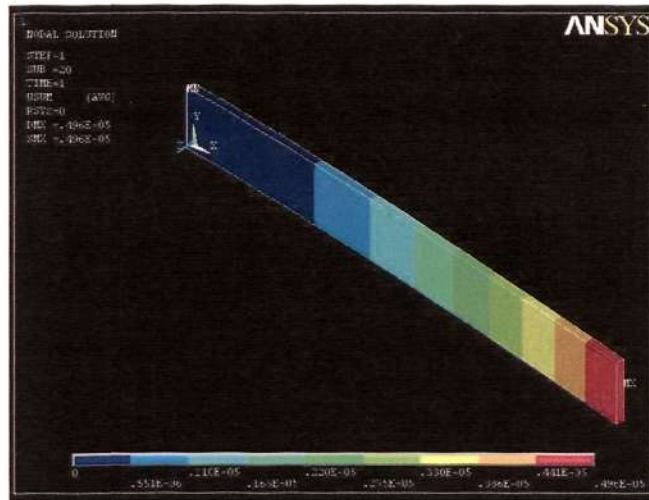


Figure 31: Nodal solution for displacements (straight-plate flexure)

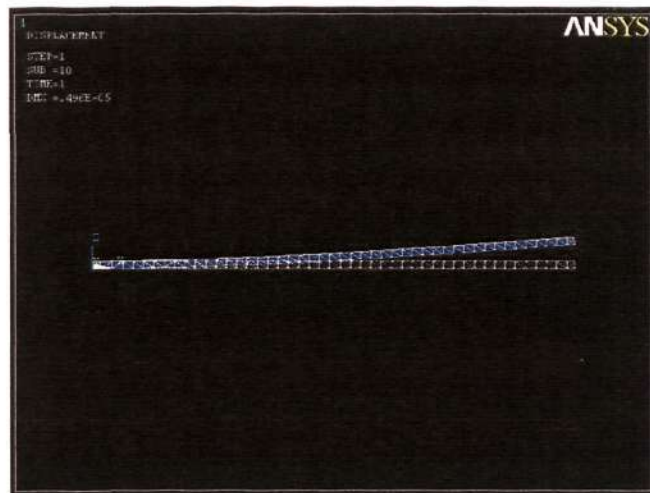


Figure 32: Deformed and undeformed shape (straight-plate flexure)

Chapter 4: Finite Element Analysis of the Microactuator Structure

From the FEM results obtained, the region of maximum stress is located at the constrained end of the straight-plate flexure. Maximum stress level obtained is 28MPa. Note that silicon is a brittle material and fractures if the yield stress is larger than the stress needed for fracture under the operating conditions. Since the yield stress decreases with increasing temperature, plastic deformation will occur at some temperature. The maximum stress level obtained is only 28MPa and this stress level is very low for operating conditions at room temperature. Maximum displacement (in the operating direction) obtained is 4.96 μm (for a loading level of 35 μN) and is located at the tip of the free end of the flexure. There is good agreement between the FE results obtained and the theoretical values. Maximum percentage deviation obtained is 0.713%. Figure 33 shows a plot for the applied load against displacement values.

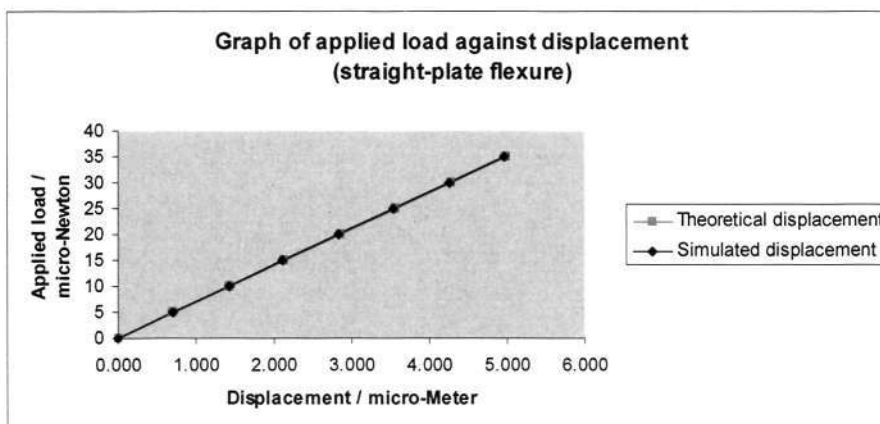


Figure 33: Graph of applied load against displacement (straight-plate flexure)

The analysis of the simple straight-plate flexure also serves as a patch test to justify the validity of the selected element type. The selected element type is shown to produce convergent results with high accuracy when compared against theoretical ones.

4.2.2 Fixed-fixed beam flexure

The required total stiffness for the system in the operating direction is 28.1N/m. There will be two identical fixed-fixed beam flexures supporting the system. In this case, only one flexure will be modeled and analyzed. Hence the stiffness (in the operating direction) per fixed-fixed beam flexure is 14.05N/m. From equation [35], the dimensions of the fixed-fixed beam flexure to cater for a stiffness of 14.05N/m are as follows:

- Length (L) = 518 μ m
- Width (h) = 60 μ m
- Thickness (b) = 5 μ m

Figure 34 shows the CAD model of a fixed-fixed beam flexure generated for FEA:

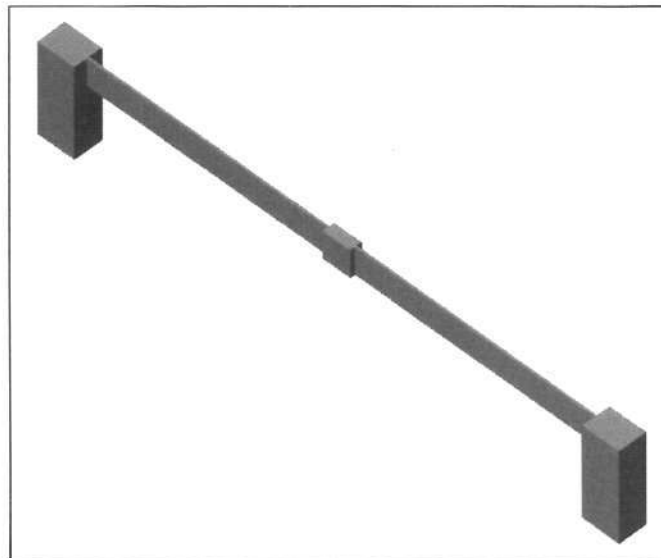


Figure 34: FE model of fixed-fixed beam flexure

Chapter 4: Finite Element Analysis of the Microactuator Structure

The following figure shows the loading scheme for the fixed-fixed beam flexure:

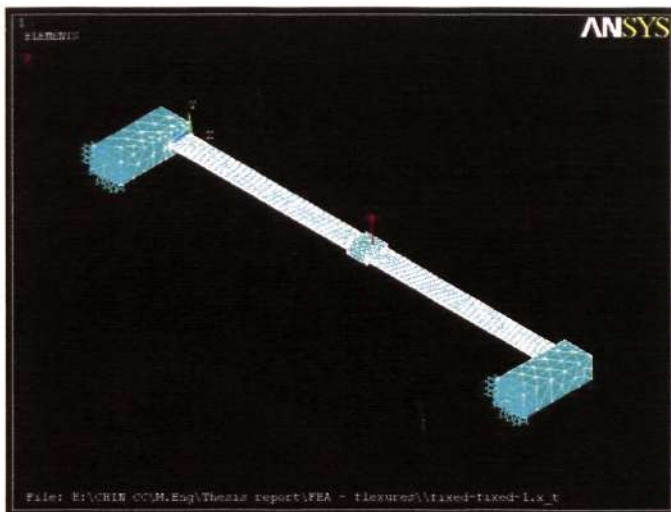


Figure 35: Loading scheme for fixed-fixed beam flexure

The analysis is carried out for various loading levels. The simulated displacement values are compared against theoretical values obtained from Equation [35]. The corresponding displacement values obtained for each loading level are shown in Table 6:

Table 6: Loading against displacement values (fixed-fixed beam flexure)

Applied load / F (μN)	Simulated displacement / Δ (μm)	Theoretical displacement / Δ (μm)	Percentage deviation / (%)
0	0.000	0.000	0.000
10	0.721	0.712	-1.301
20	1.430	1.423	-0.458
30	2.150	2.135	-0.692
40	2.860	2.847	-0.458
50	3.580	3.559	-0.598
60	4.300	4.270	-0.692
70	5.010	4.982	-0.558

Chapter 4: Finite Element Analysis of the Microactuator Structure

Figures 36 to 38 show the FEA results obtained:

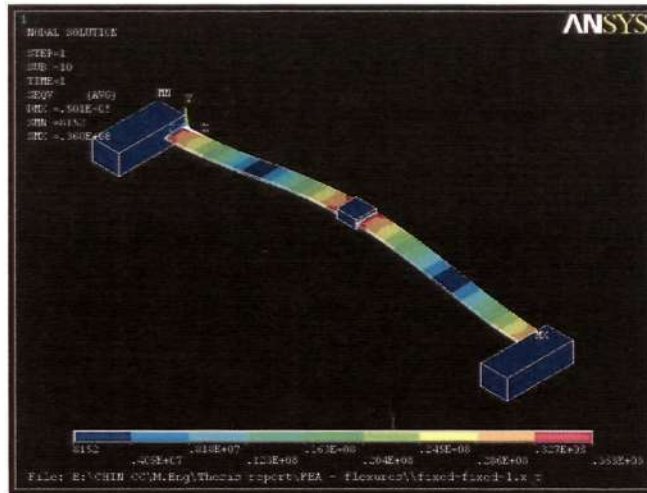


Figure 36: Nodal solution for Von Mises stresses (fixed-fixed beam flexure)

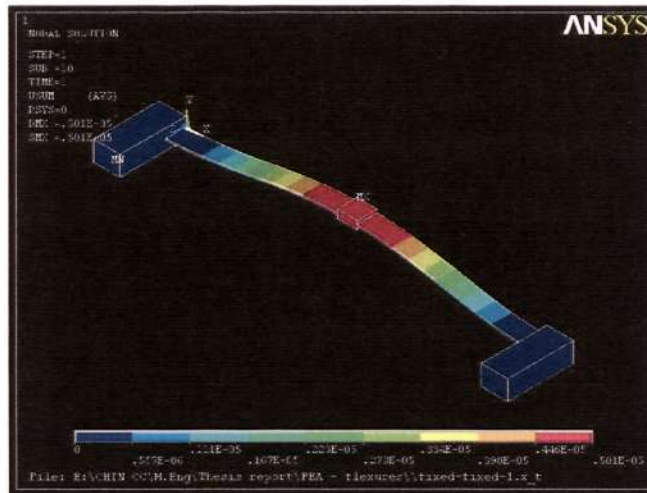


Figure 37: Nodal solution for displacements (fixed-fixed beam flexure)

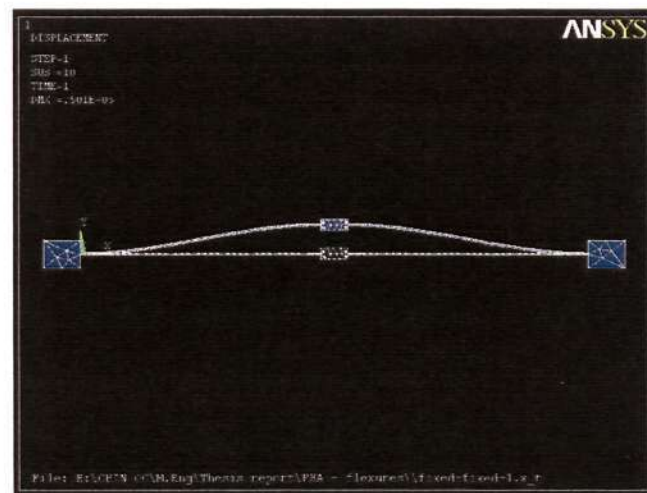


Figure 38: Deformed and undeformed shape (fixed-fixed beam flexure)

Chapter 4: Finite Element Analysis of the Microactuator Structure

(Note: The displacement as shown is not to scale with reference to flexure dimensions.)

From the FEM results obtained, the region of maximum stress is located at both the constrained ends of the fixed-fixed beam flexure. Maximum stress level obtained is 36.8MPa. This stress level is very low for operating conditions at room temperature. Maximum displacement (in the operating direction) obtained is $5.01\mu\text{m}$ (for a loading level of $70\mu\text{N}$) and is located at the center of the flexure. There is good agreement between the FE results obtained and the theoretical values. Maximum percentage deviation obtained is 1.301%. Figure 39 shows a plot for the applied load against displacement values.

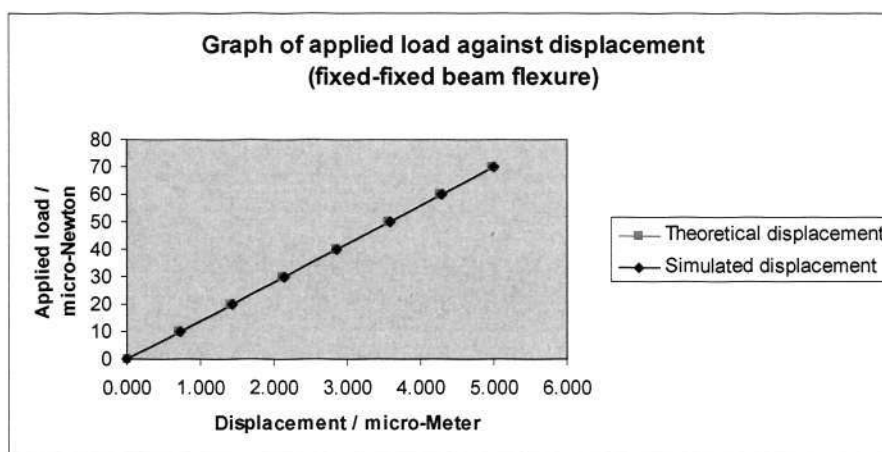


Figure 39: Graph of applied load against displacement (fixed-fixed beam flexure)

4.2.3 Crab-leg flexure

The required total stiffness for the system in the operating direction is 28.1N/m . There will be two identical crab-leg flexures supporting the system. In this case, only one flexure will be modeled and analyzed. Hence the stiffness (in the operating direction) per crab-leg flexure is 14.05N/m . From equation [38], the dimensional of the fixed-fixed flexure to cater for a stiffness of 14.05N/m are as follows:

Chapter 4: Finite Element Analysis of the Microactuator Structure

- Length (L_1) = 518 μm
- Length (L_2) = 140 μm
- Width (h) = 60 μm
- Thickness (b) = 5.34 μm

It should be noted that as a guideline for the design of the crab-leg flexure, the value of L_2 should be approximately one-third the value of L_1 . With L_1 remaining constant, the stiffness value of the crab-leg flexure will decrease as L_2 increases.

Figure 40 shows the CAD model of a crab-leg flexure generated for FEA:

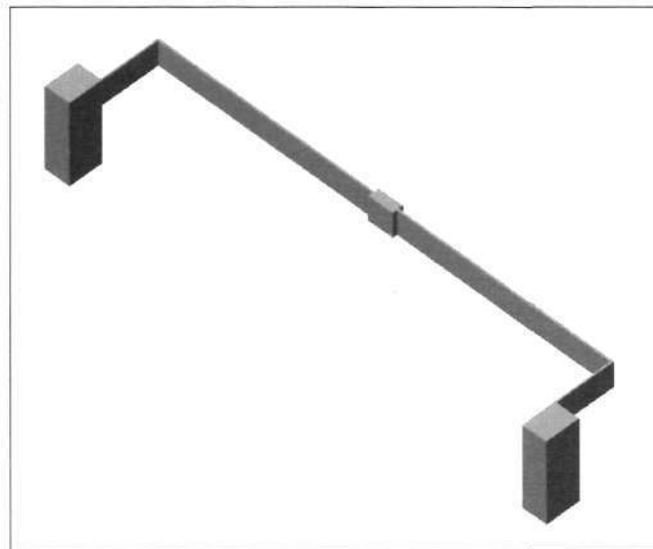


Figure 40: FE model of crab-leg flexure

Chapter 4: Finite Element Analysis of the Microactuator Structure

The following figure shows the loading scheme for the crab-leg flexure:

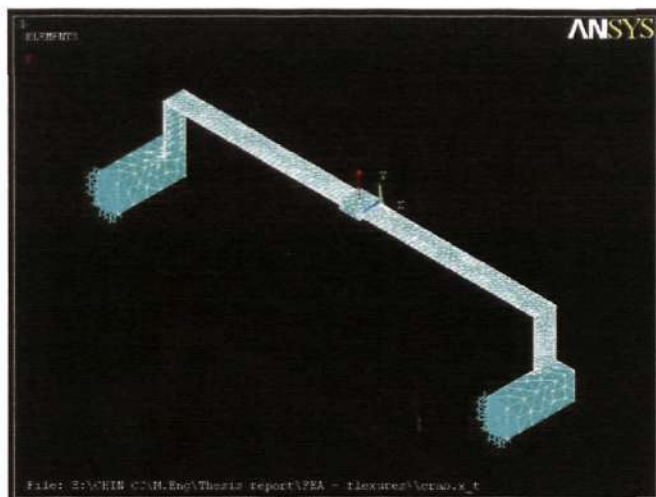


Figure 41: Loading scheme for crab-leg flexure

The analysis is carried out for various loading levels. The simulated displacement values are compared against theoretical values obtained from Equation [38]. The corresponding displacement values obtained for each loading level are shown in Table 7:

Table 7: Loading against displacement values (crab-leg flexure)

Applied load / F (μN)	Simulated displacement / Δ (μm)	Theoretical displacement / Δ (μm)	Percentage deviation / (%)
0	0.000	0.000	0.000
10	0.692	0.712	2.774
20	1.380	1.423	3.055
30	2.080	2.135	2.587
40	2.770	2.847	2.704
50	3.460	3.559	2.774
60	4.150	4.270	2.821
70	4.840	4.982	2.854

Chapter 4: Finite Element Analysis of the Microactuator Structure

Figures 42 to 44 show the FEA results obtained:

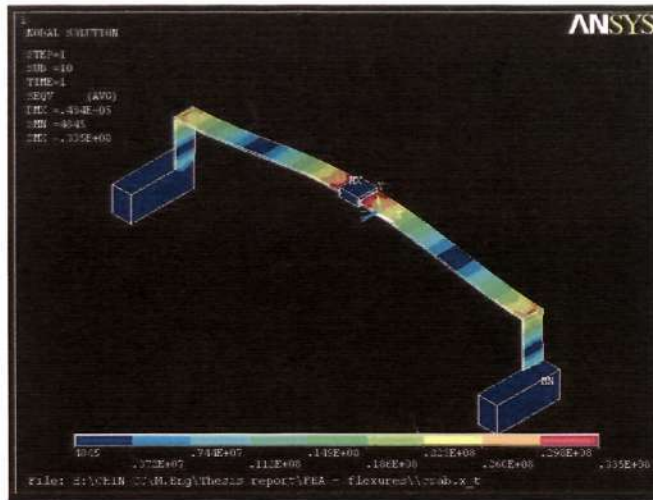


Figure 42: Nodal solution for Von Mises stresses (crab-leg flexure)

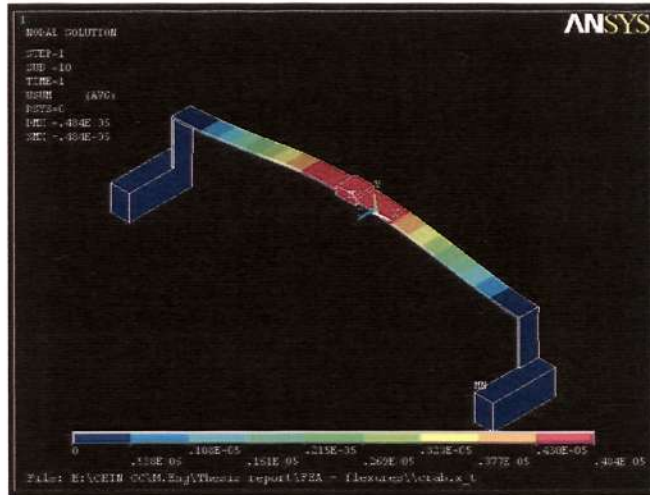


Figure 43: Nodal solution for displacements (crab-leg flexure)

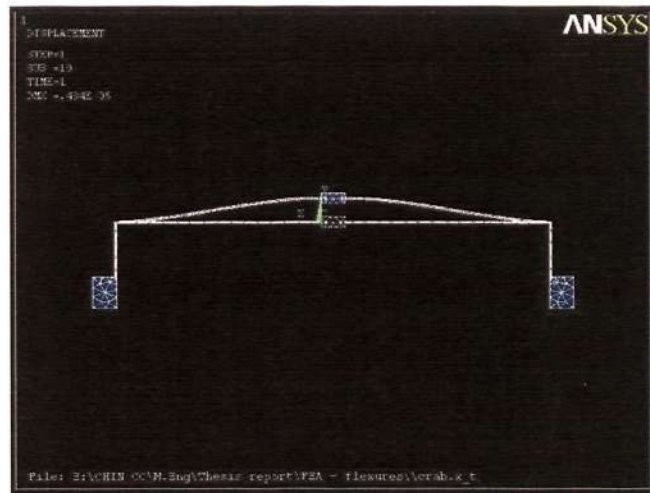


Figure 44: Deformed and undeformed shape (crab-leg flexure)

Chapter 4: Finite Element Analysis of the Microactuator Structure

(Note: The displacement as shown is not to scale with reference to flexure dimensions.)

From the FEM results obtained, the region of maximum stress is located at both constrained ends of the elbow of the crab-leg flexure. Maximum stress level obtained is 33.5MPa. This stress level is very low for operating conditions at room temperature. Maximum displacement (in the operating direction) obtained is 4.84 μm (for a loading level of 70 μN) and is located at the center of the flexure. There is good agreement between the FE results obtained and the theoretical values. Maximum percentage deviation obtained is 3.055%. Figure 45 shows a plot for the applied load against displacement values.

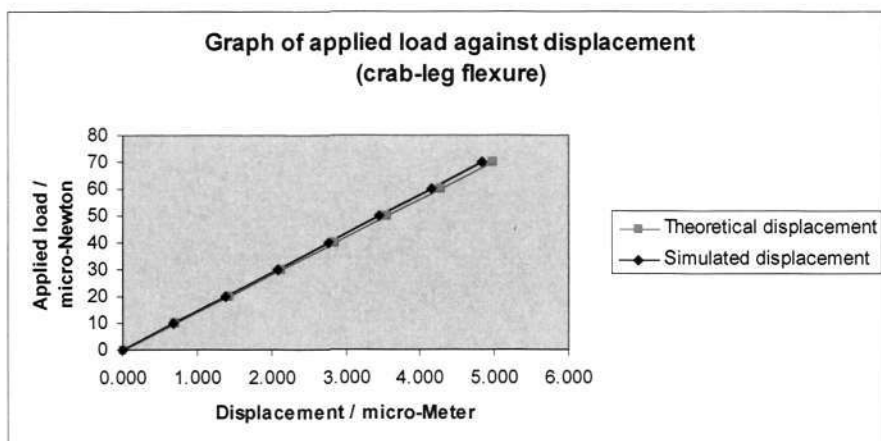


Figure 45: Graph of applied load against displacement (crab-leg flexure)

4.2.4 Folded flexure

The required total stiffness for the system in the operating direction is 28.1N/m. There will be two identical folded flexures supporting the system. In this case, only one flexure will be modeled and analyzed. Hence the stiffness (in the operating direction) per folded flexure is 14.05N/m. From equation [41], the dimensional of the folded flexure to cater for a stiffness of 14.05N/m are as follows:

Chapter 4: Finite Element Analysis of the Microactuator Structure

- Length (L) = 518 μ m
- Width (h) = 60 μ m
- Thickness (b) = 5 μ m

Figure 46 shows the CAD model of a folded flexure generated for FEA:

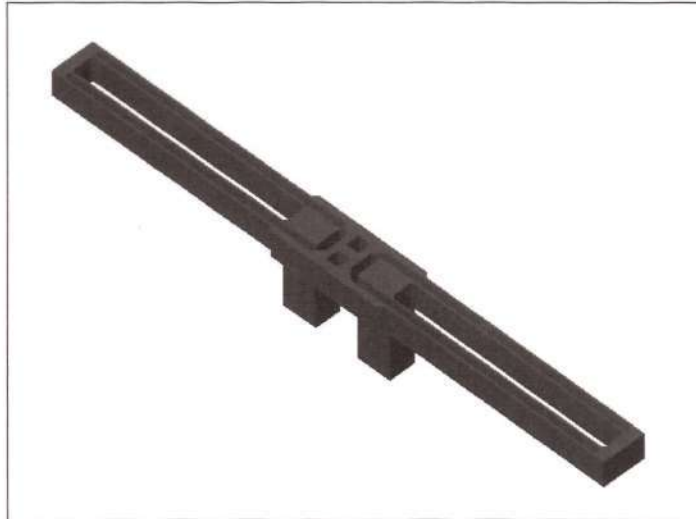


Figure 46: FE model of folded flexure

The following figure shows the loading scheme for the folded flexure:

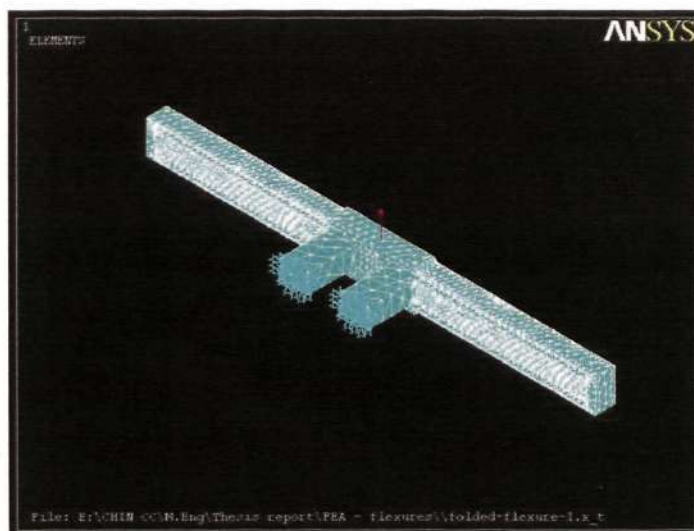


Figure 47: Loading scheme for folded flexure

Chapter 4: Finite Element Analysis of the Microactuator Structure

The analysis is carried out for various loading levels. The simulated displacement values are compared against theoretical values obtained from Equation [41]. The corresponding displacement values obtained for each loading level are shown in Table 8:

Table 8: Loading against displacement values (folded flexure)

Applied load / F (μN)	Simulated displacement / Δ (μm)	Theoretical displacement / Δ (μm)	Percentage deviation / (%)
0	0.000	0.000	0.000
10	0.684	0.712	3.898
20	1.360	1.423	4.460
30	2.040	2.135	4.460
40	2.730	2.847	4.109
50	3.410	3.559	4.179
60	4.090	4.270	4.226
70	4.780	4.982	4.059

Figures 48 to 50 show the FEA results obtained:

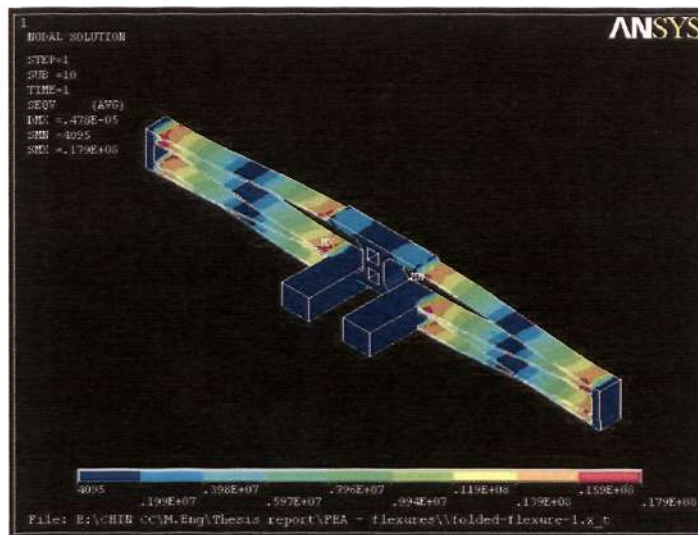


Figure 48: Nodal solution for Von Mises stresses (folded flexure)

Chapter 4: Finite Element Analysis of the Microactuator Structure

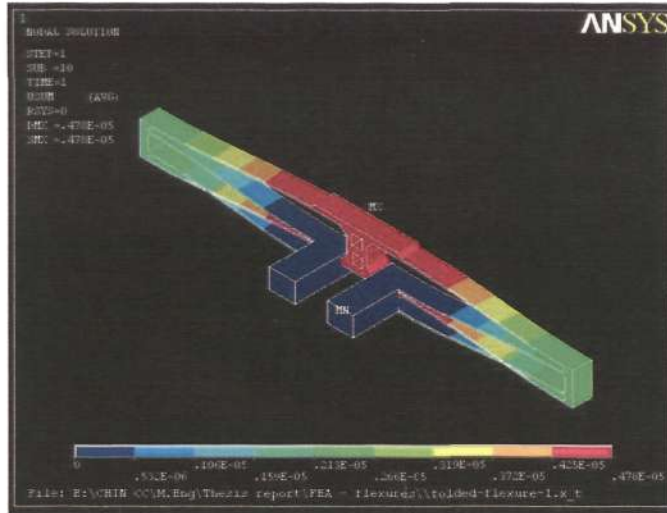


Figure 49: Nodal solution for displacements (folded flexure)

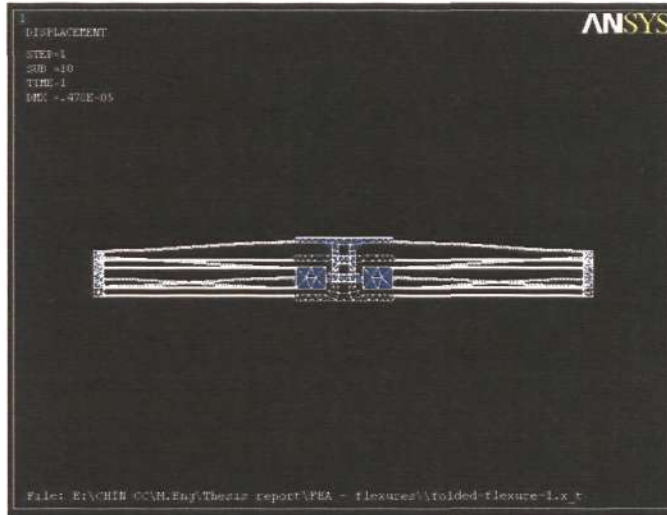


Figure 50: Deformed and undeformed shape (folded flexure)

(Note: The displacement as shown is not to scale with reference to flexure dimensions.)

From the FEM results obtained, the regions of maximum stress are located at both ends of the truss of the folded flexure, and at the constrained ends of the support. Maximum stress level obtained is 17.9MPa. This stress level is very low for operating conditions at room temperature. Maximum displacement (in the operating direction) obtained is $4.78\mu\text{m}$ (for a loading level of $70\mu\text{N}$) and is located at the center of the flexure. There is good agreement between the FE results obtained and the theoretical

Chapter 4: Finite Element Analysis of the Microactuator Structure

values. Maximum percentage deviation obtained is 4.460%. Figure 51 shows a plot for the applied load against displacement values.

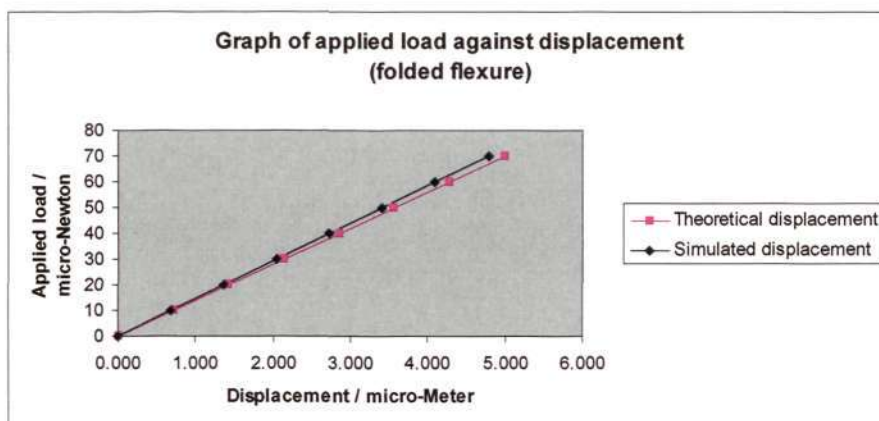


Figure 51: Graph of applied load against displacement (folded flexure)

The folded flexure design strongly reduces the development of axial forces (in the direction orthogonal to the operating direction) and exhibits a much larger linear deflection range as compared to other flexure types. The stiffness ratio for small deflections is the same as that of fixed-fixed flexure, thus the folded flexure is very suitable for large deflection linear actuators. FEM results have also shown that there is very good linearity between the simulated displacement values and the theoretical predicted ones, with a maximum percentage deviation no more than 4.5%. The folded flexure design is also robust with very low stresses induced for the applied loading. With all the discussed issues in mind, the folded flexure design is therefore chosen as the micromechanical flexure support for the proposed microactuator switch.

4.3 Fatigue

4.3.1 Introduction

Static or quasi-static loading is rarely observed in modern engineering practice, making it essential for the designer to address the implication of repeated loads,

Chapter 4: Finite Element Analysis of the Microactuator Structure

fluctuating loads and rapidly applied loads. Fluctuating or cyclic loads induce fluctuating or cyclic stress that often results in failure by fatigue. Damage done during the fatigue process is cumulative and is generally unrecoverable.

Fatigue, or progressive fracture, is defined as the progressive localized permanent structural change that occurs in a material subjected to repeated or fluctuating strains at stress having a maximum value less than the tensile strength of the material. Fracture of a structural component due to repeated cycles of load or fluctuating loads is commonly referred to as fatigue failure or fatigue fracture. The corresponding number of load cycles or the time during which the component is subjected to these loads before fracture occurs is referred to as fatigue life of the component.

The fatigue life of a component is affected by many factors listed as follows:

- Type of load >> uni-axial, bending or torsion
- Nature of load-displacement curve >> linear or non-linear
- Frequency of load repetitions or cycling
- Load history >> cyclic load with constant or variable amplitude, random etc.
- Size of component
- Material flaws
- Manufacturing method >> surface roughness, notches etc.
- Operating temperature >> high temperature results in creep and low temperature results in brittleness
- Environmental operating conditions >> corrosion etc.

Chapter 4: Finite Element Analysis of the Microactuator Structure

In practice, the actual estimation of fatigue life is difficult to obtain because for many materials, a small change in the discussed conditions may strongly affect fatigue life. The fatigue process embraces two domains of cyclic stressing or straining that are significantly different in character, and in each of which failure is probably produced by different physical mechanisms.

One domain of cyclic loading is that for which significant plastic strain occurs during each cycle. This domain is associated with high loads and short lives, or low number of cycle to produce fatigue failure (low-cycle fatigue). Low-cycle fatigue is typically associated with lives from one up to 10^5 cycles. The other domain of cyclic loading is that for which the strain cycles are largely confined to the elastic range. This domain is associated with low loads and long lives, or high number of cycles to produce fatigue failure (high-cycle fatigue). High-cycle fatigue is typically associated with lives greater than 10^5 cycles.

4.3.2 Fatigue loading

The simplest fatigue stress spectrum to which a component may be subjected is a zero-mean sinusoidal stress-time pattern of constant amplitude and fixed frequency, applied for a specified number of cycles. Such a stress pattern is often referred to as completely reversed cyclic stress.

Figure 52 shows several constant-amplitude stress-time patterns. A completely reversed cyclic stress-time pattern is shown in Figure 52(a).

Chapter 4: Finite Element Analysis of the Microactuator Structure

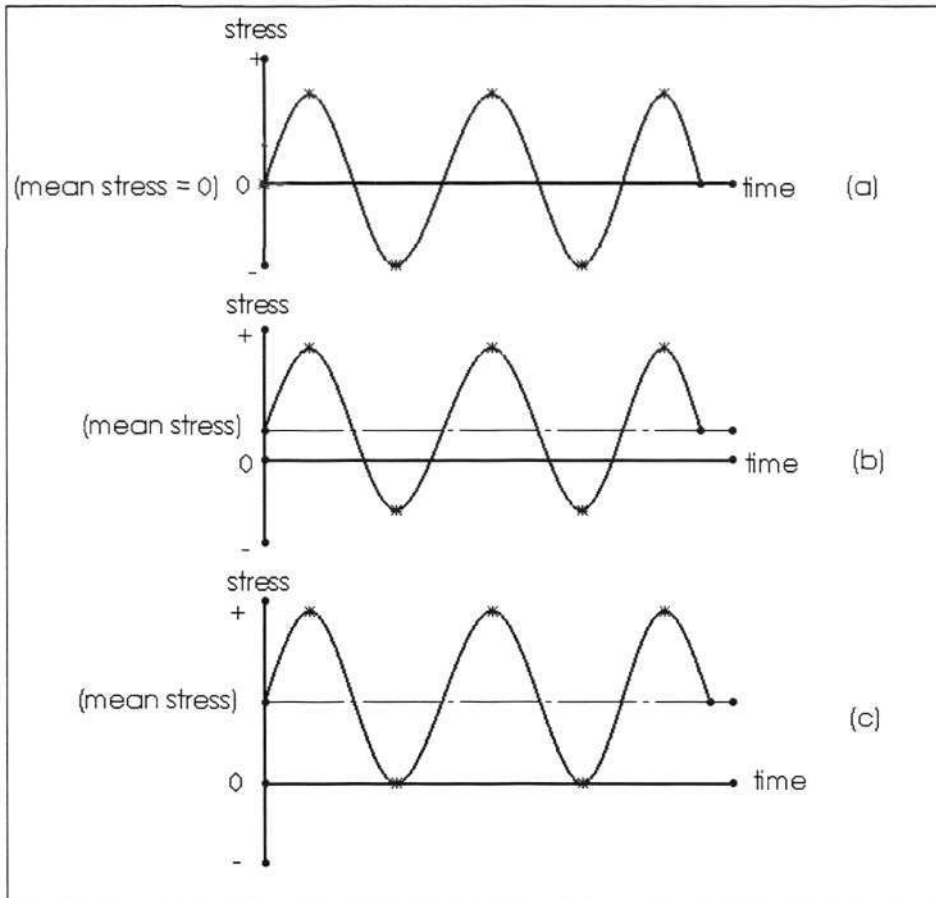


Figure 52: Constant stress-time patterns (a) completely reversed, $R = -1$;
(b) non-zero mean stress and (c) released tension, $R = 0$

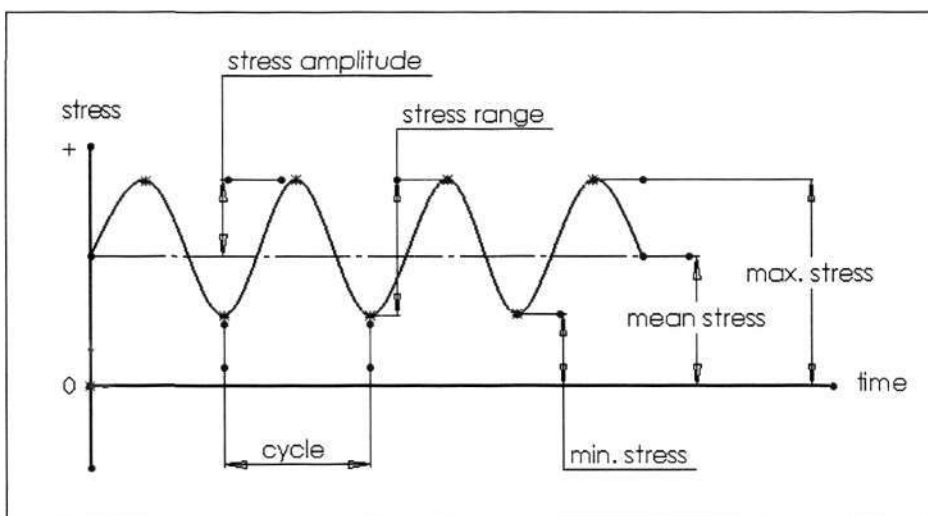


Figure 53: Typical cyclic loading parameters

Chapter 4: Finite Element Analysis of the Microactuator Structure

Figure 53 shows the typical cyclic loading parameters. With reference to Figure 53, the following definitions are used to define a stress cycle with both alternating and mean stress:

- Stress range ($\Delta\sigma$) >> algebraic difference between the maximum and minimum stress in a cycle

$$\Rightarrow \Delta\sigma = \sigma_{\max} - \sigma_{\min}$$

- Stress amplitude (σ_a) >> one-half the stress range

$$\Rightarrow \sigma_a = \frac{\Delta\sigma}{2} = \frac{\sigma_{\max} - \sigma_{\min}}{2}$$

- Mean stress (σ_m) >> algebraic mean of the maximum and minimum stress in a cycle

$$\Rightarrow \sigma_m = \frac{\sigma_{\min} + \sigma_{\max}}{2}$$

- Stress ratio (R) >> ratio defined for the representation of the mean stress

$$\Rightarrow R = \frac{\sigma_{\min}}{\sigma_{\max}}$$

- Amplitude ratio (A) >> ratio defined for an alternative representation of the mean stress

$$\Rightarrow A = \frac{\sigma_a}{\sigma_m} = \frac{1-R}{1+R}$$

Note that any two of the mentioned quantities, except the combination of σ_a and $\Delta\sigma$ or the combination of R and A, are sufficient to completely describe the stress-time pattern.

Chapter 4: Finite Element Analysis of the Microactuator Structure

A second type of stress-time pattern that is often encountered is the non-zero mean spectrum as shown in Figure 52(b). This pattern is very similar to the completely reversed case, except that the mean stress is either tensile or compressive, in any event different from zero. The non-zero mean case may be treated as a static stress equal in magnitude to mean σ_m with a superposed completely reverse cyclic stress of amplitude σ_a .

A special type of non-zero mean stress is shown in Figure 52(c). In this case, the minimum stress σ_{\min} is zero, meaning that the stress ranges from zero up to some tensile maximum and then back to zero. This type of stressing is often called released tension. For released tension it is noted that the mean stress is half the maximum stress, or $\sigma_m = \frac{\sigma_{\max}}{2}$. A similar but less frequently encountered stress-time pattern is

released compression, where $\sigma_{\max} = 0$ and $\sigma_m = \frac{\sigma_{\min}}{2}$.

4.3.3 S-N-P curves

Basic fatigue data in the high-cycle life range can be conveniently displaced on a plot of cyclic level versus the logarithm of life, or alternatively, on a log-log plot of stress versus life. These plots are known as S-N curves and constitute design information of fundamental importance for components subjected to repeated loading.

Due to the scatter of fatigue life data at any given stress level, it must be recognized that there is not only one S-N curve for a given material, but a family of S-N curves with probability of failure as a parameter. These curves are called S-N-P curves, or curves with constant probability of failure on a stress versus life plot.

4.3.4 The influence of non-zero mean stress

It is very important to know the influence of mean stress on fatigue behavior so that basic completely reversed laboratory data may be used for the design of components that are subjected to non-zero mean cyclic stress.

Some empirical relations are proposed to describe the effects of mean stress. Three such relations for 1-D testing are described as follows:

- Soderberg relation >> The Soderberg relation yields conservative estimates of critical stress amplitude σ_a (or range of $2\sigma_a$).

$$\Rightarrow \frac{\sigma_a}{\sigma_{am}} + \frac{\sigma_m}{Y} = 1 \quad [44]$$

where σ_a = stress amplitude

σ_{am} = fatigue strength for a given N for zero mean stress

Y = yield stress

- Gerber relation >> The Gerber relation yields fairly good estimates for σ_a for ductile materials.

$$\Rightarrow \frac{\sigma_a}{\sigma_{am}} + \left(\frac{\sigma_m}{\sigma_u}\right)^2 = 1 \quad [45]$$

where σ_u = ultimate strength

- Goodman relation >> The Goodman relation gives reasonably good results for brittle materials, whereas it is conservative for ductile materials.

$$\Rightarrow \frac{\sigma_a}{\sigma_{am}} + \frac{\sigma_m}{\sigma_u} = 1 \quad [46]$$

The three relations are interpreted in Figure 54 as shown. For any mean stress σ_m , the ordinate to a particular curve gives the magnitude of σ_a for that relation. The dashed

Chapter 4: Finite Element Analysis of the Microactuator Structure

line CD is generally used along with the Gerber and Goodman relations since failure by general yielding is assumed to occur along the line.

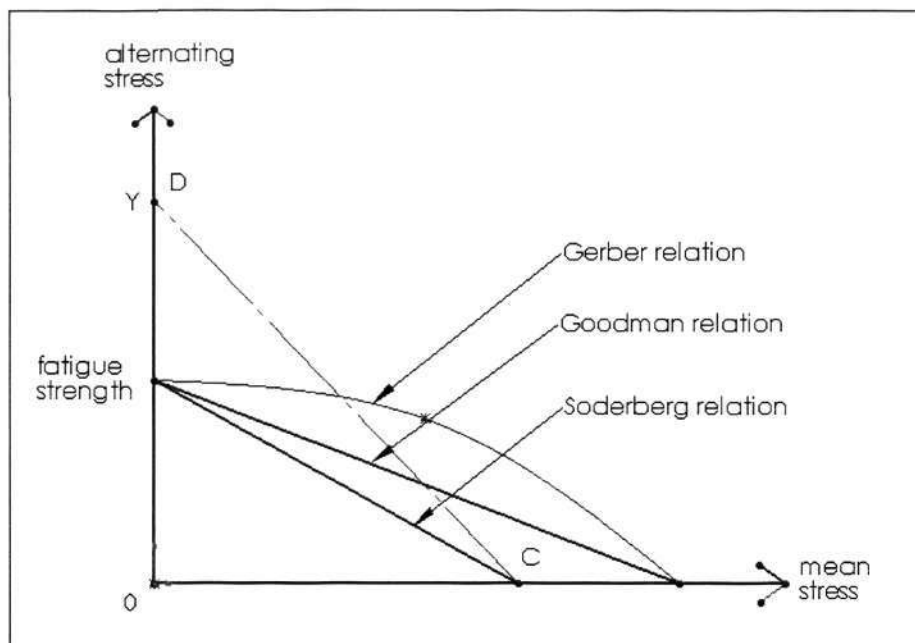


Figure 54: Three relations: Soderberg, Gerber and Goodman

4.4 Chapter summary

This chapter gives an overview of finite element analysis, followed by an introduction to the FE software ANSYS and a standard set of FEM procedures. Various micromechanical flexure types were modeled and used in the finite element analysis. The FEM results obtained for all four micromechanical flexure types are very good, with a maximum percentage deviation from theory of no greater than 4.5%. This gives an indication of very good conformance between the predicted (theoretical) and actual flexure stiffness values. The use of the theoretical flexure stiffness equations in the design of the microactuator switch has been justified via finite element analysis. Structural analysis results obtained indicated very low stress levels for all the micromechanical flexure types at the maximum loading level. This would imply that excellent structural integrity is maintained for the designed micromechanical spring

Chapter 4: Finite Element Analysis of the Microactuator Structure

flexures under the normal operating conditions. Finite element analysis is essential during the design phase of the microactuator switch in order to justify the use of theoretical flexure stiffness equations and to check on the structural integrity of the designed spring flexures under the stipulated loading conditions.

Next, the concept and theory of fatigue is presented and discussed. The three main types of empirical relations to describe the effects of mean stress are listed and discussed. It is possible to carry out fatigue analysis via ANSYS to predict the operating lifespan of the micromechanical flexures under the stipulated loading levels. However, this will not be performed in this research project as the main emphasis is on the design, fabrication and testing of the lateral microactuator switch assembly.

Chapter 5: Mask Design and Microfabrication Process

An assembly model of the microactuator switch is generated using a 3-D CAD software called 'SolidWorks', after the design and analysis has been completed. The proposed fabrication process flow and mask design process will be documented and presented. A well-documented process flow is necessary before actual microfabrication process takes place in order to perform an overall process flow simulation check. The design and fabrication of the masks is a critical part of the entire microfabrication process. The masks will be used for photolithography purpose for the transfer of copies of patterns from the mask onto the surface of a solid material via the use of photo-resist. The complete microfabrication process for the lateral microactuator switch is presented.

5.1 CAD modeling

A CAD model of the entire microactuator switch design is generated using 'SolidWorks'. The CAD model is essential as it is able to provide a simulation check on the design for any possible physical interference. The CAD model also serves as a platform for finite element analysis of critical components within the assembly. Finite element analysis is performed prior to any actual microfabrication and it serves as a tool to justify the designed parameters and theoretical predictions. Finite element analysis is an engineering tool that is used to justify the conformance between theoretical and actual values obtained; and to check on the structural integrity of critical structures in the microactuator switch assembly.

Figure 55 shows a CAD model of the microactuator switch assembly (plan view):

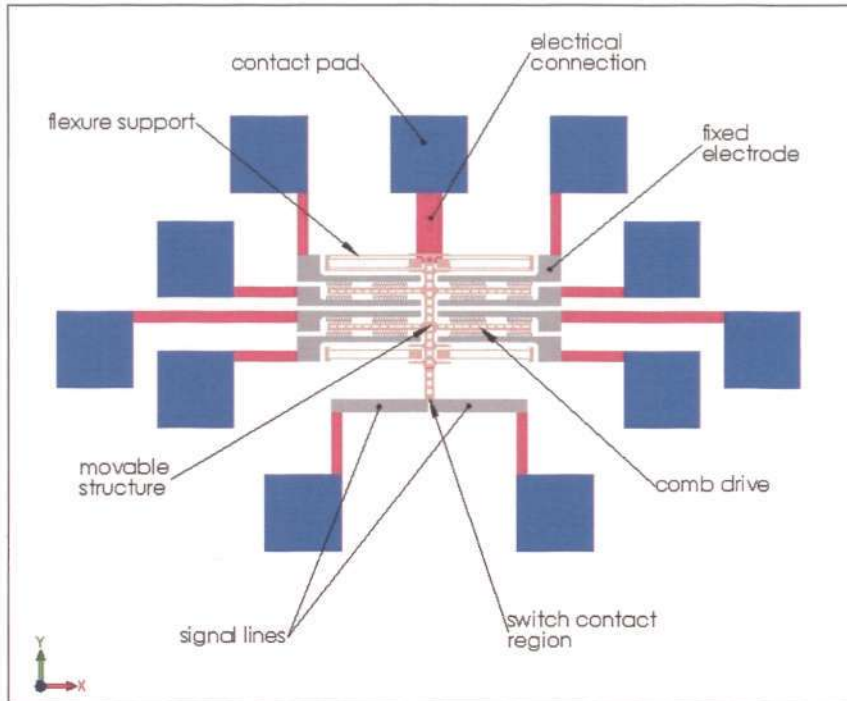


Figure 55: Schematic of the microactuator switch assembly (plan view)

An isometric view of the microactuator switch assembly is shown in Figure 56:

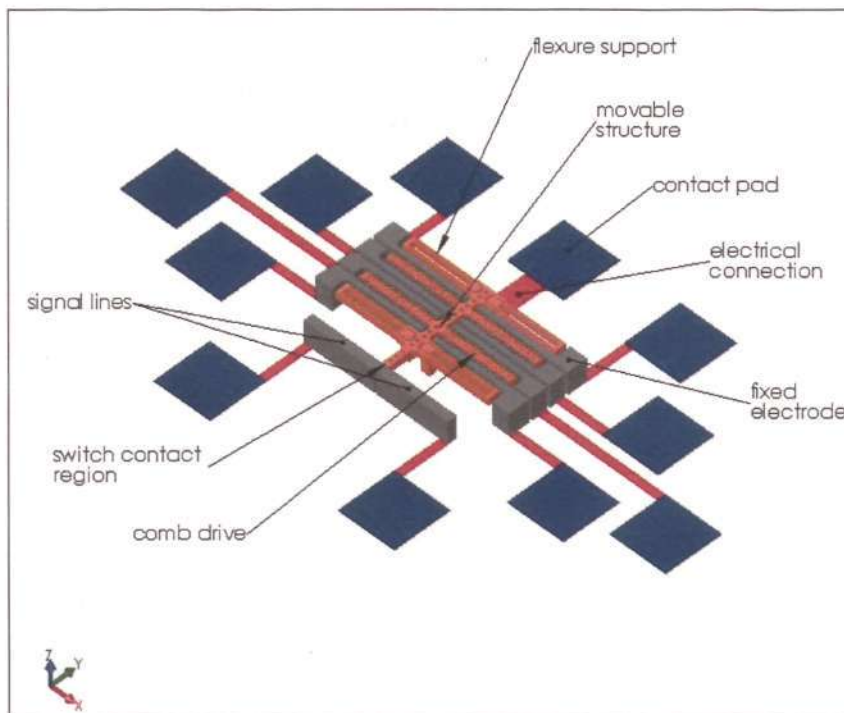


Figure 56: Schematic of the microactuator switch assembly (isometric view)

Chapter 5: Mask Design and Microfabrication Process

Each microactuator switch assembly resides within a cell on the wafer surface. Each cell will contain an independent microactuator switch assembly. The total number of cells to be arranged on the wafer surface area has to be optimized for better efficiency and productivity. An overview of the microactuator switch assembly at the wafer level (only one microactuator switch assembly is shown for illustration purpose) is as shown in the following figures:

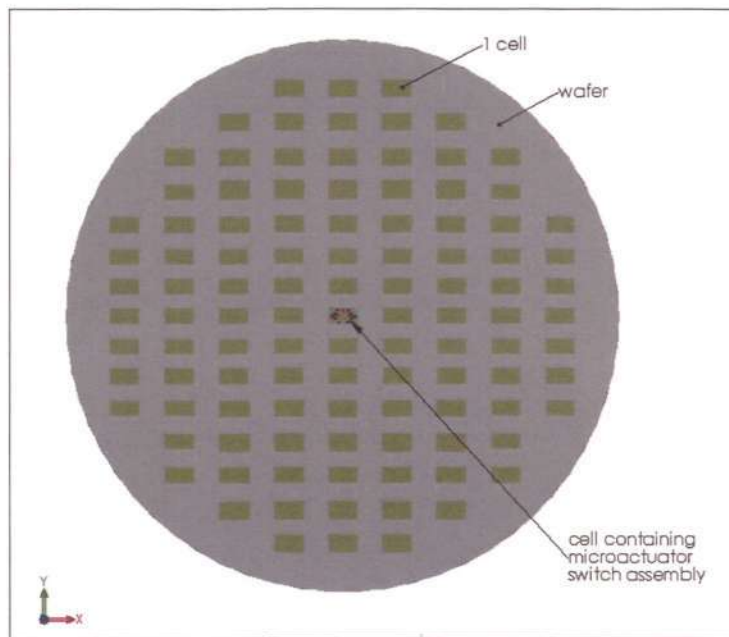


Figure 57: Overview of microactuator switch assembly (wafer level)

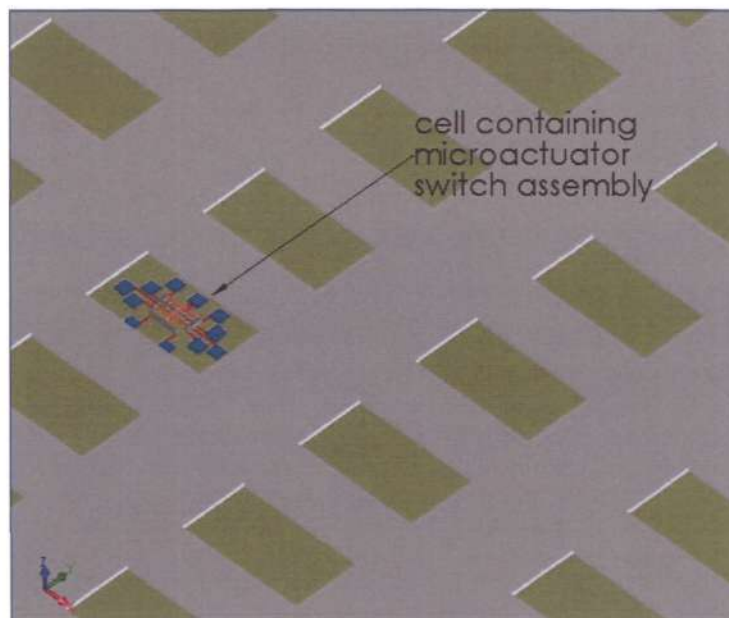


Figure 58: Isometric view of microactuator switch assembly (wafer level)

5.2 Proposed fabrication process flow

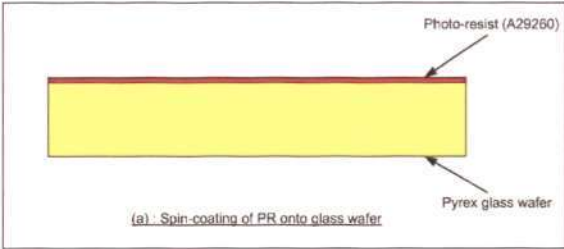
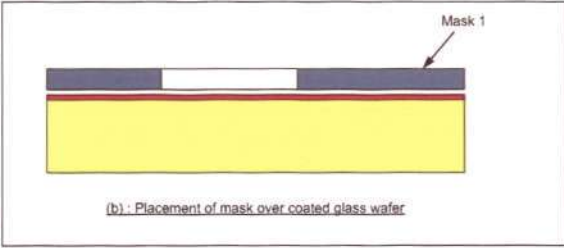
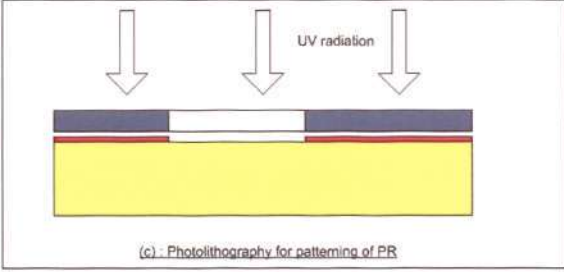
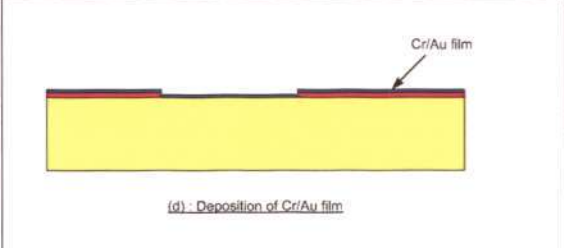
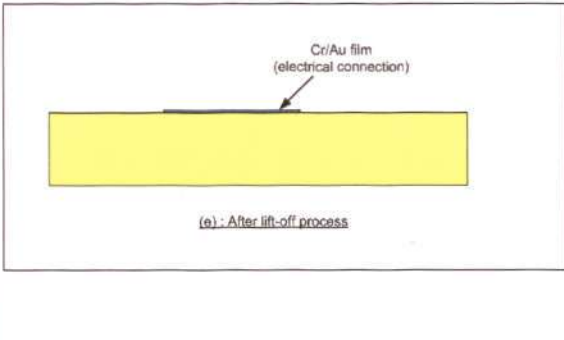
The designed microactuator switch has a large thickness structure. Hence, fabrication is done using bulk silicon (via bulk micromachining) instead of using SOI wafers. To achieve the prototype of the microactuator switch, a range of MEMS microfabrication techniques would need to be employed. The adopted techniques consist of photolithography, sputter deposition, lift-off process, DRIE and wafer bonding process.

The microactuator switch assembly consists of two main components, namely the silicon wafer and the glass wafer, bonded together via the wafer bonding process. Electrical routing, contact pads and connections are fabricated onto the glass substrate via the sputtering and lift-off processes; while the features of the comb-drives and support flexures are obtained via DRIE of bulk silicon. The glass wafer will act as a substructure to support the entire microactuator switch assembly, and at the same time provide electrical connections and interfaces.

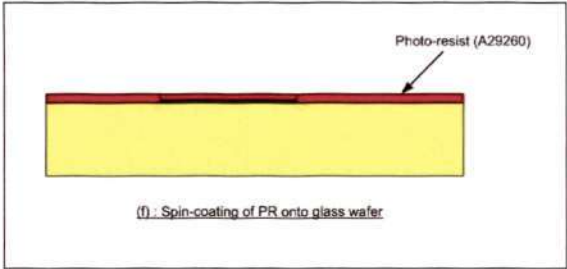
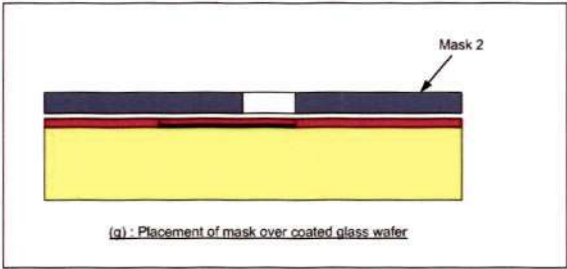
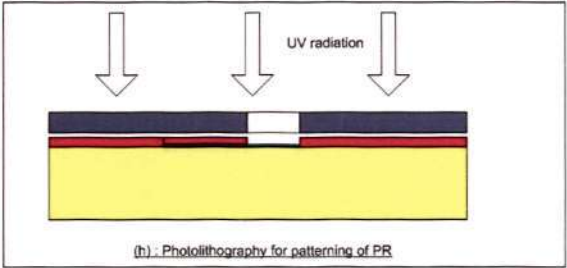
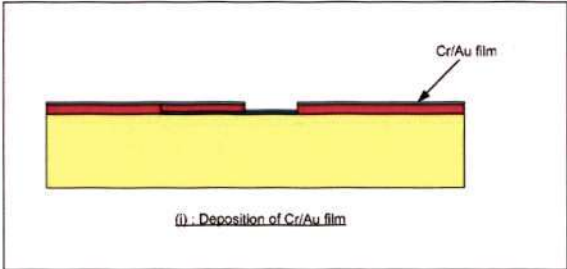
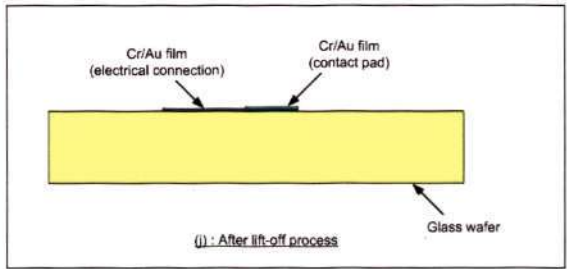
The detailed proposed process flow for the entire microfabrication of the microactuator switch is documented and presented accordingly in the Appendix section.

The overall proposed process flow is summarized sequentially in the series of schematics in Table 9 as follows (Note: The support wafers are not shown in the schematic diagrams):

Table 9: Summary of microfabrication process flow for microactuator switch

Schematic process diagram	Description
	<p><u>Process 1 >> Deposition of Cr/Au film (on 700μm-thick Pyrex glass wafer)</u></p>
	<ul style="list-style-type: none"> • Objective: To cater for electrical routing and connections. • Process: Sputter deposition • Wafer: Glass wafer
	<ul style="list-style-type: none"> • Mask: Mask 1 (electrical connection) • Total thickness of the deposited Cr/Au film must not exceed 50nm.
	<ul style="list-style-type: none"> • Thickness of chromium (Cr) film ~ 20nm. • Thickness of gold (Au) film ~ 30nm.
	

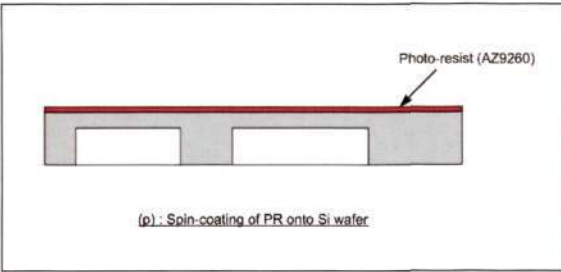
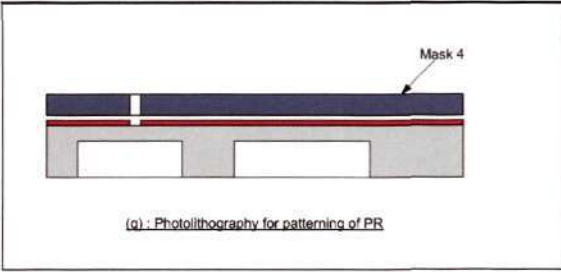
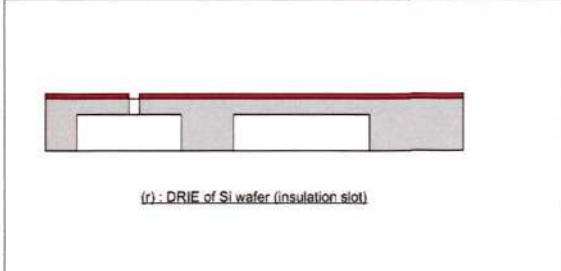
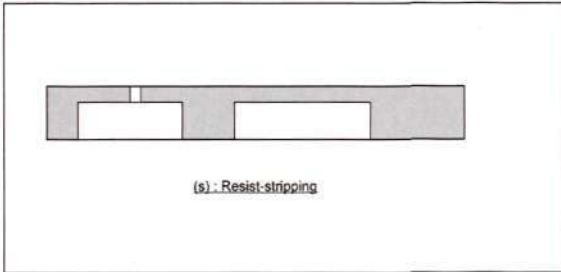
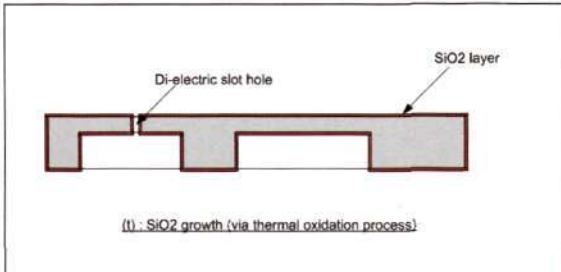
Chapter 5: Mask Design and Microfabrication Process

 <p>(f) : Spin-coating of PR onto glass wafer</p>	<p><u>Process 2 >> Deposition of Cr/Au film (on 700μm-thick Pyrex glass wafer)</u></p>
 <p>(g) : Placement of mask over coated glass wafer</p>	<ul style="list-style-type: none">• Objective: To cater for electrical contact pads.• Process: Sputter deposition• Mask: Mask 2 (contact pad)• Wafer: Glass wafer (from Process 1)
 <p>(h) : Photolithography for patterning of PR</p>	<ul style="list-style-type: none">• Thickness of Cr film \sim 30nm.• Thickness of Au film \sim 0.4μm (or 400nm).
 <p>(i) : Deposition of Cr/Au film</p>	
 <p>(j) : After lift-off process</p>	

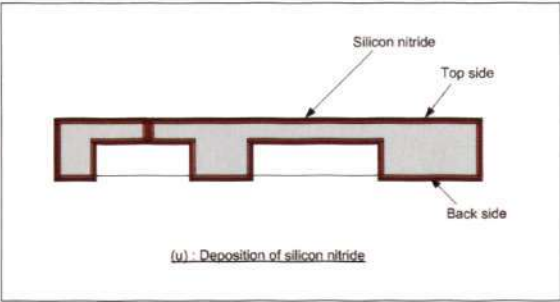
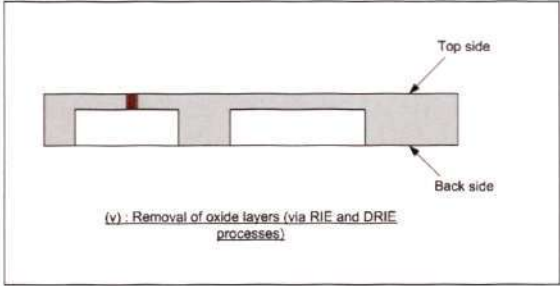
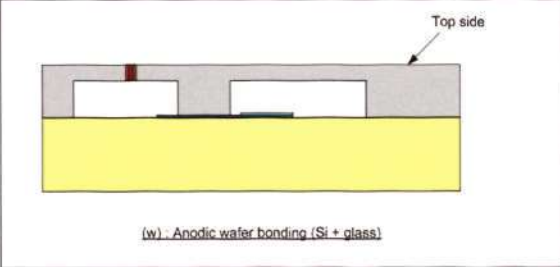
Chapter 5: Mask Design and Microfabrication Process

<p>(k) : Spin-coating of PR onto Si wafer</p>	<p><u>Process 3 >> Back etching of cavities (on 200μm-thick silicon wafer)</u></p>
<p>(l) : Placement of mask over the coated Si wafer</p>	<ul style="list-style-type: none"> • Objective: To etch cavities of a depth of 140μm. • Process: DRIE • Mask: Mask 3 (back etching) • Wafer: Silicon wafer and support wafer
<p>(m) : Photolithography for patterning of PR</p>	
<p>(n) : DRIE of Si wafer (back etching)</p>	
<p>(o) : Resist-stripping and flip-over</p>	

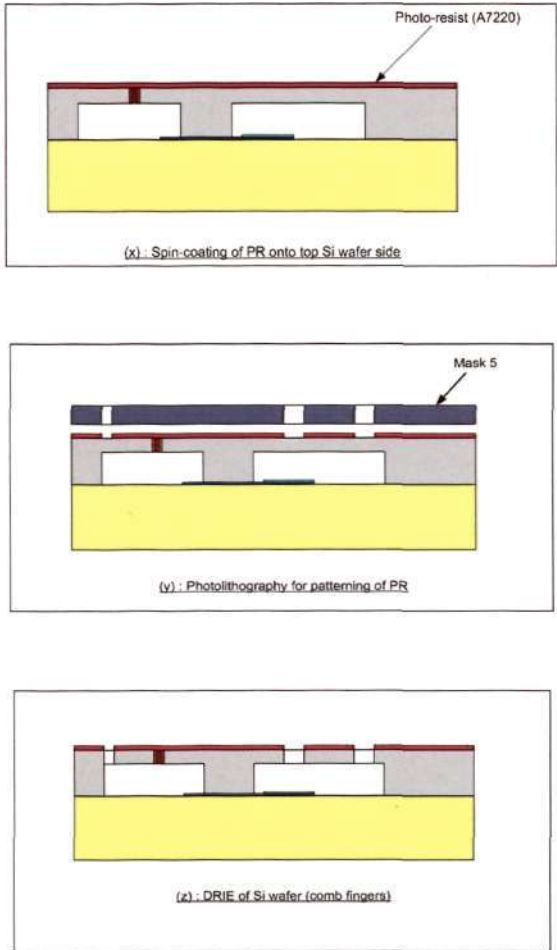
Chapter 5: Mask Design and Microfabrication Process

 <p>(p) : Spin-coating of PR onto Si wafer</p>	<p><u>Process 4 >> Etching of dielectric slot hole (on the 200μm-thick silicon wafer)</u></p>
 <p>(q) : Photolithography for patterning of PR</p>	<ul style="list-style-type: none"> • Objective: To etch dielectric slot holes
 <p>(r) : DRIE of Si wafer (insulation slot)</p>	<ul style="list-style-type: none"> • Process: DRIE
 <p>(s) : Resist-stripping</p>	<ul style="list-style-type: none"> • Mask: Mask 4 (insulation slot)
 <p>(t) : SiO2 growth (via thermal oxidation process)</p>	<ul style="list-style-type: none"> • Wafer: Silicon wafer (from process 3) and support wafer
	<ul style="list-style-type: none"> • Dimension of dielectric slot hole is $(L \times W)\mu\text{m}^2 = (60 \times 3)\mu\text{m}^2$ with a depth of 60μm.

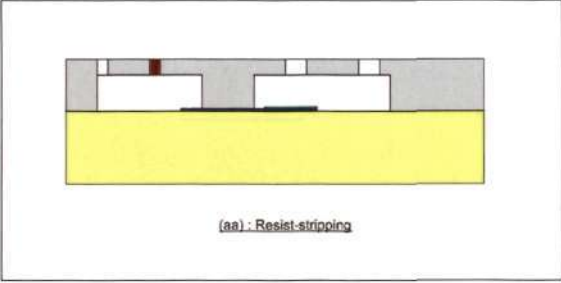
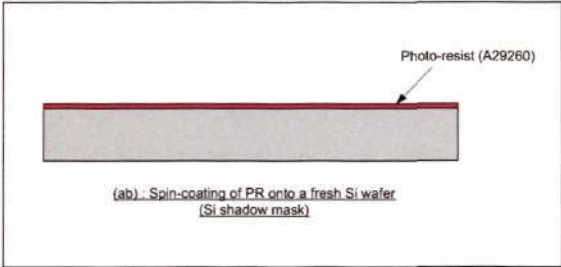
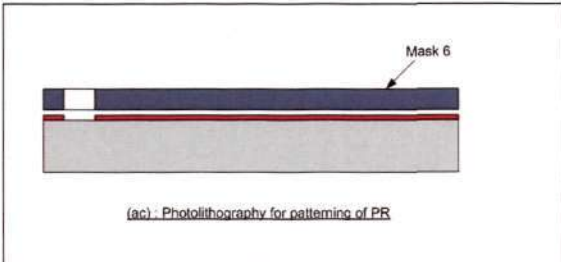
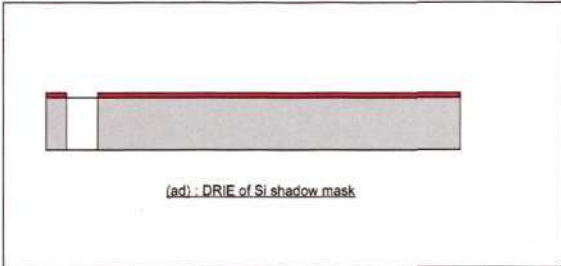
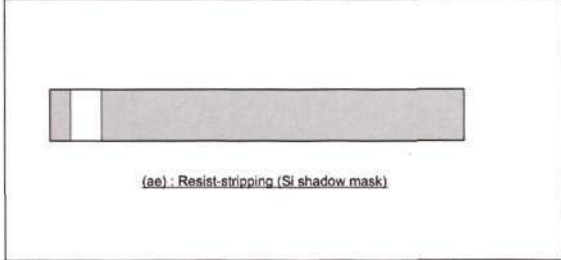
Chapter 5: Mask Design and Microfabrication Process

 <p>(v) - Deposition of silicon nitride</p>  <p>(v) - Removal of oxide layers (via RIE and DRIE processes)</p>	
 <p>(w) - Anodic wafer bonding (Si + glass)</p>	<p><u>Process 5 >> Wafer bonding (between the glass wafer and silicon wafer)</u></p> <ul style="list-style-type: none"> • Objective: To bond the prepared silicon and glass wafers. • Process: Anodic wafer bonding • Wafers: Glass wafer (from process 2) and silicon wafer (from process 4) • Bonding process is performed between sputter-deposited top-side of glass wafer and etched

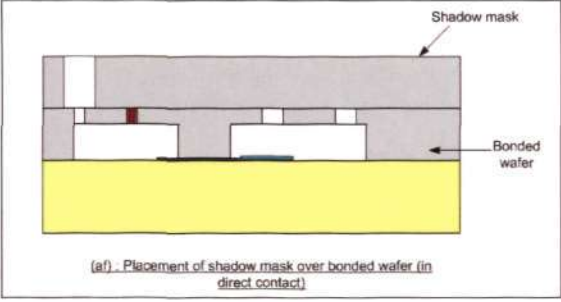
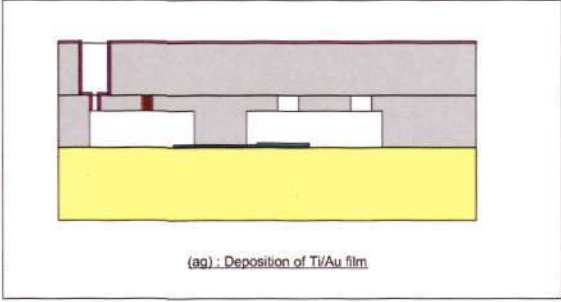
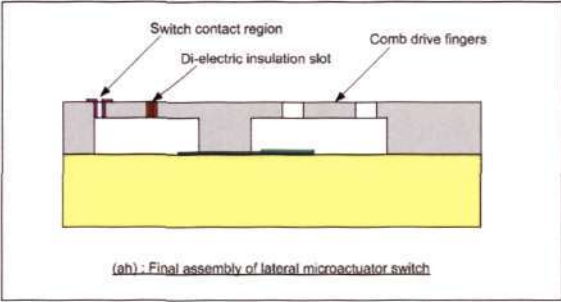
Chapter 5: Mask Design and Microfabrication Process

	<p>backside of silicon wafer.</p> <ul style="list-style-type: none"> • Alignment is needed between the sputtered metal film alignment marks on the glass wafer and the etched-through alignment marks on the silicon wafer. • Anodic bonding process is performed under a voltage of 1000V and a temperature of 363°C.
 <p>(x) Spin-coating of PR onto top Si wafer side</p> <p>(y) Photolithography for patterning of PR</p> <p>(z) DRIE of Si wafer (comb fingers)</p>	<p><u>Process 6 >> Etching of comb-drive finger elements (on the top silicon wafer side of the bonded wafers)</u></p> <ul style="list-style-type: none"> • Objective: To etch both the comb-drive features and flexure supports. • Process: DRIE • Mask: Mask 5 (comb-drive fingers) • Wafer: Bonded silicon-glass wafer (from process 5)

Chapter 5: Mask Design and Microfabrication Process

 <p>(aa) : Resist-stripping</p>	
 <p>Photo-resist (A29260)</p> <p>(ab) : Spin-coating of PR onto a fresh Si wafer (Si shadow mask)</p>	<p><u>Process 7 >> Deposition of Ti/Au film at the switch contact region</u></p> <ul style="list-style-type: none"> • Objective: To deposit conducting metal films at the switch contact region via a shadow mask wafer. • Process: DRIE and Sputter deposition • Mask: Mask 6 (shadow mask opening) • Wafer: Bonded glass-silicon wafer (from process 6) and support wafer • A shadow mask wafer is to be positioned over the bonded wafer at the switch contact region for the purpose of sputter deposition of Ti/Au film.
 <p>Mask 6</p> <p>(ac) : Photolithography for patterning of PR</p>	
 <p>(ad) : DRIE of Si shadow mask</p>	
 <p>(ae) : Resist-stripping (Si shadow mask)</p>	

Chapter 5: Mask Design and Microfabrication Process

 <p>(af) : Placement of shadow mask over bonded wafer (in direct contact)</p>	<ul style="list-style-type: none"> • Thickness of titanium (Ti) film = 50nm • Thickness of gold (Au) film = 0.5μm (or 500nm) • Dimension of through opening on the shadow mask = (300x200)μm²
 <p>(ag) : Deposition of Ti/Au film</p>	
 <p>(ah) : Final assembly of lateral microactuator switch</p>	

5.3 Mask design

Once the structure and the corresponding microfabrication processes have been determined, the next step is to design the required masks. The design and fabrication of masks is very critical since the photolithography process will transfer copies of pattern from the mask directly onto the surface of a solid material via a photoresist. Based on the proposed microfabrication process flow, a total of 6 layers of masks have been designed using the mask layout design software called 'L-Edit'.

Chapter 5: Mask Design and Microfabrication Process

The microactuator switch comprises of two wafers, silicon and glass; with double-side patterning required for the silicon wafer. A total of six masks (one mask for shadow mask) are required as described:

- Mask 1 >> For the electrical connections on glass substrate
- Mask 2 >> For the electrical contact pads on glass substrate
- Mask 3 >> For backside etching of silicon wafer
- Mask 4 >> For etching of insulation slot holes
- Mask 5 >> For etching of comb finger features and flexure supports
- Mask 6 >> For etching of through opening holes for shadow mask

The following figures show the various mask layers.

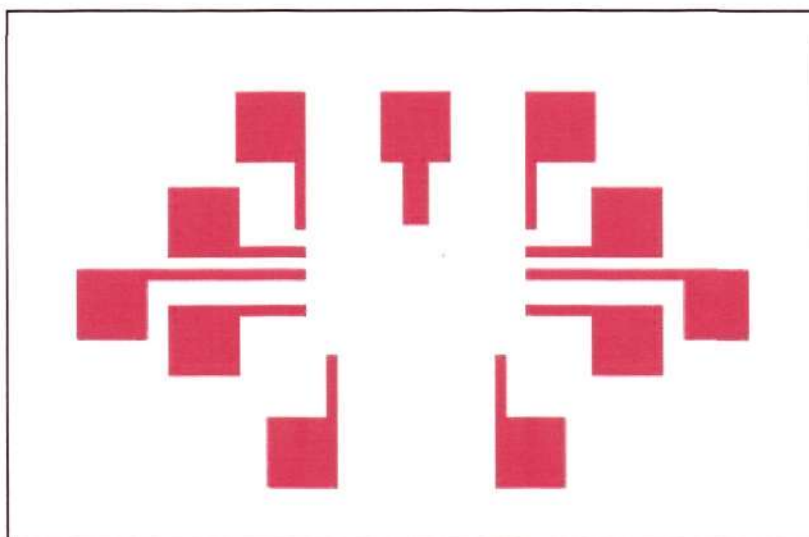


Figure 59: Mask 1 (electrical connection)

Chapter 5: Mask Design and Microfabrication Process

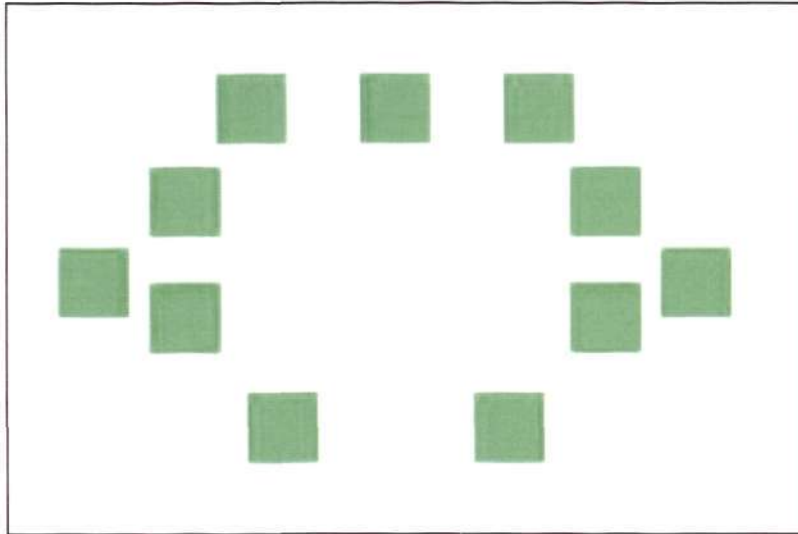


Figure 60: Mask 2 (electrical contact pads)

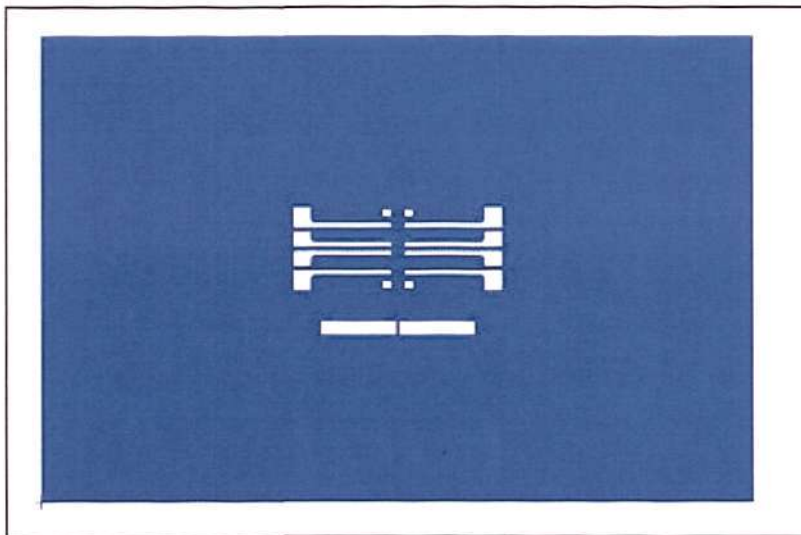


Figure 61: Mask 3 (backside etching)

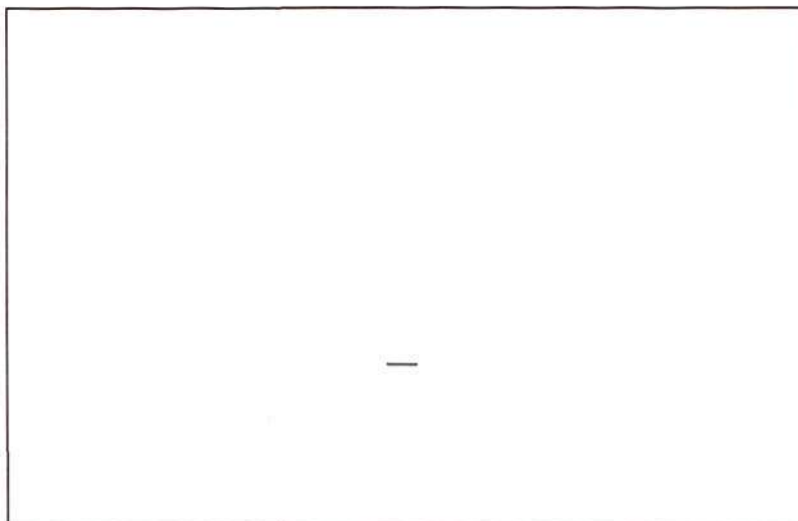


Figure 62: Mask 4: Insulation slot

Chapter 5: Mask Design and Microfabrication Process



Figure 63: Mask 5 (comb finger features)

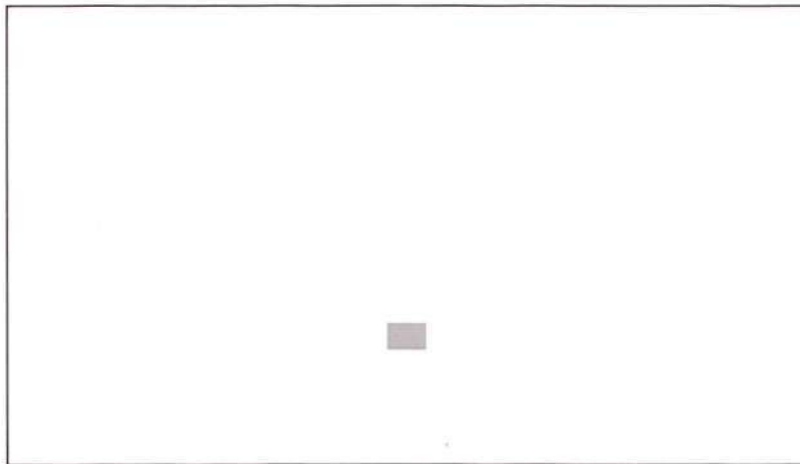


Figure 64: Mask 6 (shadow mask opening)

Figure 65 shows the schematic of all 6 masks superimposed:

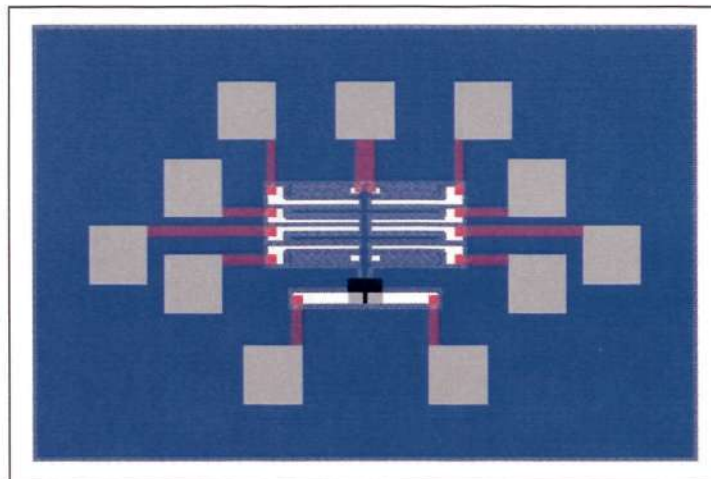


Figure 65: Schematic of all masks superimposed

Chapter 5: Mask Design and Microfabrication Process

An overview of the layout of all masks is as shown:

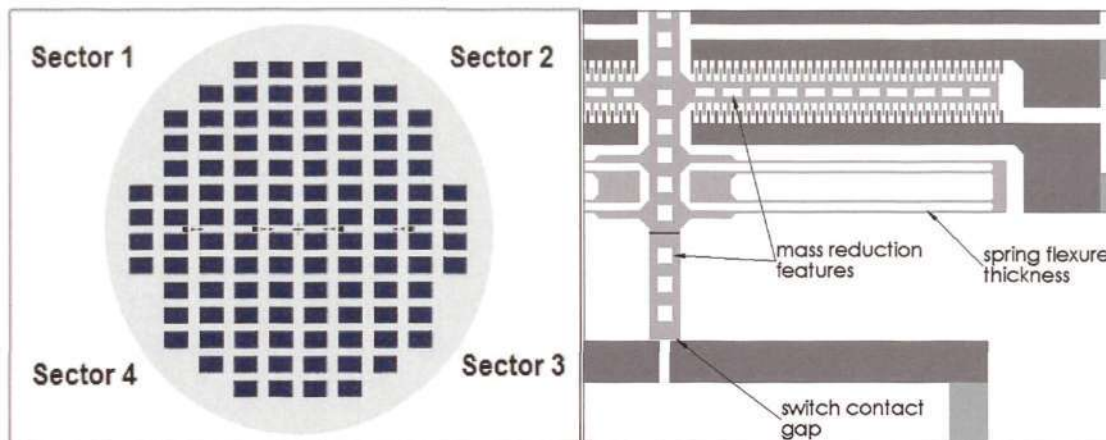


Figure 66: Overview of the layout of all masks

Figure 66 shows the whole set of masks that have been designed for the photolithography steps in the microfabrication process of the microactuator switch. There are many cells of the microactuator switch neatly arrayed in the mask layout, and each cell will fabricate a prototype of the microactuator switch. Since there are several mask layers involved in the microfabrication process, the alignment process is crucial. The alignment marks on each respective mask layer are required for the accurate alignment of features between the silicon and glass wafers. The designed alignment marks are distributed symmetrically in each mask layer.

With reference to Figure 66, the overall mask layout is divided into four sectors, with each sector consisting of the same design but with a modified design parameter as follows:

- Sector 1 >> Original theoretical design (switch contact gap = $3\mu\text{m}$; spring flexure thickness = $5\mu\text{m}$ and without mass reduction features)
- Sector 2 >> Switch contact gap is increased to $4\mu\text{m}$
- Sector 3 >> Thickness of spring flexure is increased to $6\mu\text{m}$.

Chapter 5: Mask Design and Microfabrication Process

- Sector 4 >> Original theoretical design (with mass reduction features as shown in Figure 66)

5.4 Fabrication process and results

Actual microfabrication was carried out after the detailed process flow has been generated, and the designed masks being fabricated. Fabrication pictures are presented for each process discussed earlier on.

Processes 1 and 2: Deposition of Cr/Au film (on a 700 μ m-thick Pyrex glass wafer)

The sputtered alignment marks are as shown in the following pictures:

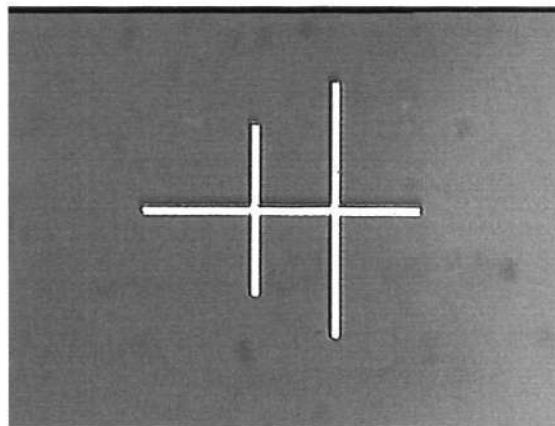


Figure 67: Sputtered alignment marks I (on glass substrate)

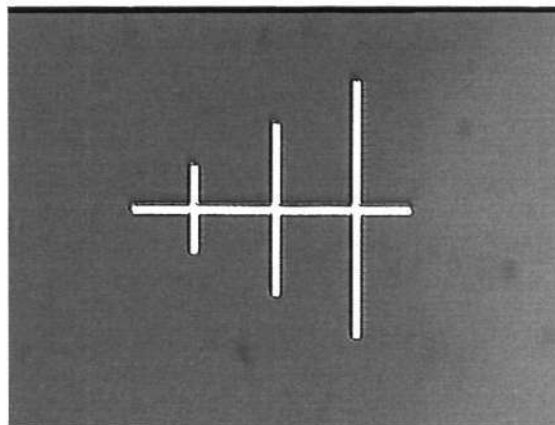


Figure 68: Sputtered alignment marks II (on glass substrate)

Chapter 5: Mask Design and Microfabrication Process

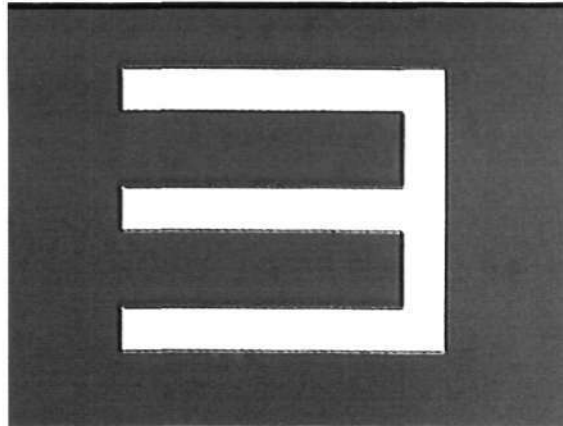


Figure 69: Sputtered alignment marks III (on glass substrate)

The final sputtered Cr/Au thin films (after completing process 2) are as shown:

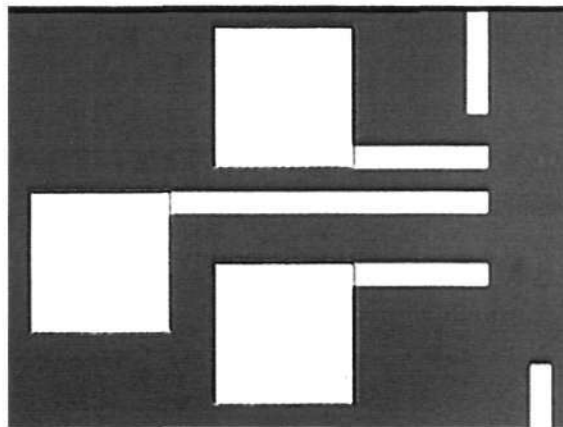


Figure 70: Sputtered Cr/Au electrode contacts I (on glass substrate)

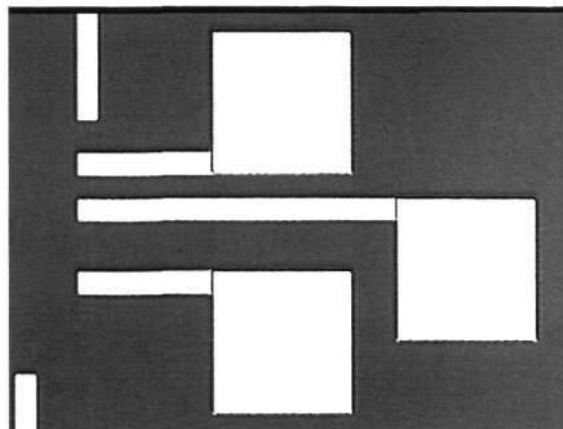


Figure 71: Sputtered Cr/Au electrode contacts II (on glass substrate)

Chapter 5: Mask Design and Microfabrication Process

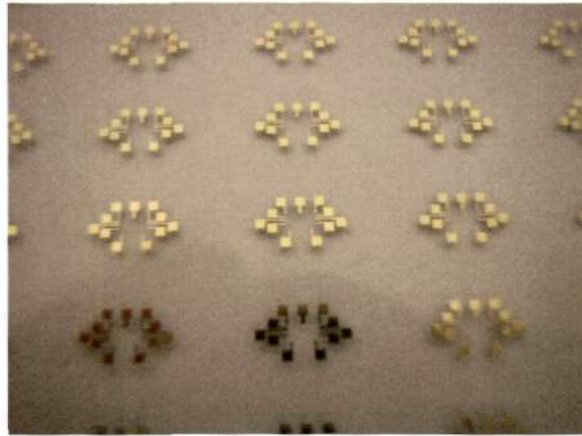


Figure 72: Sputtered Cr/Au electrode contacts III (on glass substrate)

Process 3: Back etching of cavities (on 200 μ m-thick silicon wafer)

Figure 73 shows a picture of one of the alignment marks after back etching:

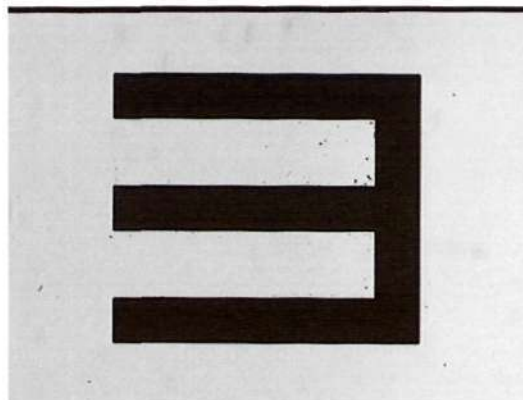


Figure 73: Alignment mark after back etching (on silicon wafer)

The following picture shows the patterned photo-resist for the back etching process:

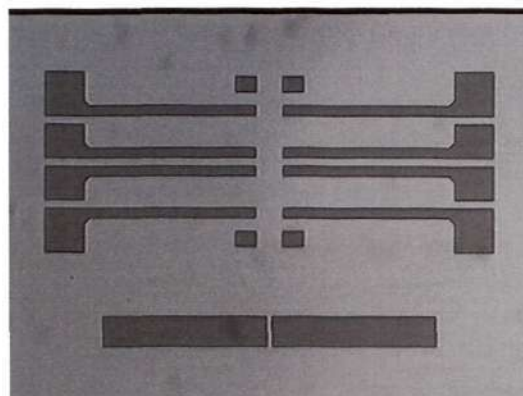


Figure 74: Photo-resist patterning for back etching (on silicon wafer)

Chapter 5: Mask Design and Microfabrication Process

The following figures show the silicon substrate after back etching process:



Figure 75: Structures formed after back etching (on silicon wafer)

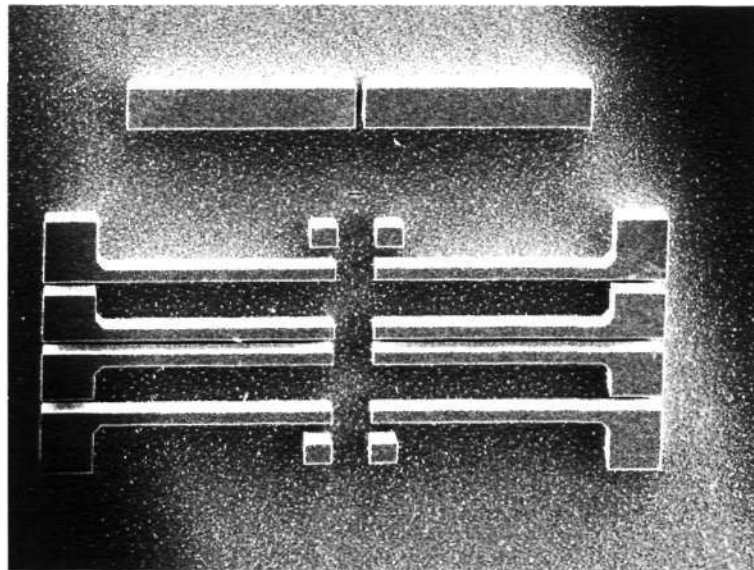


Figure 76: SEM photo of structures formed after back etching (on silicon wafer)

Process 4: Etching of dielectric slot hole (on the 200 μm -thick silicon wafer)

After back etching process of the silicon wafer has been performed, the through dielectric slot holes are obtained via DRIE process on the top-side of the silicon wafer.

Figure 77 shows the dielectric through slot hole after DRIE from the top-side of the silicon wafer:

Chapter 5: Mask Design and Microfabrication Process

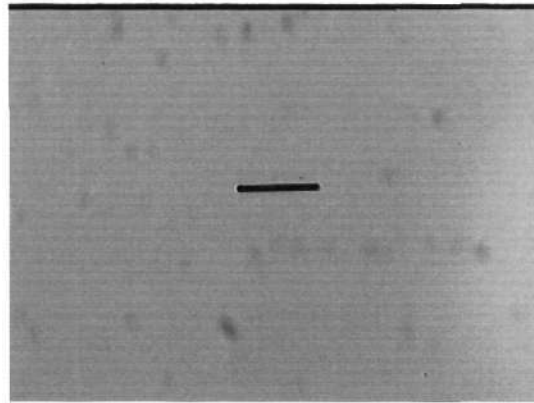


Figure 77: Dielectric slot hole (view from top-side of silicon wafer)

The following picture shows the dielectric slot hole from the backside of the silicon wafer:

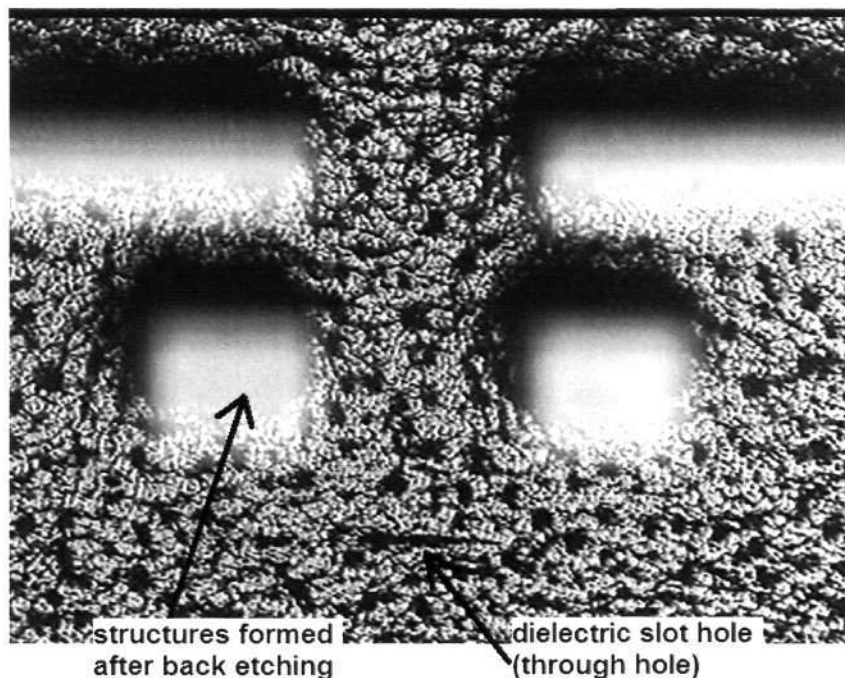


Figure 78: Dielectric slot hole (view from backside of silicon wafer)

The next procedure after DRIE process of the dielectric slot hole is to grow a layer of silicon oxide (SiO_2) via thermal oxidation process, followed by silicon nitride (Si_3N_4) deposition via LPCVD. Pictorials of the silicon wafer after SiO_2 growth and Si_3N_4 deposition are shown:

Chapter 5: Mask Design and Microfabrication Process

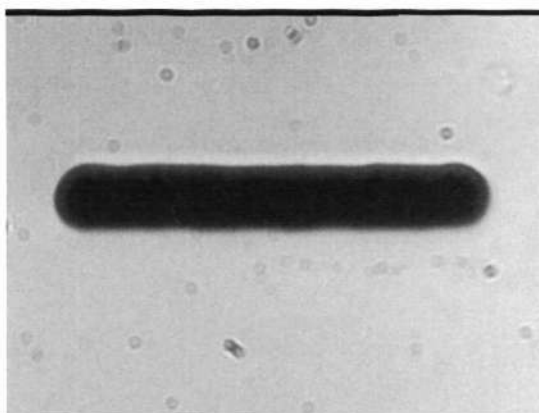


Figure 79: Dielectric slot hole after SiO₂ growth and Si₃N₄ deposition (top-side view)

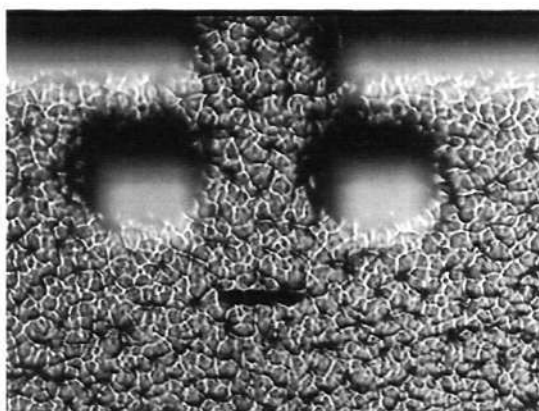


Figure 80: Dielectric slot hole after SiO₂ growth and Si₃N₄ deposition (backside view)

Processes 5 and 6: Anodic wafer bonding and etching of comb-drive finger and flexure features

The surface oxide and nitride layers need to be completely removed before anodic wafer bonding takes place. The removal of surface oxides and nitrides is via RIE and DRIE processes. After this, anodic wafer bonding is performed, followed by a final DRIE process on the topside of the silicon wafer to obtain both the comb finger and spring flexure features.

Figures 81 to 83 show the comb fingers and flexure features after the final DRIE process.

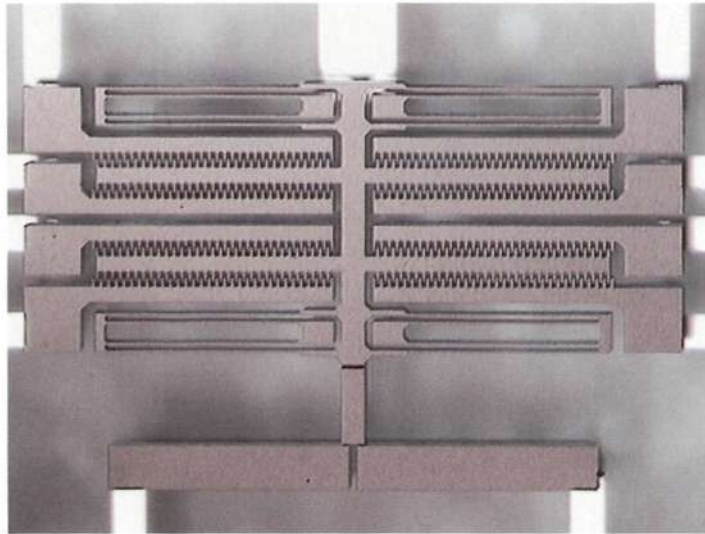


Figure 81: Microactuator switch assembly (after final DRIE)

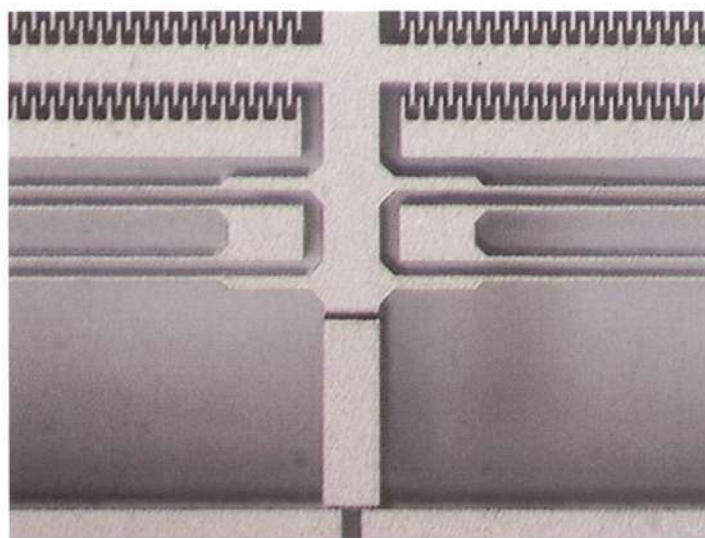


Figure 82: Dielectric slot at the switch contact region

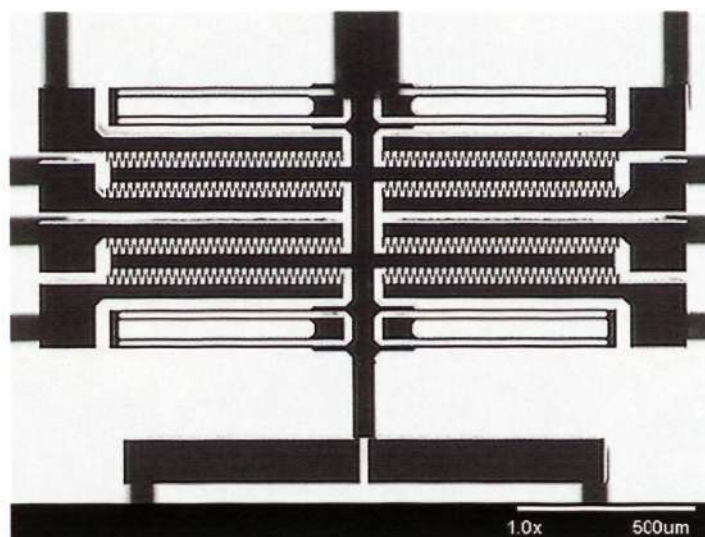


Figure 83: Microactuator switch assembly

Chapter 5: Mask Design and Microfabrication Process

Process 7: Deposition of Ti/Au film at the switch contact region via a shadow mask

A few shadow masks have been fabricated using silicon wafers of thickness of 200 μm . The shadow mask contains neatly arrayed rectangular opening holes to cater for the sputtering of Ti/Au films at the switch contact region. The following picture shows an opening of the shadow mask wafer:

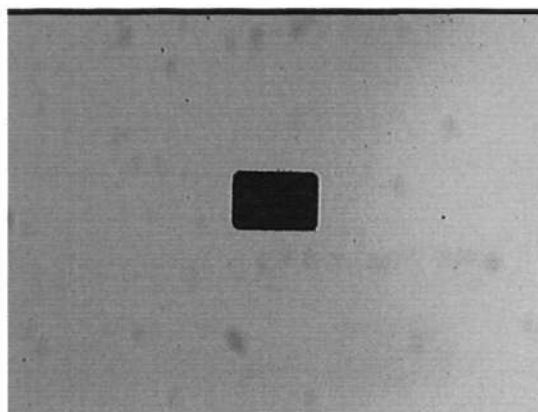


Figure 84: An opening of shadow mask wafer

The shadow mask is placed in contact on top of the fabricated microactuator switch assembly, with the arrayed through openings aligned to the switch contact regions. After the sputtering process of Ti/Au films, the shadow mask is removed; and the microfabrication of the lateral MEMS microactuator switch assembly is completed.

5.5 Chapter summary

The chapter presents the background and the need for CAD modeling to be performed for the proposed microactuator switch design. This is followed by a detailed documentation and description of the microfabrication process flow for the microactuator switch. The issue of mask design has been highlighted and the designed masks for each corresponding process are documented and presented. Finally, pictures

Chapter 5: Mask Design and Microfabrication Process

and SEM photos showing the various phases of the entire microfabrication process are presented and discussed.

Chapter 6: Results and Discussion

This research work has been undertaken for the design and analysis of a lateral MEMS microactuator switch, and has developed a new design of a 3-D electrostatic lateral microactuator switch with a unique dielectric slot feature. The prototypes of the microactuator switch have been successfully fabricated. Functional screening test is performed for all cells of the fabricated wafers containing the microactuator switch units. The functional screening test is carried out to identify the few functional cells, which would be subjected to further characterization testing.

6.1 Test results

The functional cells that have been identified are subjected to a series of tests for the following characteristics:

- Actuation voltage
- Contact resistance
- Switching time
- Switching lifetime

6.1.1 Actuation voltage

The functional microactuator switch units obtained are tested to check the level of actuation voltage required to physically close and open the switch. It is observed that an input square waveform with amplitude of $\pm 60\text{V}$ is required to physically close and open the microactuator switch.

6.1.2 Contact resistance

With the microactuator switch activated at the 'CLOSED' state, the resistance across the signal lines is measured; and is found to be no more than 1.64Ω for all the functional microactuator switch units tested.

6.1.3 Switching time

The microactuator switch is able to function well under an input sinusoidal waveform at a frequency of 3.5kHz with an amplitude of $\pm 60\text{V}$, corresponding to a switching time of $286\mu\text{s}$. Figure 85 shows the input waveform.

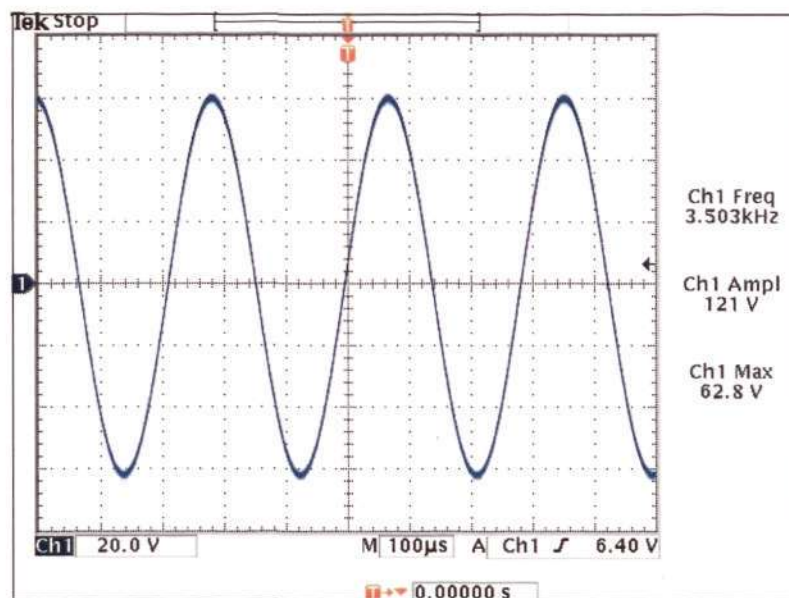


Figure 85: Input sinusoidal waveform

6.1.4 Switching lifetime

Using sputtered gold as the contact material, it has been demonstrated that a contact resistance below 1.64Ω is maintained for up to approximately 3.2 million cycles of continuous switching operation. Failure is observed at the anchor points (bonding interface between silicon and glass) of the micromechanical flexures where de-

lamination occurs. This failure mode is observed for most of the functional cells that are subjected to reliability testing. No sign of significant degradation is observed at the switch contact region for the tested cells at the point of failure. No sign of failure is observed at the dielectric slot region, which is connecting the switch contact section and the main microactuator structure. Figures 86, 87 and 88 show the failure mode encountered during testing.

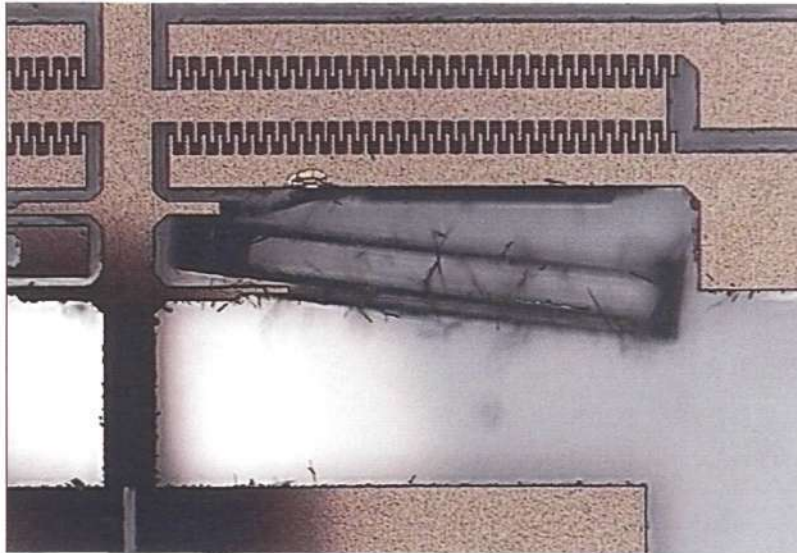


Figure 86: Failure mode I (de-lamination at anchor point of front flexure support)

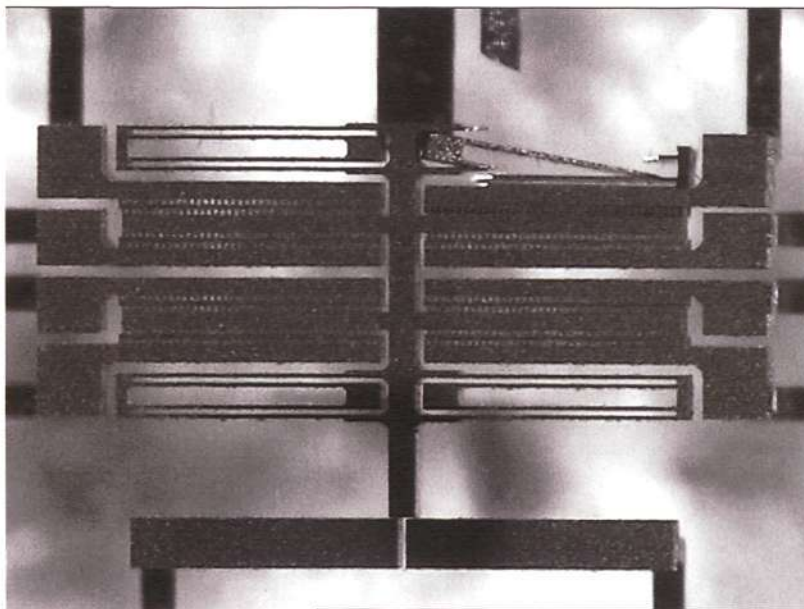


Figure 87: Failure mode II (de-lamination at anchor point of back flexure support)

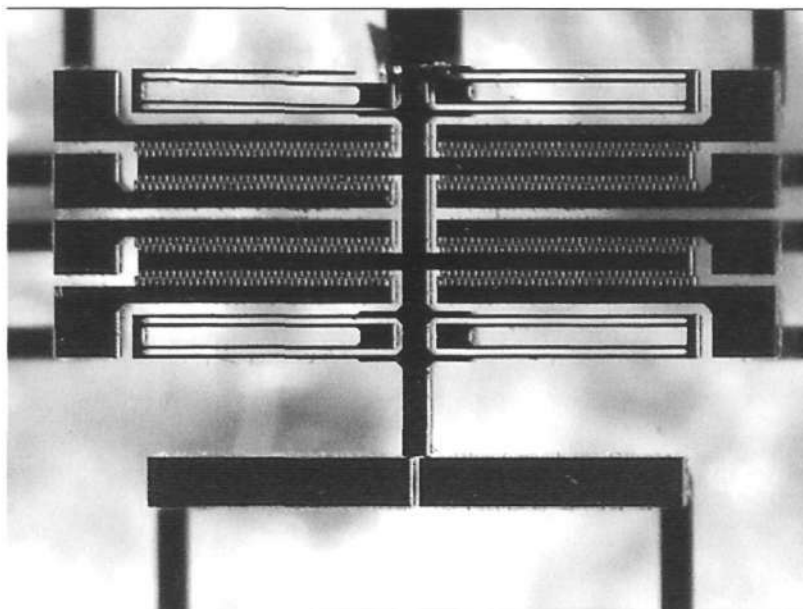


Figure 88: Failure mode III (de-lamination at anchor point of back flexure support)

6.2 Discussion

Table 10 provides a summary of the comparison between the expected values (specifications) and the actual tested values:

Table 10: Comparison between specifications and actual values

Characteristic	Specification	Actual value	Remarks
Actuation voltage (V)	< 80	60	Achieved
Contact resistance (Ω)	< 2	1.64	Achieved
Switching time (μ s)	< 500	286	Achieved
Switching lifetime (continuous number of switching cycles)	> 2×10^6	3.2×10^6	Achieved

For the functional cells obtained in Sector 1 (original theoretical design with switch contact gap = $3\mu\text{m}$ and flexure thickness = $5\mu\text{m}$), the measured actuation voltage that is required to physically close the microactuator switch is 60V. This is in very good conformance to the theoretical design value of 60.8V with a percentage deviation of

only 1.3%. For the tested cells found in Sector 3 (switch gap = $3\mu\text{m}$ and flexure thickness = $6\mu\text{m}$), the actuation voltage required to operate the microactuator switch is found to be at a higher value of 66V. This is in conformance to theory since a higher actuation voltage will be required to overcome the stiffer support flexures in order to operate the microactuator switch with the same switch contact gap. No functional cells can be obtained from Sectors 2 and 4.

Contact resistance is measured using the functional cells in Sector 1. An actuation voltage of 60V is applied and maintained to physically close the switch, and the resistance across the signal lines is measured. The contact resistance measured is no more than 1.64Ω for all the cells tested. The value of contact resistance obtained is relatively low, and this is possibly due to the fact that an additional contact force of $15\mu\text{N}$ has been catered in the design of the microactuator switch. The additional contact force will increase the contact pressure which is advantageous to provide a mechanical abrasion of surface films in order to achieve a low contact resistance. At low applied forces, contact is made only at local asperities hence electrical resistance is high. As greater force is applied, the real contact area increases and contact resistance decreases. Gold is chosen as the contact material because of its low resistivity, good stability and efficiency in RF propagation. Sputtered gold is known to have a higher hardness which gives less surface damage for metallic microcontacts.

The cells from Sector 1 are tested under an input sinusoidal waveform at a frequency of 3.5kHz under an actuation voltage of 60V. This corresponds to a low switching time of $286\mu\text{s}$ (or 0.29ms). Although switch contacts with sputtered gold provide the lowest contact resistance, there is a tendency for 'sticking' or stiction to occur. An

idea to overcome potential stiction problems is to implement designs that stiffen the structures in the direction of motion where stiction is most likely to occur. In the microactuator switch design, a ‘push-pull’ concept has been adopted instead; and the electrostatic force generated by the opposite arrays of comb-drives will assist in the return stroke of the switch (i.e. opening the switch) in addition to the restoring forces from the loaded support flexures. In this way, stiction is much less likely to occur during the normal operation of the microactuator switch at high operating frequencies.

The problem of stiction was prominently encountered in the very first few functional prototypes. That was when the actuation voltage was designed to be at a lower value (as compared to 60V) and with support flexures of lower stiffness in the operating direction. The stiction problem has since been reduced significantly when the design was changed to cater for a larger actuation voltage (i.e. larger push/pull force) and with supporting flexures of higher stiffness values in the operating direction. It is deemed that the higher push/pull force exerted by the reciprocating linear microactuator has greatly aided in the reduction of stiction problems.

Functional testing of prototype samples of the microactuator switch has been carried out in the first few millions of cycles, before failure was first observed. Failure was commonly observed to be at the anchor points (i.e. bonding interface between silicon and glass) of the micromechanical flexures where de-lamination occurs. This failure could be due to the fact that the bonding surfaces were not completely clean, and any particulates or process residuals trapped at the interface could result in the degradation of bonding integrity over time. Another possibility could be due to the combined thickness of both the sputtered adhesive and conductive layers on the glass

substrate. The total combined thickness should be no greater than 50nm, or else the 'step' at the silicon-glass bonding interface will be too pronounced and might affect bonding integrity.

Finite element analysis played a crucial part in the design of the microactuator switch. No sign of failure was observed on the structure of the micromechanical spring flexures during both functional and reliability testing. This would imply excellent structural integrity of the spring flexures under the stipulated loading conditions, as predicted by FEA. The microactuator switch is able to translate a linear distance of $3\mu\text{m}$ to physically close the switch under an actuation voltage of 60V. This is in very good agreement to the theoretical predictions made involving flexure stiffness equations, which have been verified by FEA. Finite element analysis has justified both the use of theoretical equations in the design phase; and also the excellent structural integrity of the spring flexures.

The micromechanical flexures are made of single-crystal silicon; and therefore have excellent mechanical performance, such as high yield strength. No sign of significant degradation was observed at the switch contact region at the point of failure. Stiction was not observed at the switch contact region during the reliability testing up to the point of failure, possibly due to the reciprocating action of the microactuator switch to assist in the return stroke in addition to the relaxation of the loaded micromechanical spring support flexures. No sign of failure is observed for the dielectric slot, indicating very good structural integrity and insulating capability under normal switching operating conditions. The normal functioning of the microactuator switch would imply good insulating capability of the dielectric slot.

Chapter 7: Conclusion and Recommendations

7.1 Conclusion

A novel lateral MEMS microactuator switch has been successfully designed and fabricated via bulk micromachining technique. With the optimized design, the microactuator switch has the advantages of low actuation voltage, high reliability, good structural integrity and low switching time. The microactuator switch is designed primarily for high reliability and good functionality. With the ‘push-pull’ configuration, failure by ‘sticking’ phenomenon at the switch contact region is deemed to be reduced. The unique design of the dielectric slot filled with silicon oxide and silicon nitride layers is able to structurally connect the two separate regions of the translating structure and switch contact section during functional testing. Finite element analysis has been employed to justify the use of theoretical flexure stiffness equations and check on the structural integrity of the designed spring flexures. No failure was observed for the designed micromechanical flexures during testing. The phenomenon of stiction was not observed at the switch contact region up to the point of failure during reliability testing.

Failure was observed at the anchor points of the micromechanical flexures at the silicon-glass bonding interface during functional testing. With sputtered gold as the contact material, the measured contact resistance is below 1.64Ω . The microactuator switch can work well under an input square waveform at a frequency of 3.5kHz, up to approximately 3.2 million cycles of continuous switching operation. This corresponds to a switching time of 0.29ms under an actuation voltage of 60V. This would justify

the insulating capability of the dielectric slot for switching operations. The structural integrity and bonding capability of the dielectric slot are found to be very good as it can structurally ‘bond’ two physically separate sections together even after reliability testing.

7.2 Recommendations

Some recommendations for future research work are as follows:

- Improvement in the microfabrication process

The processing of both the glass and silicon wafers in preparation for anodic wafer bonding process should be carried out with great care for process cleanliness. It is critical for the surfaces (to be anodically bonded together) to be extremely clean and free of any particulates or process residuals, which will result in the degradation of bonding integrity.

- Fatigue analysis of the micromechanical flexure supports

The micromechanical flexure supports is a critical component in the microactuator switch assembly. It is essential to perform a fatigue analysis on the flexure support design prior to microfabrication process in order to predict the operational lifetime of the support flexures under the stipulated loading stress levels.

- Exploration of better microfabrication processes

The critical processes such as DRIE and anodic wafer bonding processes should be investigated and improved. At present, anodic bonding is used for the wafer bonding process. If possible, a better bonding technology that produces greater bonding intensity and uniformity should be explored and evaluated. Parameters of the equipment performing DRIE can also be investigated and optimized in order to improve uniformity of the etched areas on the wafer.

References

- [1] Kaigham J. Gabriel, **Microelectromechanical Systems (MEMS)**, Electrical and Computer Engineering and the Robotics Institute, Carnegie Mellon University.
- [2] Nadim Maluf, **An introduction to microelectromechanical systems engineering**, Artech House, Boston London, 2000.
- [3] Joachim, Oberhammer; **Novel RF MEMS Switch and Packaging Concepts**, Microsystem technology, Department of signals, sensors and systems, Royal Institute of Technology, Stockholm, Sweden.
- [4] Howe, R.T.; Muller, R.S.; Gabriel, K.J.; Trimmer, W.S.N., **Silicon micromechanics: sensors and actuators on a chip**, IEEE Spectrum, Volume 27 Issue 7, July 1990.
- [5] Hiroyuki Fujita, **Microactuators and micromachines**, Proceedings of the IEEE, Volume: 86 Issue 8, Aug. 1998, p. 1721-1732.
- [6] Harvey S. Newman, **RF MEMS Switches and Applications**, Naval Research Laboratory, Washington DC.
- [7] Mohammad N. Mollah and Nemai C. Karmakar, **RF MEMS Switches: Paradigms of microwave switching**, School of Electrical and Electronic Engineering, Nanyang Technological University, Singapore.
- [8] Gabriel M. Rebeiz and Jeremy B. Muldavin, **RF MEMS Switches and Switch Circuits**, University of Michigan, Michigan, USA.
- [9] Chuck Goldsmith; Jennifer Kleber; Brandon Pillans; Dave Forehand; Andrew Malczewski and Paul Frueh, **RF MEMS: Benefits and Challenges of an Evolving RF Switch technology**, Raytheon Company.
-

- [10] Wood, D.; Burdess, J.S.; Harris, A.J., **Actuators and their mechanisms in microengineering**, Engineering Science and Education Journal, Volume 7 Issue 1, Feb. 1998, p.19-27.
- [11] Hidenori Ishihara; Fumihito Arai and Toshio Fukuda, **Micro Mechatronics and micro actuators**, Mechatronics, IEEE/ASME Transactions on, Volume 1, No 1, March 1996, p.68-78.
- [12] Trimmer WSN; Gabriel KJ; Mahadevan R., **Silicon electrostatic motors**, in Transactions of the '87: Fourth International Conference on Solid-State Sensors and Actuators, 1987, p.857±60.
- [13] K.S.J. Pister et al., **A planar air levitated electrostatic actuator system**, in Proc. IEEE Micro Electro Mech. Syst. (MEMS'92), 1992, p.190-195.
- [14] Wagner B; Kreutzer M and Benecke W., **Linear and rotational magnetic micromotors fabricated using silicon technology**, in Proceedings of the IEEE Micro Electro mechanical Systems, TravemuE nde, Germany, 1992, p.174-192.
- [15] T. Fukuda et al., **Design and experiments of micro mobile robot using electromagnetic actuator**, in Proc. Third IEEE int. Symp. Micro machine, Human Sci. (MHS'92) , 1992, p.77-81.
- [16] BoE hm S., Olthius W., Bergveld P., **An electrochemically actuated micropump for the use in a 'push-pull' microdialysis based in-vivo monitoring system**, in Proceedings of the Transducer '99: Tenth International Conference on Solid-State Sensors and Actuators, Sendai, Japan, 1999, p.879-881.
- [17] Van de Pol FCM; Van Lintel HTG; Elwenspoek M and Fluitman JHJ, **A thermopneumatic micropump based on micro-engineering techniques**, Sensors and Actuators, 1990, p.198-202.
-

[18] Robbins WP; Polla DL; Tamagawa T and Glumac DE., **Design of linear-motion microactuators using piezoelectric thin films**, J. Micromech Microeng, Volume 1 No 4, Decenber 1991, p.247-252.

[19] Que L; Park J-S; Gianchandani Y.B., **Bent-beam electro-thermal actuators for high force applications**, I proceedings of IEEE micro electro mechanical systems, Orlando, USA, 1999, p.31-36.

[20] Reynaerts D; Peirs J and Van Brussel H., **An implantable drug-delivery system based on shape memory alloy micro-actuation**, Sensors and Actuators, Volume 61, Issues 1-3, June 1997, p.455-462.

[21] Hom C.L.and Shankar, N., **A dynamics model for nonlinear electrostrictive actuators**, Ultrasonics, Ferroelectrics and Frequency Control, IEEE Transactions on, Volume 45, Issue 2, March 1998, p.409-420.

[22] Quandt E. and Seemann K., **Fabrication and simulation of magnetostrictive thin-film actuators**, Sensors and Actuators, Volume 50, Issues 1-2, August 1995, p.105-109.

[23] Benecke W., **Silicon microactuators: activation mechanisms and scaling problems**, in Transducers '91: Sixth International Conference on Solid-State Sensors and Actuators, 1991, p.46-50.

[24] Marc Madou, **Fundamentals of microfabrication**, CRC Press, 1997.

[25] Kellar, C.G. and Howe, R.T., **Hexsil Bimorphs for Vertical Actuation**, Solid-State Sensors and Actuators, 1995 and Eurosensors IX, Transducers '95, The 8th International Conference on, Volume 1, p.9-102.

[26] Takimoto, S.; Kondo, R.; Suzuki, K. and Sugiyama, S., **Fabrication of micromotors using LIGA process**, Micromechatronics and Human Science, MHS '99, Proceedings of 1999 International Symposium on, 1999, p.221-226.

- [27] Gregory T.A. Kovacs; Nadim I. Maluf and Kurt E. Petersen, **Bulk micromachining of silicon**, Proceedings of IEEE, Volume 86, Issue8, August 1998, p.1536-1551.
- [28] Mehra, A.; Ayon, A.A.; Waitz, I.A. and Schmidt, M.A., **Microfabrication of high-temperature silicon devices using wafer bonding and deep reactive ion etching**, Microelectromechanical Systems, Journal of, Volume 8, Issue 2, June 1999, P.152-160.
- [29] Klaassen, E.H.; Petersen, K.; Noworolski, J.M.; Logan, J.; Maluf, N.I.; Brown, J. and Storment, C., **Silicon Fusion Bonding and Deep Reactive Ion Etching a New Technology for Microstructures**, Solid-State Sensors and Actuators, 1995 and Eurosensors IX., Transducers '95, The 8th International Conference on, Volume 1, p.556-559.
- [30] Howe, R.T. and R.S. Muller, **Polycrystalline silicon micromechanical beams**, J. Electrochem. Soc., 1983, p.1420-1423.
- [31] Gobet J.; Cardot F.; Bergqvist J. and Rudolf F., **Electrodeposition of 3D microstructures on silicon**, J. Micromech. Microeng., 3 No 3, September 1993, p.123-130.
- [32] Menz W., **LIGA and related technologies for industrial applications**, in *Transducers '95: The 8th International Conference on Solid-State Sensors and Actuators*, Stockholm, Sweden, 1995, p. 55-55.
- [33] Keller, C.G. and Howe, R.T.; **Hexsil Bimorphs For Vertical Actuation**, Solid-State Sensors and Actuators, 1995 and Eurosensors IX. Transducers '95, The 8th International Conference on, Volume 1, p. 99 -102.
- [34] ---, **Micromechanical membrane switches on silicon**, IBM Journal of Research and Development, vol. 23, no. 4, p.376-385, July 1979.
-

- [35] L.E. Larson, R.H. Hackett and R.F. Lohr, **Microactuators for GaAs-based microwave integrated circuits**, in Proc. Transducers 1991, San Francisco, USA, June 24-27, 1991, p.743-746.
- [36] H.A.C. Tilmans; W. De Raedt and E. Beyne, **MEMS for wireless communications : from RF-MEMS components to RF-MEMS-SiP**, Journal of Micromechanics and Microengineering, vol. 13, no. 4, p. S139-S163, July 2003.
- [37] “**International technology roadmap for semiconductors itrs 2003**”, available at <http://public.itrs.net/>, Tech. Rep., 2003.
- [38] J. Yao, **RF MEMS from a device perspective**, Journal of micromechanics and microengineering, vol. 10, p. R9-R38, 2000.
- [39] G. M. Rebeiz, **RF MEMS Theory, Design and Technology**, 1st ed. Hoboken, New Jersey: Wiley, 2003.
- [40] Tang and William Chi-Keung, **Electrostatic comb drive for resonant sensor and actuator applications**, Thesis (Ph.D.)--University of California at Berkeley, 1990, Ann Arbor, Mich.: UMI, 1990.
- [41] Tang, W.C.; Nguyen, T.-C.H. and Howe, R.T.; **Laterally driven polysilicon resonant microstructures**, **Micro Electro Mechanical Systems**, 1989, Proceedings, An Investigation of Micro Structures, Sensors, Actuators, Machines and Robots, IEEE, 1989, p. 53 -59.
- [42] Tang, W.C.; Lim, M.G. and Howe, R.T.; **Electrostatically balanced comb drive for controlled levitation**, Solid-State Sensor and Actuator Workshop, 1990, 4th Technical Digest, IEEE, 1990, p. 23 -27.
-

- [43] Tang, W.C.; Lim, M.G. and Howe, R.T.; **Electrostatic Comb Drive Levitation and Control Method**, Microelectromechanical Systems, Journal of, December 1992, p. 170 - 178.
- [44] Chien, Chao-Heng and Chen, Shi-Hao, **Fabrication comb-drive device by MEMS and electroplating**, Design, Test, Integration & Packaging of MEMS/MOEMS, May 2003.
- [45] V.P. Jaecklin; C. Lindert; N.F. de Rooij and J.M. Moret, **Micromechanical comb actuators with low driving voltage**, J. Micromech. Microeng., Volume 2, No 2, 1992, p.250-255.
- [46] Rob Legtenberg; A.W. Groeneveld and M. Elwenspoek, **Comb-drive actuators for large displacements**, J. Micromech. Microeng., Volume 6, No 3, September 1996, p.320-329.
- [47] S. G. Adams; F. M. Bertsch; K. A. Shaw; P. G. Hartwell; F. C. Moon and N.C. MacDonald, **Capacitance based tunable resonators**, J. Micromech. Microeng., 8 No 1, March 1998, p.15-23.
- [48] Hirano, T.; Furuhashi, T.; Gabriel, K.J. and Fujita, H., **Design, fabrication, and operation of submicron gap comb-drive microactuators**, Journal of Microelectromechanical systems, Volume 1, Issue 1, March 1992, p. 52 -59.
- [49] Wenjie Ye; Subrata Mukherjee and Noel C. Macdonald, **Optimal shape design of an electrostatic comb drive in microelectromechanical systems**, Microelectromechanical systems, Journal of, Volume 1, No. 1, March 1998, p. 18-25.
-

- [50] L. L. Mercado; S. M. Koo; T. Y. T. Lee and L. Liu, **A mechanical approach to overcome RF MEMS switch stiction problem**, in Proc. IEEE Electronic Components and Technology Conference 2003, New Orleans, LA, USA, May 27-30, 2003, p. 377-384.
- [51] J. Schimkat, **Contact measurement providing basic design data for microrelay actuators**, Sensors and Actuators A: Physical, vol. 73, no. 1-2, p.138-143, Mar 1999.
- [52] G. M. Rebeiz and J. B. Muldavin, **RF MEMS switches and switch circuits**, IEEE Microwave Magazine, vol. 2, no. 4, p. 59-71, Dec 2001.
- [53] G. M. Rebeiz, **RF MEMS theory, Design and Technology**, 1st ed. Hoboken, New Jersey, Wiley 2003.
- [54] T. Ono; D.Y. Sim and M. Esashi, **Micro-discharge and electric breakdown in a micro-gap**, Journal of Micromechanics and Microengineering, vol. 10, no. 3, p. 445-451, Sept 2000.
- [55] L.H. Germer, **Electrical breakdown between close electrodes in air**, Journal of Applied Physics, vol. 30, no. 1., p. 41-47, 1959.
- [56] H. F. Schlaak, **Potentials and limits of micro-electromechanical systems for relays and switches**, in Proc. Int. Conf. on Electrical Contacts, Zurich, Switzerland, Sept. 9-12, 2002, p. 19-30.
- [57] D. Hymen and M. Mehregany, **Contact physics of gold microcontacts for MEMS switches**, IEEE Trans. on Components and Packaging Technology, vol. 22, no. 3, p.357-364, Sept 1999.
-

[58] J. Schimkat, **Contact materials for microrelays**, in Proc. IEEE Micro Electro Mechanical Systems 1998, Heidelberg, Germany, Jan. 35-29, 1998, p. 190-194.

[59] E. J. J. Kruglick and K. S. J. Pister, **Lateral MEMS microcontact considerations**, IEEE Journal of Microelectromechanical Systems, vol. 8, no. 3, p. 264-271, Sept 1999.

[60] W. van Spengen; R. Puers; R. Mertens and I. De Wolf, **Experimental characterization of stiction due to charging in RF MEMS**, in Proc. IEEE Int. Electron Devices Meeting IEDM 2002, San Francisco, CA, USA, Dec 8-11, 2002, p. 901-904.

[61] C. C. Cabuz; E. I. Cabuz; T. R. Ohnstein; J. Neus and R. Maboudian, **Factors enhancing the reliability of touch-mode electrostatic actuators**, Sensors and Actuators A: Physical, vol. 79, no. 3, p. 245-250, Feb 2000.

[62] N. Tas; T. Sonnenberg; H. Jansen; R. Legtenberg and M. Elwenspoek, **Stiction in surface micromachining**, Journal of Micromechanics and Microengineering, vol. 6, no. 4, p. 385-397, Dec 1996.

[63] Ye. W.; Mukherjee S. and Macdonald N. C., 1998, **Optimization shape design of an electrostatic comb drive in micromechanical systems**, J. Microelectromechanical systems, Vol. 7, No. 1, p.16-26.

[64] Hirano, T.; Long-Sheng Fan; Wen Y. Lee; Hong, J.; Imaino, W.; Patanaik, S.; Chan, S.; Webb, P.; Horowitz, R.; Aggarwal, S. and Horsley, D.A., **High-bandwidth high-accuracy rotary microactuators for magnetic hard disk drive tracking servos**, Mechatronics, IEEE/ASME Transactions on, Volume 3, Issue 3, Sept. 1998, p. 156 -165.

References

[65] Cho Y.H., Pisano A.P., 1999, **Optimal structure design of micromechanical crap-leg flexure with micro fabrication constrains**, Proc. ASME Winter Annual meeting, Dallas, Texas, Nov.

[66] Gary K. Fedder, **Simulation of Microelectromechanical System**, Ph.D. thesis, University of California, Berkeley, 1994.

[67] Stephen P. Timoshenko and James M. Gere, **Mechanics of materials**, 2nd edition, 1987.

[68] MEMS Clearinghouse, MEMS Material Database, website:
<http://mems.isi.edu/mems/material/index.html>

Appendix

Detailed microfabrication process flow for the microactuator switch

Process 1 >> Deposition of Cr/Au film (on 700 μ m-thick Pyrex glass wafer)

- Objective: To cater for electrical routing and connections.
- Process: Sputter deposition
- Wafer: Glass wafer
- Mask: Mask 1 (electrical connection)
- Total thickness of the deposited Cr/Au film must not exceed 50nm.
- Thickness of chromium (Cr) film ~ 20nm.
- Thickness of gold (Au) film ~ 30nm.

The gold (Au) layer will be used both as electrode pads and electrical routing. Gold is selected because of its good combination capability with silicon wafer. Chromium is deposited as an intermediate layer between glass and gold, which will provide a strong adhesion force between them (i.e. an adhesion layer). Sputter deposition process is preferred over e-beam evaporation process in thin film deposition due to a faster deposition rate, better uniformity and excellent adhesion to substrate.

The sequential steps for microfabrication process 1 are as follows:

1. Perform the standard wafer preparation/cleaning/drying procedures.
 2. Perform RIE process (for ~ 120sec) to 'roughen' the surface of the glass wafer for better adhesion with the sputter deposited metal films.
-

-
3. Perform HMDS process for the wafer for better adhesion with photo-resist (PR).
 4. Spin-coat a layer of positive PR onto the wafer (thickness of PR is $9.91\mu\text{m}$; PR type is AZ9260).
 5. After spin-coating process, soft-bake wafer at a temperature of 110°C for a period of 240sec.
 6. Use Mask 1 (electrical connection) for photolithography process for the patterning of PR (hard-contact, exposure timing = 60sec)
 7. Perform resist development process ($\sim 75\text{sec}$) and rinse with de-ionized (DI) water.
 8. Perform spin-dry process to dry the wafer.
 9. Deposit Cr/Au film (to deposit Cr film first followed by Au film) by sputter deposition process.
 10. Perform lift-off process by immersing the sputtered wafer into a solution of acetone fully and subject to ultrasonic vibration process (for a clean lift-off at all edges of the deposited metal regions).
 11. Rinse the wafer with DI water.
 12. Spin-dry the wafer (sputtered glass wafer ready for process 2).

Process 2 >> Deposition of Cr/Au film (on $700\mu\text{m}$ -thick Pyrex glass wafer)

- Objective: To cater for electrical contact pads.
 - Process: Sputter deposition
 - Mask: Mask 2 (contact pad)
 - Wafer: Glass wafer (from Process 1)
 - Thickness of Cr film $\sim 30\text{nm}$
 - Thickness of Au film $\sim 0.4\mu\text{m}$ (or 400nm)
-

The sequential steps for microfabrication process 2 are as follows:

1. Perform HMDS process for the glass wafer (from process 1) for better adhesion with PR.
2. Spin-coat a layer of positive PR onto the previously sputtered side of the glass wafer from process 1 (thickness of PR is $9.91\mu\text{m}$; PR type is AZ9260).
3. After spin-coating process, soft-bake wafer at a temperature of 110°C for a period of 240sec.
4. Use Mask 2 (contact pad) for photolithography process for the patterning of PR (hard-contact, exposure timing = 60sec, alignment is needed between the sputtered alignment marks on the glass wafer and alignment marks on Mask 2).
5. Perform resist development process ($\sim 75\text{sec}$) and rinse with DI water.
6. Perform spin-dry process to dry the wafer.
7. Deposit Cr/Au film (to deposit Cr film first followed by Au film) by sputter deposition process.
8. Perform lift-off process by immersing the sputtered wafer into a solution of acetone fully and subject to ultrasonic vibration process (for a clean lift-off at all edges of the deposited metal regions).
9. Rinse the wafer with DI water.
10. Spin-dry the wafer (sputtered glass wafer ready for process 5).

Processes 1 and 2 are solely for microfabrication using the glass wafer. After processes 1 and 2 have been completed, the sputtered glass wafer will be ready for the anodic wafer bonding process.

Process 3 >> Back etching of cavities (on 200 μ m-thick silicon wafer)

- Objective: To etch cavities of a depth of 140 μ m.
- Process: DRIE
- Mask: Mask 3 (back etching)
- Wafer: Silicon wafer and support wafer

This process is to etch cavities in order to provide moving space for the microactuator switch. The etch depth for the cavities will depend on the designed thickness of the comb drive and spring flexure structures. The microactuator switch will be bonded to a glass substrate for structural reliability. Therefore the silicon wafer needs to be patterned on both sides and etched. The top-side silicon will be the pattern of the comb drive and flexure support features of the microactuator switch; whereas the bottom-side will be the cavities.

The sequential steps for microfabrication process 3 are as follows:

1. Perform the standard wafer preparation/cleaning/drying procedures.

{Note: Steps 2 to 6 are for the preparation of the support wafer for DRIE purpose. The support wafer is required to provide a structural support for the thin silicon wafer when subjected to DRIE process in which many cavities are to be etched which will reduce the structural integrity of the wafer.}

2. Perform HMDS process on a clean silicon support wafer for better adhesion with PR.
-

-
3. Spin-coat a layer of positive PR onto the support wafer (thickness of PR is $9.91\mu\text{m}$; PR type is AZ9260).
 4. Perform 'manual' wafer bonding process by attaching the silicon working wafer onto the support wafer. Manual wafer alignment is done using the wafer flats.
 5. Soft-bake the attached wafers at a temperature of 110°C for a period of 30mins.
 6. Allow a cooling period of 10mins.
 7. Perform HMDS for the attached wafers for better adhesion with PR.
 8. Spin-coat a layer of positive PR onto the top surface of the silicon wafer (thickness of PR is $9.91\mu\text{m}$; PR type is AZ9260).
 9. After spin-coating process, soft-bake the attached wafers at a temperature of 110°C for a period of 240sec.
 10. Use Mask 3 (back etching) for photolithography process for the patterning of PR (hard-contact; exposure timing = 60sec).
 11. Perform resist development process ($\sim 75\text{sec}$) and rinse with DI water.
 12. Perform spin-dry process to dry the attached wafers.
 13. Perform DRIE to obtain cavities of a depth of $140\mu\text{m}$.
 14. Perform resist-stripping process and support wafer stripping process simultaneously by fully immersing the attached wafers into a solution of acetone and subject to ultrasonic vibration process.
 15. Perform the standard wafer cleaning procedures for the stripped silicon wafer with etched cavities (ready for process 4).

Process 4 >> Etching of dielectric slot hole (on the $200\mu\text{m}$ -thick silicon wafer)

- Objective: To etch dielectric slot holes
 - Process: DRIE
-

- Mask: Mask 4 (insulation slot)
- Wafer: Silicon wafer (from process 3) and support wafer
- Dimension of dielectric slot hole is $(L \times W)\mu\text{m}^2 = (60 \times 3)\mu\text{m}^2$ with a depth of $60\mu\text{m}$.

The dielectric slot hole is to be filled with silicon oxide and low-temp oxide respectively, and will act as an electrical isolation between the switch contact region and the microactuator switch structure. In operation, the center translating beam structure will always be grounded with alternating voltages supplied to the corresponding set of fix comb drive finger electrodes. The dielectric slot will provide electrical isolation between the switch contact region and the center translating beam.

The sequential steps for microfabrication process 4 are as follows:

1. Perform HMDS process on the un-etched topside of the silicon wafer (from process 3) for better adhesion with PR.
 2. Spin-coat a layer of positive PR onto the silicon wafer (thickness of PR is $2.70\mu\text{m}$; PR type is AZ7220).
 3. After spin-coating, soft-bake the wafer at a temperature of 100°C for a period of 90sec.
 4. Allow a cooling down period of 60sec.
 5. Use Mask 4 (insulation slot) for photolithography process for the patterning of PR (vacuum-contact; exposure timing = 3.4sec; alignment is needed between the etched alignment marks on the silicon wafer and the alignment marks on Mask 4).
-

6. After photolithography process, post-bake the wafer at a temperature of 110°C for a period of 60sec.
7. Perform resist development process (~ 60sec).
8. Rinse the wafer with DI water for a period of 60sec.
9. Perform spin-dry process to dry the wafer.
10. After spin-dry process, soft-bake the wafer at a temperature of 100°C for a period of 120sec.

{Note: Steps 11 to 15 are for the preparation of the support wafer for DRIE purpose.

Note that in this case the support wafer is not manually bonded to the silicon wafer first before the photolithography process, because by doing so the etched alignment marks would be covered or obscured by the support wafer and therefore alignment during photolithography process is not possible.}

11. Perform HMDS process on a clean support wafer for better adhesion with PR.
 12. Spin-coat a layer of positive PR onto the support wafer (thickness of PR is 5.00µm; PR type is AZ9260).
 13. Perform 'manual' wafer bonding process by attaching the etched side of the silicon wafer to the support wafer. Manual wafer alignment is done using the wafer flats.
 14. Soft-bake the attached wafers at a temperature of 110°C for a period of 15mins.
 15. Allow a cooling period of 10mins.
 16. Perform DRIE process to obtain the through slot holes.
-

-
17. Perform resist-stripping process and support wafer stripping process simultaneously by immersing the attached wafers into a solution of acetone fully and subject to ultrasonic vibration process.
 18. Perform wafer cleaning procedures for the stripped silicon wafer with both etched cavities and through slot holes.
 19. Grow a layer of silicon oxide (SiO_2) of thickness $\sim 2\mu\text{m}$ via thermal oxidation process on the silicon wafer (from step 14).

{Note: After step 19, the width of the di-electric slot hole ($3\mu\text{m}$) would be reduced to $\sim 1\mu\text{m}$.}

20. Deposit a layer of silicon nitride (Si_3N_4) of thickness $\sim 0.5\mu\text{m}$ via low-pressure chemical vapour deposition (LPCVD) process.

{Note: After step 20, the remaining $\sim 1\mu\text{m}$ gap would be completely filled up by the deposited silicon nitride layer.}

21. Remove the surface oxide layers by RIE and DRIE processes.
22. Perform standard wafer cleaning procedures for the silicon wafer after the oxide-removal processes (ready for process 5).

Process 5 >> Wafer bonding (between the glass wafer and silicon wafer)

- Objective: To bond the prepared silicon and glass wafers.
 - Process: Anodic wafer bonding
 - Wafers: Glass wafer (from process 2) and silicon wafer (from process 4)
-

-
- Bonding process is performed between sputter-deposited top-side of glass wafer and etched backside of silicon wafer.
 - Alignment is needed between the sputtered metal film alignment marks on the glass wafer and the etched-through alignment marks on the silicon wafer.
 - Anodic bonding process is performed under a voltage of 1000V and a temperature of 363°C.

As the glass substrate is deposited with Cr/Au films for the electrode pads, anodic wafer bonding is the preferred bonding process. The glass substrate is selected because it can provide good isolation between the different electrodes, and also has good toughness to support the movement of the microactuator switch. Anodic bonding process takes place at a temperature of 363°C, which is lower than the melting point of glass. The bonding stress is comparable to that of fusion bonding. Anodic bonding process should be carried out very carefully because many factors such as temperature, bonding pressure and even the presence of native oxides can affect or hinder the bonding process.

Process 6 >> Etching of comb-drive finger elements and flexure features (on the top silicon wafer side of the bonded wafers)

- Objective: To etch both the comb-drive features and flexure supports.
 - Process: DRIE
 - Mask: Mask 5 (comb-drive fingers)
 - Wafer: Bonded silicon-glass wafer (from process 5)
-

The sequential steps for microfabrication process 6 are as follows:

1. Perform HMDS process on the bonded wafers for better adhesion with PR.
 2. Spin-coat a layer of positive PR onto the top-side of the silicon wafer side for the bonded wafer (thickness of PR is 2.70 μ m; PR type is AZ7220).
 3. After spin-coating, soft-bake wafer at a temperature of 100°C for a period of 90sec.
 4. Allow a cooling down period of 60sec.
 5. Use Mask 5 (comb-drive fingers) for photolithography process for the patterning of PR (vacuum-contact; exposure timing = 3.4sec; alignment is needed between the etched alignment marks on the silicon wafer and the alignment marks on Mask 5).
 6. After photolithography process, post-bake the bonded wafers at a temperature of 110°C for a period of 60sec.
 7. Perform resist development (~ 60sec).
 8. Rinse the bonded wafers with DI water for a period of 60sec.
 9. Perform spin-dry process to dry the bonded wafers.
 10. After spin-dry process, soft-bake the bonded wafer at a temperature of 100°C for a period of 120sec.
 11. Perform DRIE process to obtain the comb-drive features.
 12. Perform resist-stripping process by immersing into a solution of acetone.
 13. Perform drying process by using low-pressure compressed air (ready for process 7).
-

Process 7 >> Deposition of Ti/Au film at the switch contact region

- Objective: To deposit conducting metal films at the switch contact region via a shadow mask wafer.
- Process: DRIE and Sputter deposition
- Mask: Mask 6 (shadow mask opening)
- Wafer: Bonded glass-silicon wafer (from process 6) and a shadow mask
- A shadow mask wafer is to be positioned over the bonded wafer at the switch contact region for the purpose of sputter deposition of Ti/Au film.
- Thickness of titanium (Ti) film = 50nm
- Thickness of gold (Au) film = 0.5 μ m (or 500nm)
- Dimension of through opening on the shadow mask = (300x200) μ m²

The sequential steps for microfabrication process 7 are as follows:

{Note: Steps 1 to 6 are for the preparation of the support wafer for DRIE purpose for the shadow mask wafer. The support wafer is required to provide a structural support for the thin silicon shadow mask wafer when subjected to DRIE process where many through openings are to be etched.}

1. Perform the standard wafer preparation/cleaning/drying procedures.
 2. Perform HMDS process on a clean silicon support wafer for better adhesion with PR.
 3. Spin-coat a layer of positive PR onto the support wafer (thickness of PR is 9.91 μ m; PR type is AZ9260).
-

-
4. Perform 'manual' wafer bonding process by attaching the silicon wafer onto the support wafer. Manual wafer alignment is done using the wafer flats.
 5. Soft-bake the attached wafers at a temperature of 110°C for a period of 30mins.
 6. Allow a cooling period of 10mins.
 7. Perform HMDS process on the silicon wafer for better adhesion with PR.
 8. Spin-coat a layer of positive PR onto the wafer (thickness of PR is 9.91µm; PR type is AZ9260).
 9. After spin-coating, soft-bake the attached wafers at a temperature of 110°C for a period of 240secs.
 10. Use Mask 6 (shadow mask opening) for photolithography process for the patterning of PR (hard-contact, exposure timing = 60sec).
 11. Perform resist development (~ 75sec) and rinse with DI water.
 12. Perform spin-dry process to dry the wafer.
 13. Perform DRIE (through etching) to obtain the required through hole openings.
 14. Perform resist-stripping process and support wafer stripping process simultaneously by immersing the attached wafers into a solution of acetone fully and subject to ultrasonic vibration process.
 15. Perform the standard wafer cleaning procedures for the stripped silicon wafer with etched openings (i.e. the shadow mask wafer).

{Note: Steps 16 to 18 are for the sputter deposition of Ti/Au films at the switch contact region.}

16. Position, align and secure the position of the shadow mask wafer (from step 15) over the bonded wafers (at the top silicon face).
-

17. Deposit the Ti/Au (to deposit Ti film first followed by Au film) layers by sputter deposition process.
18. After the sputter deposition process, remove the shadow mask wafer.

After process 7 has been completed, microfabrication of the prototype of the lateral MEMS microactuator switch is completed.
